# Development of a Ridged Slip-Resistant Connection for Modular Aluminum Bridge Deck Applications

By

James St.Onge

A thesis
presented to the University of Waterloo
in fulfilment of the
thesis requirement for the degree of
Master of Applied Science
in
Civil Engineering

Waterloo, Ontario, Canada, 2018

## Author's Declaration

I hereby declare that I am the sole author of this thesis. This is a true copy of my thesis, including any required final revisions, as accepted by my examiners.

I understand that my thesis may be made electronically available to the public.

## Abstract

Aluminum is a lightweight material that possesses excellent corrosion resistance and has been shown to be an attractive alternative to steel and concrete for the construction and rehabilitation of bridge structures. It is often possible to increase the load-carrying capacity of a bridge with an existing concrete deck by reducing the structure's self-weight through the installation of an aluminum deck. For new construction, aluminum can allow for the use of accelerated bridge construction (ABC) methods as the lightweight components can be easily transported and installed on site. Aluminum also offers potential for lower life-cycle costs due to its high corrosion resistance, which reduces maintenance requirements and eliminates the need for protective coatings.

One of the latest developments in bridge construction and rehabilitation is the modular aluminum bridge deck system, which consists of a series of pre-fabricated panels that are fastened together to form a continuous deck. Welds and mechanical fasteners can both be used to join the panels together. However, a mechanical fastening system is often advantageous for ease of transportation and installation. Modular aluminum bridge deck systems offer all of the benefits that are associated with the use of aluminum for bridge structures, and their modular design provides opportunities for ABC methods in both new construction and rehabilitation projects. They are currently more commonplace in Europe than in North America, however, which is due, in part, to a lack of commercially available products in the North American market. There is a particular lack of products that implement a mechanical fastening system for the panel-to-panel connections. A need has therefore been identified to develop a novel modular aluminum bridge deck system with mechanical connections for vehicular bridge structures in North America.

The research presented in this thesis focuses on the development of a novel ridged slip-resistant connection for future implementation in a modular aluminum bridge deck system. Ridged slip-resistant connections consist of interlocking faying surfaces, which are clamped together with mechanical fasteners, with the goal of providing improved strength and ductility compared to equivalent slip-resistant connections with flat faying surfaces. In the current study, their performance is validated through experimental testing, finite element modelling, and the development of a simple mechanistic model for predicting their slip-resistance.

An experimental program was carried out to study the performance of ridged and non-ridged slip-resistant connections with carbon steel and stainless steel bolts. Static and cyclic tests were performed on small-scale lap-splice specimens fabricated from 6061-T6 aluminum. The results of the static tests were used to characterize the behaviour of ridged slip-resistant connections and to quantify the performance gains between the ridged and non-ridged specimens. The results of the cyclic tests were used to provide a preliminary assessment of the fatigue performance of ridged slip-resistant connections.

Finite element (FE) modelling was conducted to predict the behaviour of each experimental test specimen. The slip loads predicted by the FE models were compared to the experimental observations and were then used in combination with the experimental observations to validate an equilibrium-based mechanistic model. The mechanistic model was combined with the existing design provisions of CSA S6 Canadian Highway Bridge Design Code (CSA Group, 2014) to develop a design equation for aluminum ridged slip-resistant connections at the service limit state. The stress concentrations predicted by the FE models were used as inputs for a strain-life analysis, which was carried out to predict the fatigue lives of the cyclic experimental test specimens. Further FE modelling was conducted to study a full-scale modular aluminum bridge deck system so that the feasibility of implementing ridged slip-resistant connections between the panels could be verified.

**Acknowledgements**

I would like to thank my supervisor, Dr. Scott Walbridge, for the guidance and support which he provided throughout the entire duration this research project. His knowledge and expertise in the areas of aluminum, finite element modelling, and fatigue were crucial to the successful completion of this research. I would also like to thank Dr. Donald Burn and Dr. Adrian Gerlich for their review of this thesis.

I would like to thank the Civil Engineering Structures Laboratory technicians, Douglas Hirst, Peter Volcic, and Richard Morrison, for their expertise and assistance with the experimental testing portion of this research. I would also like to thank my colleague, Dylan Dowling, for his assistance with experimental testing and the digital image correlation (DIC) component of this project.

Furthermore, I would like to thank the MAADI Group and the Natural Sciences and Engineering Research Council of Canada for graciously funding this research. I would also like to thank Ajax Fasteners of Australia for generously donating the ONESIDE$^{TM}$ blind bolts that were used for the experimental testing portion of this research.

Finally, I would like to thank my friends and family for their continuous support throughout the completion of my degree.

## Table of Contents

## List of Figures

## List of Tables

# 1 Introduction

## 1.1 General

North American highway authorities are currently faced with the challenge of upgrading a substantial number of dated bridge structures that are contributing immensely to severe and pressing maintenance costs. The need to repair these structures in a cost-effective and timely manner represents a great opportunity to promote the use of aluminum in structural engineering and highway infrastructure applications. To date, the use of aluminum in vehicular bridges has been limited for several reasons, including the high initial cost of aluminum and the historical lack of codes and standards for the design of aluminum structures. It has been shown, however, that aluminum can be a very competitive option for bridge deck replacements, based on a comparison of total life-cycle costs. This demonstrates the important role that modular aluminum bridge decks could play in the rehabilitation of deteriorated bridge structures.

Modular aluminum bridge decks are a relatively new technology in bridge engineering and have several advantages over conventional concrete decks. In addition to the benefit of reduced life-cycle costs, the load-carrying capacity of an existing bridge can often be increased through the installation of a lightweight aluminum deck. Aluminum bridge decks are also highly durable due to their high corrosion resistance, and they provide opportunities for accelerated bridge construction due to their lightweight and modular design. An example of a modular aluminum bridge deck system is shown in Figure 1.1.

Modular aluminum bridge decks are assembled from a series of panels that are typically fabricated through an aluminum extrusion process. The panels can either be connected to one another other using aluminum welding techniques (e.g. arc or friction stir welding) or with mechanical fasteners. It is thought that there may be potential benefits to connecting the panels with mechanical fasteners rather than welds, so that fatigue problems can be avoided and the panels can be shipped to site and installed individually. To date, both connection methods have been used successfully for vehicular bridges. There is currently a lack of commercially available products in North America, however. In particular, there are no existing products in North America that employ mechanical means to connect the extrusions to each other. It is also prohibitively expensive to import modular aluminum bridge deck products from Europe where they are more commonplace, as the additional

upfront costs negate the life-cycle cost savings. This suggests a need to develop new modular aluminum bridge deck systems for vehicular bridges in North America.

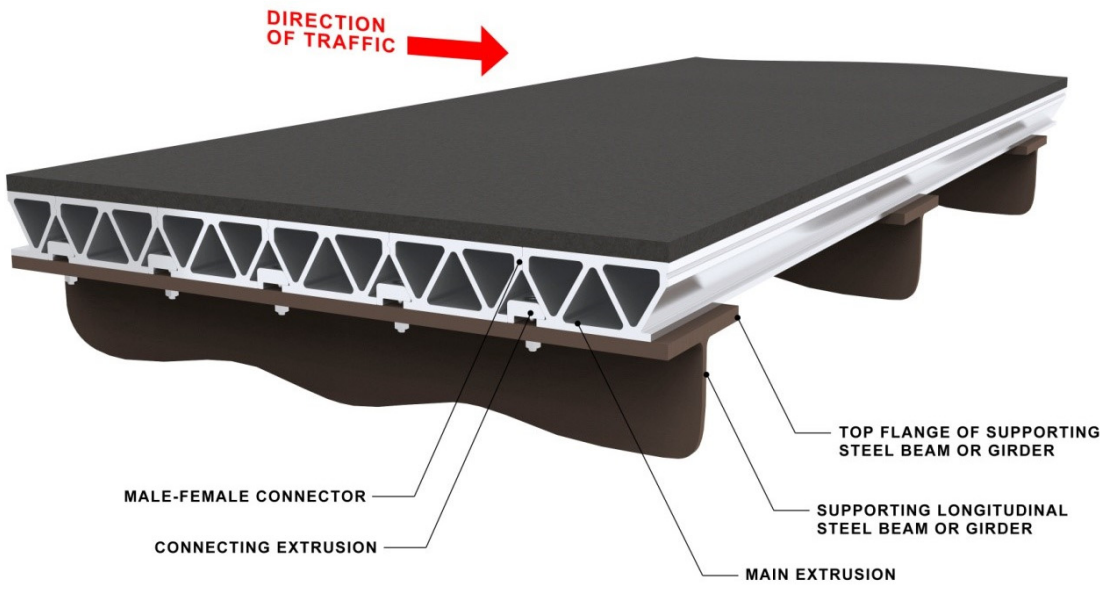


Figure 1.1: Modular aluminum bridge deck system (Walbridge & de la Chevrotiere, 2012)

## 1.2 Objectives

The primary purpose of the research presented in this thesis was to assess the performance and behaviour of an original ridged slip-resistant connection that could be used as a means for mechanically connecting extrusions in aluminum bridge decks and other applications. The specific objectives of the work summarized in this thesis were as follows:

1. to develop a parametric study process to optimize the ridge geometry of ridged slip-resistant connections;

2. to develop a simple mechanistic model for predicting the slip-resistance of ridged slip-resistant connections;

3. to develop a three-dimensional finite element modelling procedure for predicting the behaviour of ridged slip-resistant connections;

4. to perform experimental testing to evaluate and compare the performance of several ridged slip-resistant connections in relation to non-ridged slip-resistant connections;

5. to compare the results of the experimental testing to predictions made using the developed mechanistic and three-dimensional finite element models; and

6. to present preliminary design recommendations for ridged slip-resistant connections.

## 1.3 Scope

The scope of the work presented in this thesis is limited primarily to the study of ridged slip-resistant connections, and not the structural systems in which they may be implemented. A bridge deck analysis is performed primarily to obtain load effects. However, the ridged connections have not been studied as functioning components of such systems.

The experimental testing presented in this thesis is limited to small-scale testing of lap-splice specimens. The ridge geometry used for the experimental program is also limited to a single ridge profile.

## 1.4 Thesis Organization

This thesis consists of nine chapters, including the current introductory chapter. Brief descriptions of the subsequent chapters are provided as follows:

In Chapter 2, a review of current literature pertaining to the research described within this thesis is presented. First, the use of aluminum in bridge structures is discussed, including the primary advantages and challenges associated with the use of aluminum in bridge engineering. Existing modular aluminum bridge deck systems are then presented, along with the experimental and analytical analyses that have been carried out to assess the behaviour and performance of each system. Next, mechanical fasteners that are suitable for use in aluminum bridge structures are discussed. Finally, the existing code provisions for slip-resistant connections are presented, and recent efforts to improve the performance of slip-resistant connections are discussed.

In Chapter 3, a parametric study is presented, which was used to assess the impact of ridge geometry on the performance of aluminum ridged slip-resistant connections. First, the finite element models that were used for the study are presented, along with the process that was used to automate the creation of the models. The results of the study are then presented and discussed.

In Chapter 4, a simple mechanistic model is presented, which was developed for predicting the slip-resistance of ridged slip-resistant connections. First, the derivation of the model is described. The results are then compared to the finite element analysis presented in Chapter 3.

In Chapter 5, an experimental program is presented, which was carried out to evaluate the performance of aluminum ridged slip-resistant connections. First, the test matrix is introduced, along with the geometry and material properties of the specimens. The specimen design and fabrication methods are also discussed. Next, the instrumentation used for each of the tests is described, and the typical experimental test setup is presented.

In Chapter 6, the results of the experimental program are presented. The observed behaviour of the specimens is discussed, and overall trends are described.

In Chapter 7, the experimental results are compared to numerical and mechanistic model solutions. First, the experimental results from the static tests are compared to the mechanistic model presented in Chapter 4. Next, finite element models used to predict the slip loads of the static load test specimens are described, and the modelling assumptions are validated. The experimental results from the static tests are then compared to the predictions made using the finite element models. Next, a strain-life method is used to make fatigue life predictions for the ridged connections, which are compared to experimental results obtained from a pilot study performed to investigate the fatigue performance of this connection type. Finally, preliminary design recommendations for ridged slip-resistant connections are presented.

In Chapter 8, a finite element model is presented, which was used to predict the normal and shear forces that are transferred between modular aluminum bridge deck panels. The results of the model are then presented and discussed in relation to the experimental observations.

In Chapter 9, the conclusions drawn from the findings of the research are presented and recommendation for further research are discussed.

# 2 Literature Review

This chapter presents a review of current literature pertaining to the research described within this thesis. First, the use of aluminum in bridge structures is discussed, including the primary advantages and challenges associated with the use of aluminum in bridge engineering. Existing modular aluminum bridge deck systems are then presented, along with the experimental and analytical analyses that have been carried out to assess the behaviour and performance of each system. Next, mechanical fasteners that are suitable for use in aluminum bridge structures are discussed. Finally, the existing code provisions for slip-resistant connections are presented, and recent efforts to improve the performance of slip-resistant connections are discussed.

## 2.1 Use of Aluminum in Bridges

Aluminum is a lightweight material that offers several advantages over steel and concrete for the construction and rehabilitation of bridges. The first instance of aluminum use for bridge rehabilitation occurred in 1933 when the steel stringers and wood deck of the Smithfield Street Bridge in Pittsburgh, PA, were replaced with an aluminum deck (Growdon et al., 1934). The first bridge constructed entirely of aluminum followed later, and was built over the Saguenay River in Arvida, Canada in 1950. The Arvida bridge remains in service today as the longest aluminum bridge in the world (Siwowski, 2006). Despite the higher initial costs associated with aluminum construction, aluminum has become an increasingly popular choice for bridge construction and rehabilitation projects. This is primarily due to lower total life-cycle costs when compared to concrete and steel.

The lower life-cycle costs associated with aluminum arise from its high corrosion resistance, which reduces maintenance requirements and eliminates the need for protective coatings. Siwowski (2006) writes that corrosion has been identified as the leading cause of deterioration in both concrete and steel bridges and it is therefore the most important factor responsible for the majority of structurally deficient bridges. In scenarios where bridges may be subject to high levels of corrosion, such as in marine environments or in areas where large amounts of road salt are used, it is possible for the higher initial cost of aluminum to offset the maintenance costs that would arise from the use of steel or concrete. This is an important consideration for both new construction and for the rehabilitation of existing bridges in corrosive environments.

Another beneficial property of aluminum is its low density, which is approximately one third that of steel (Das & Kaufman, 2007). For bridge rehabilitation projects, it is possible to increase the load-carrying capacity of a bridge with an existing concrete deck by replacing it with an aluminum deck. In literature, it has been reported that an aluminum deck can weigh as little as 10% of that of an equivalent concrete deck (Arrien et al., 2001). The replacement of a concrete deck with a lightweight aluminum deck can also provide cost savings by reducing the rehabilitation needs for the substructure and superstructure (Siwowski, 2006). For new bridge construction, aluminum can enable accelerated bridge construction (ABC) as the components can be easily transported and installed on site (Das & Kaufman, 2007).

The strengths of structural aluminum alloys are comparable to those of the mild steels that are commonly used for bridge construction (Das & Kaufman, 2007). Aluminum also has a high toughness and is resistant to low-ductility fracture, unlike older steels used for bridges which have been found to be susceptible to ductile-to-brittle transitions in failure modes (Das & Kaufman, 2007). The elastic modulus of aluminum is 68.9 GPa, which is approximately one third of that of steel, and aluminum's coefficient of thermal expansion is about twice that of steel. In addition, the fatigue strength of aluminum is about one third of that of steel (Das & Kaufman, 2007). These differences in material properties must be accounted for in design, especially when aluminum and other materials are fastened together. Saleem et al. (2012) also note that galvanic corrosion can be a concern when dissimilar metals are in contact, such as an aluminum deck sitting on steel girders. One possible solution to this problem is the use of stainless steel to separate the aluminum and steel (Saleem et al., 2012).

Das and Kaufman (2007) write that one of the factors limiting the use of aluminum in civil engineering applications has been a historical lack of knowledge of the properties and design rules for aluminum, as well as an unwillingness to break away from the more typical use of steel and concrete. It has been shown, however, that aluminum provides several advantages over steel and concrete for bridge construction and rehabilitation, and it should be considered as a design option in certain cases. Aluminum design provisions now exist within CSA S6 Canadian Highway Bridge Design Code (CSA Group, 2014), and further design guidelines are provided by CSA S157 Strength Design in Aluminum (CSA Group, 2005). Aluminum already makes up approximately

90% of all structural metal used in the aircraft industry, and its low life-cycle cost can make it a competitive option for bridges as well (Das & Kaufman, 2007).

## 2.2 Modular Aluminum Bridge Deck Systems

Modular aluminum bridge deck systems are a relatively recent development in bridge construction and rehabilitation. They consist of a series of pre-fabricated panels that are fastened together to form a continuous deck. The panels are fabricated through extrusion, which gives designers a large range of freedom to develop unique and highly optimized sections. The panels can either be joined together other using aluminum welding techniques or with mechanical fasteners. A mechanical fastening system is advantageous in terms of transportation and installation, as the panels can be shipped to site and installed individually. Welded panels must be pre-assembled in a shop and shipped to site in larger sections. Mechanical fasteners also avoid the fatigue issues that are associated with aluminum welding methods. To date, both mechanical and welded connections have been used for bridges employing modular aluminum bridge decks.

An example of a modular aluminum bridge deck system with welded connections is a system developed by Reynolds Metal Company, which is now owned by Alcoa Corporation. An experimental program and analytical model of the Reynolds deck system are described by Dobmeier et al. (2001). Two static load tests were performed on identical deck sections, each consisting of nine 3.66 m long extrusions welded together to form a 3.66 m by 2.74 m panel. The extrusions were fabricated from 6063-T6 aluminum, which has a minimum yield strength of approximately 172 MPa and a tensile strength of approximately 207 MPa. A typical extrusion cross-section is shown in Figure 2.1. The first deck section was subjected to 3-point bending and failed at an ultimate load of approximately 872 kN by gross yielding under the load patch. The second deck section was subjected to 4-point bending and failed at an ultimate load of approximately 1,441 kN by fracture of a weld on the bottom surface of the deck. The analytical model used to predict the behaviour of the deck sections was created using the software ABAQUS by Dassault Systèmes. It incorporated non-linear material properties to capture the post-yielding behaviour of the sections. The model also accounted for the reduced strength of the heat-affected zone (HAZ) at weld locations. It was found that the analytical model was able to accurately predict both the failure modes and ultimate capacities of the deck panels. Dobmeier et al. (2001) note that

the welds are potential weak points in the aluminum bridge deck system, and that fracture may occur if the deck is overloaded in certain configurations.

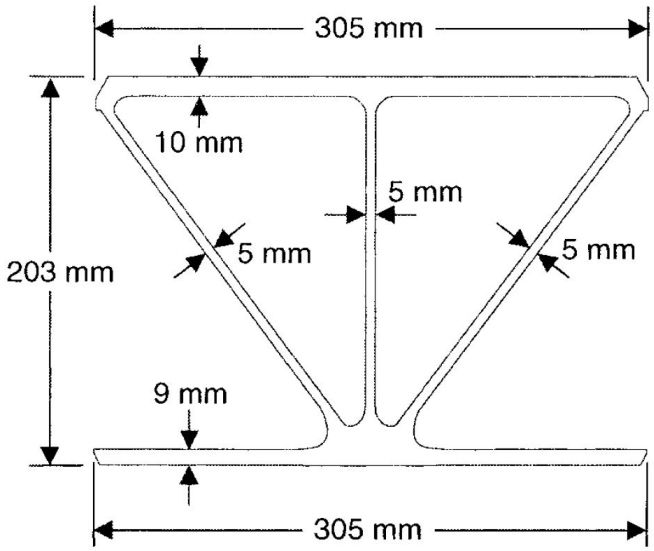


Figure 2.1: Extrusion cross-section of the Reynolds modular aluminum bridge deck system (Dobmeier et al., 2001)

A modular aluminum bridge deck system that is similar to the Reynolds system has been studied by Siwowski (2009b). Five static service load tests were carried out on identical deck sections with varying boundary conditions and load configurations. Each deck section consisted of sixteen 6005A-T6 aluminum extrusions welded together to form 2.1 m by 3.2 m panels. A typical extrusion cross-section is shown in Figure 2.2. The five test configurations were chosen to replicate typically encountered scenarios, and the service loads were based on the Polish bridge code. For each wheel load, 150 kN of force was applied onto a 0.2 m by 0.6 m patch. This wheel load is much greater than the typical design value specified by the CSA S6 Canadian Highway Bridge Design Code (CSA Group, 2014), in which the maximum wheel load of the CL-625-ONT truck is 87.5 kN applied over a 0.25 m by 0.6 m area (CSA Group, 2014). The five static load tests demonstrated that the deck sections had sufficient stiffness and strength to support the service wheel loads. However, Siwowski (2009b) notes that further testing would be needed to verify the fatigue resistance of the welded connections before implementing the deck system on an actual bridge. In a related paper, Siwowski (2009a) presents a finite element (FE) model, which was used to accurately predict the behaviour of the deck sections under service loads.

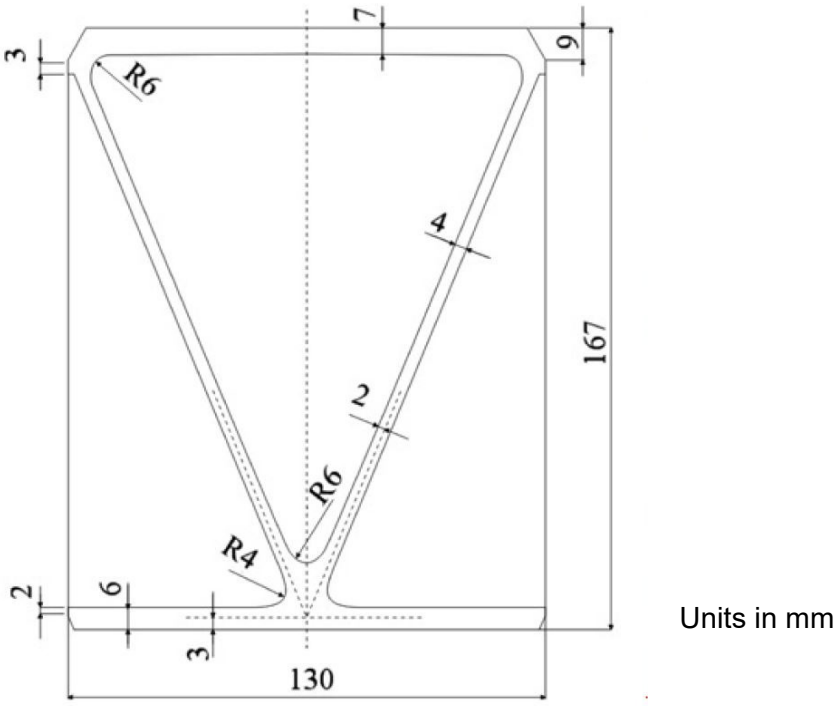


Figure 2.2: Extrusion cross-section of the Siwowski modular aluminum bridge deck system (Siwowski, 2009b)

Following the five service load tests, Siwowski performed two ultimate load tests on two of the deck sections to determine the maximum load-carrying capacities and failure modes. Each test used one of the load configurations from the previous service load tests. The first deck section was subjected to 3-point bending and failure occurred at a load of approximately 560 kN by gross section yielding under the load patch. The deck still retained additional capacity, however, and loading was continued up to 585 kN, at which point a weld fractured on the top surface of the deck. The second deck section was subjected to 4-point bending and failure occurred at a load of approximately 926 kN by fracture of a weld on the bottom surface of the deck. These failure modes are similar to those previously observed by Dobmeier et al. (2001).

An example of a modular aluminum bridge deck system that does not use welded connections is the system developed by Lars Svensson and Lars Pettersson. This system has already been used in a number of bridge rehabilitation projects (Svensson & Pettersson, 1990). The system consists of 6063-T6 aluminum extrusions, which fit together using a tongue-in-groove connection between the top flanges of adjacent extrusions, as shown in Figure 2.3. This connection transfers shear

forces between connecting extrusions but allows them to rotate independently from one another. Secondary extrusions and bolts are used to clamp the extrusions to the supporting structure. Experimental testing and analytical modelling have both been carried out to study the performance of the deck system, and good alignment has been shown between the experimental and analytical results (Arrien et al., 2001; Svensson & Pettersson, 1990). The experimental tests have shown that the deck system meets the requirements of the Swedish National Road Authority (SNRA) at both service and ultimate load levels, and that the fatigue performance exceeds the requirements of the American Association of State Highway and Transportation Officials (AASHTO) (1991). Arrien et al. (2001) note that this particular system is more economical and practical than its welded counterparts as fabrication costs are greatly reduced and the system is less susceptible to fatigue.

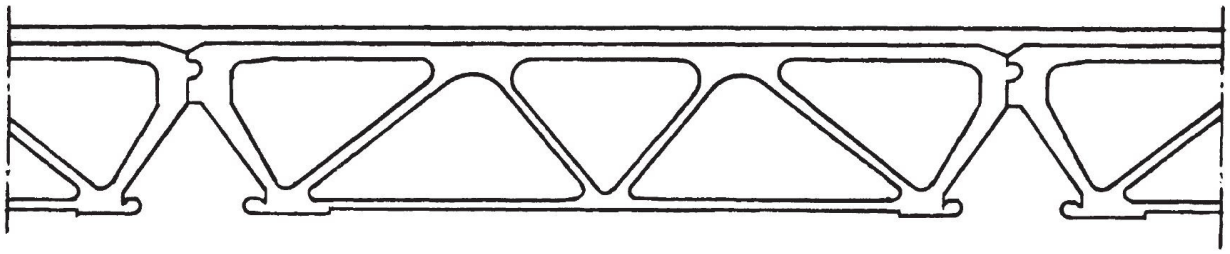

Figure 2.3: Cross-section of the Svensson and Pettersson modular aluminum bridge deck system (Svensson and Pettersson, 1990)

More recently, Saleem et al. (2012) have carried out extensive experimental testing and FE modelling to determine the feasibility of implementing Svensson and Pettersson's modular aluminum bridge deck system for movable bridges in North America. The experimental testing consisted of both static and cyclic tests using wheel loads for the HS 20 truck as specified by AASHTO (2005). First, three static tests were performed on individual extrusions, including a simple-span test, a continuous two-span test, and an inverted simple-span test. These static tests demonstrated that the capacity of the individual extrusions greatly exceeded the AASHTO requirements. For each test, failure occurred by excessive deflection or local buckling of plate elements. Next, a shear test and an uplift test were performed on the connectors, which clamp the extrusions to the supporting structure. The shear capacity of the connectors was compared to the braking force of an HS 20 truck, and it was found that the capacity of the clamping system exceeded the AASHTO requirements by a factor of approximately 2.7. The uplift capacity of the

connectors was compared to wind uplift pressure, and it was found that the capacity of the clamping system exceeded the AASHTO requirements by a factor of at least 4. In the uplift test, the extruded deck sections failed before the connectors reached their ultimate capacity. Saleem et al. (2012) note that the failure of a single connector on a deck will not be catastrophic as the system is redundant, however routine inspections are recommended to ensure that all clamps are intact. Following the tests on the connectors, a shear test was performed on the tongue-in-groove connection between adjacent extrusions. The capacity of this connection was found to exceed the AASHTO requirements by a factor of approximately 2. Finally, a constant-amplitude fatigue test was performed on a deck section consisting of three connected extrusions. Load was applied at two locations on the deck section, representing a single axle of the design truck. Two million cycles were applied to the deck section, and no signs of cracking or failure were observed. A connector between one of the extrusions and the supporting beams failed after 200,000 cycles, however Saleem et al. (2012) attribute this to the fact that only half of the number of connectors recommended by the manufacturer were used for the test. Residual strength tests were performed on the deck section following the completion of the fatigue test, and it was found that the deck was able to withstand a load nearly three times that of the HS 20 truck wheel load, although some elastic local plate buckling was observed. Saleem et al. (2012) conclude that Svensson and Pettersson's modular aluminum bridge deck system appears to be promising for implementation in moveable bridges. However, further research is needed to evaluate potential wear surfaces, and a field-monitoring program should be performed under ambient traffic and designated truck loading.

## 2.3 Mechanical Fasteners for Aluminum Bridges

Although aluminum is known to have very good corrosion resistance, galvanic corrosion can be a concern when aluminum is in contact with certain metals. Galvanic corrosion is induced when two dissimilar materials, such as aluminum and steel, are coupled in a corrosive electrolyte (Roberge, 2008). This is problematic for aluminum bridges constructed with carbon steel bolts in colder climates where de-icing salt is used. As such, the CSA S6 (CSA Group, 2014) specifies that only certain types of bolts can be used for aluminum bridges. These are aluminum bolts conforming to ASTM F468, carbon steel bolts conforming to ASTM A325M and galvanized in accordance with CAN/CSA-G164, and stainless steel bolts conforming to ASTM F593 Group 1 or 2 (2014). Carbon

steel and stainless steel bolts are generally stronger than aluminum bolts, and are therefore typically better suited for structural applications. The behaviour of stainless steel is quite different than that of carbon steel, however, and it is important to consider the differences in behaviour when deciding to use stainless steel or carbon steel fasteners for bridge applications.

Stainless steel fasteners are often chosen for their high ductility, aesthetic appeal, fire resistance, strain-hardening characteristics, and corrosion resistance (Bouchaïr et al., 2008). Like aluminum, stainless steel has a high initial cost in comparison to carbon steel. However, this can be offset by lower life-cycle costs and more desirable material properties. Gardner (2005) writes that the initial cost of stainless steel products is typically about four times that of equivalent carbon steel products. The high ductility of stainless steel is advantageous for energy dissipation under cyclic and impact loading. However, the stress-strain behaviour is quite different than that of carbon steel (Bouchaïr et al., 2008). The stress-strain curve of stainless steel is rounded and lacks a clear yield point, as shown in Figure 2.4. In addition, stainless steel tends to exhibit anisotropic and non-symmetric stress-strain behaviour in tension and compression (Gardner, 2005). It retains its strength and stiffness better than carbon steel at high temperatures, however, making it much more fire resistant. Stainless steel possesses an attractive surface finish, which does not deteriorate over time, and it does not require any protective coatings due to its excellent corrosion resistance. Certain environments, such as those containing high concentrations of chlorides, can be detrimental to the corrosion resistance of stainless steel and it's resistance to stress-corrosion cracking, and it is important to select an appropriate grade of stainless steel for such applications (Gardner, 2005). The fatigue performance of stainless steel is comparable to that of carbon steel. However, it is also more susceptible to creep (Bouchaïr, Averseng, & Abidelah, 2008; Gardner, 2005). Caution must therefore be used when stainless steel is subjected to high sustained load levels.

A relatively new development in structural fastening systems is the blind fastener, which has potential to play an important role in accelerated bridge construction and modular structures. The term blind fastener is typically used to describe any fastener that can be installed from one side of a connection without needing to access the opposite side. An example of a structural application where blind fasteners are useful is for fastening members to hollow sections. Such connections have been studied by Lee et al. (2010; 2011). Several types of blind fasteners are commercially available, including rivets, anchors, and bolts. Blind bolts are generally the most suitable type of

blind fastener for structural applications, particularly for those that require pre-tensioned bolts. A blind bolting system, which appears to have good potential for use in aluminum bridge applications, is the ONESIDE™ system by Ajax Fasteners of Australia. This particular system includes a washer on each side of the connection, which is a requirement of CSA S6 for all aluminum connections (CSA Group, 2014). The Ajax blind bolts are also compliant with ASTM A325M, which is another requirement of CSA S6 (Ajax Fasteners, 2017).

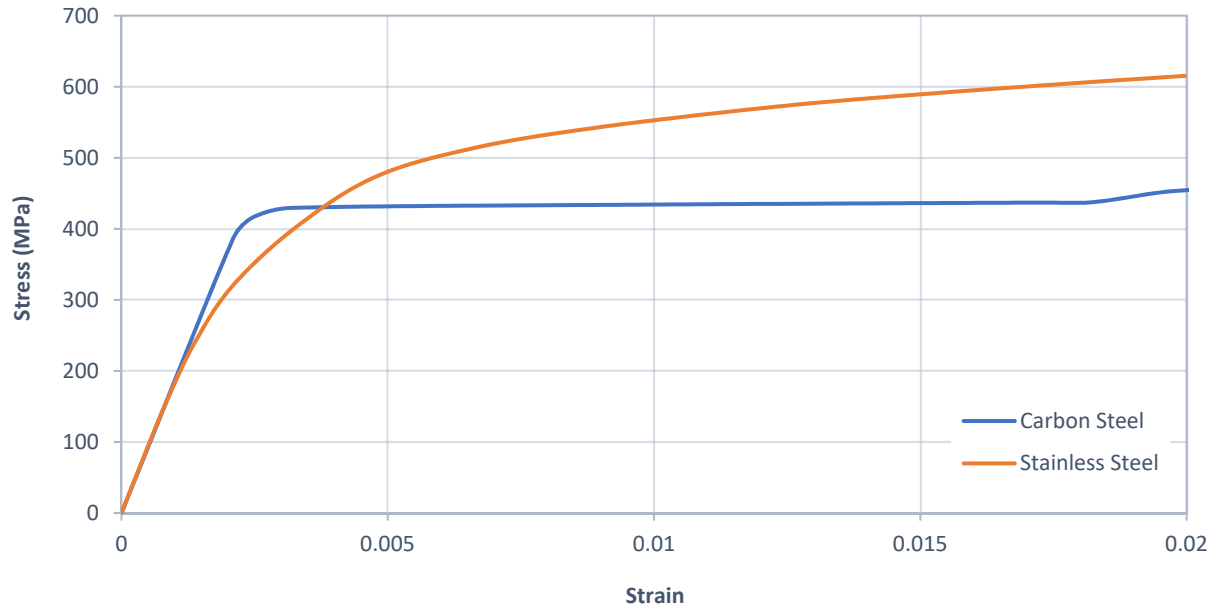


Figure 2.4: Comparison of stress-strain behaviour for carbon steel and stainless steel (Adapted from: Gardner, 2005)

The ONESIDE™ fastening system consists of a circular-headed bolt, a folding stepped washer, a solid stepped washer, a hexagonal nut, and an optional shear sleeve, as shown in Figure 2.5. A specialized tool is required for installation, as shown in Figure 2.6. The installation tool is used to insert a bolt and folded washer through an oversized hole. The tool is then rotated, which causes the folded washer to unfold, and the bolt is pulled back through the hole. The shear sleeve, solid washer, and nut are then slid onto the bolt, and the nut is tightened to complete installation. The optional shear sleeve takes advantage of the oversized hole, which is required for installation, by effectively increasing the shear capacity of the bolt. In addition to the standard ONESIDE™ blind bolt, Ajax also offers a tension control version to aid with the bolt pre-tensioning process.

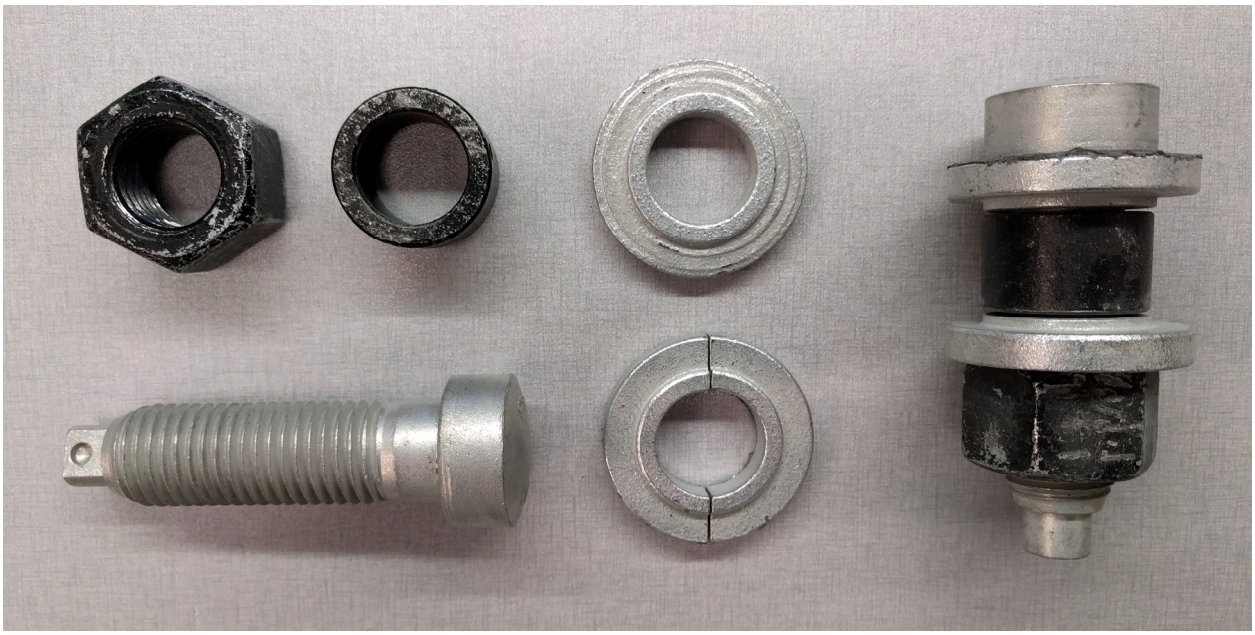

Figure 2.5: Ajax ONESIDE$^{TM}$ blind bolts; disassembled (left), assembled (right)


Figure 2.6: Ajax blind bolt installation tool

## 2.4 Slip-Resistant Connections

Slip-resistant connections, also referred to as slip-critical connections, are used in scenarios where undesired structural behaviour may occur as a result of connection slippage under service loads. These connections rely on friction between faying surfaces to resist slip at the service limit state. The required levels of frictional resistance are achieved through the use of pre-tensioned bolts,

which apply a clamping force on the connecting components. For aluminum structures, CSA S6 specifies that all connections that resist shear between connected components must be designed as slip-critical unless otherwise approved, and that the faying surfaces of slip-critical connections must be prepared by sand-blasting or other equivalent treatment to achieve a frictional coefficient of at least 0.3 (CSA Group, 2014). The code also specifies that all bolts used for aluminum slip-critical connections must conform to ASTM A325M with a zinc-coating and must be pre-tensioned to at least 70% of their minimum specified tensile strength using the turn-of-nut method (CSA Group, 2014). Connections that are designed to resist slip at the service limit state must also be designed to resist shear and bearing failure at the ultimate limit state.

The slip-resistance of a slip-critical connection can be calculated from first principles using Equation 2.1, which is presented in *High Strength Bolting for Canadian Engineers* (Kulak, 2005). The design equation for aluminum slip-critical connections provided by CSA S6 is given by Equation 2.2 (CSA Group, 2014). The design equation is similar to Equation 2.1. However, the summation of bolt tensile forces has been replaced with the product of nominal cross-sectional bolt area, minimum specified bolt tensile strength, and number of bolts. The coefficient of 0.15 found in the design equation comes from the product of $0.3 \cdot 0.7 \cdot 0.75 \cdot c_1$, where 0.3 is the minimum allowable coefficient of friction, 0.7 is a multiplier for $F_u$ which reflects the requirement that the minimum bolt pre-tension must be at least 70% of the minimum specified bolt tensile strength, 0.75 is a reasonable conversion from nominal bolt area to stress area, and $c_1$ is a coefficient that is used to relate the coefficient of friction and initial specified bolt tension to achieve an acceptable probability of slip (Kulak et al., 2001; Kulak, 2005). Since the frictional coefficient of 0.3 is built into the design equation, no benefit can be gained by achieving a frictional coefficient greater than 0.3. CSA 157 (CSA Group, 2005) provides a design equation for aluminum slip-critical connections that is similar to Equation 2.2, however the $n$ term, which accounts for the number of bolts used in a given connection, is absent.

$$P = k \cdot m \cdot \sum T_i \tag{2.1}$$

where:

$P$ = Connection slip resistance
$k$ = Coefficient of friction
$m$ = Number of slip planes
$T_i$ = Bolt pre-tension in each bolt

$$V_S = 0.15 \cdot n \cdot m \cdot A_b \cdot F_u \tag{2.2}$$

where:

$V_S$ = Connection slip-resistance
$n$ = Number of bolts
$m$ = Number of slip planes
$A_b$ = Nominal cross-sectional area of bolts
$F_u$ = Minimum specified bolt tensile strength

In recent years, several innovative methods have been proposed to improve the performance of slip-critical connections. In 2013 and 2014, Charles-Darwin Annan and Albert Chiza presented research on the use of zinc-based metallized and galvanized faying surfaces for steel slip-critical connections. It was found that metallized faying surfaces provided greater slip-resistance than the CSA S6-06 specification for an uncoated blast-cleaned surface finish, with mean frictional coefficients ranging from 0.77 to 0.98 (Annan & Chiza, 2013). In general, thicker metallized coatings resulted in greater frictional resistance. A metallized faying surface in contact with a hot-dip galvanized faying surface was found to provide a greater slip-resistance than the CSA S6-06 specification for a roughened or wire-brushed hot-dip galvanized surface finish, with mean frictional coefficient ranging from 0.49 to 0.77 (Annan & Chiza, 2014). In all cases, the steel slip-critical connections with galvanized and/or metallized faying surfaces had a greater short-term reduction in clamping force than steel slip-critical connections with uncoated blast-cleaned surfaces (Annan & Chiza, 2013; 2014). The authors note that further research is needed to study long-term creep performance under sustained loading. Fadden et al. (2015) presented research on

the use of a high performance surface coating (HPSC) for steel slip-critical connections which consisted of high-density particles suspended in a polymeric coating. When two faying surfaces with an HPSC are clamped together, the particles on each surface interlock with each other, thus increasing the coefficient of friction (Fadden et al., 2015). The amount of interlock and embedment is dependent on the concentration, size distribution, and shape of the particles. Although a 46-grit HPSC was found to provide a 31% increase in frictional resistance in comparison to a plain mill scale surface finish, a 22-grit HPSC was found to have a negative impact on frictional resistance (Fadden et al., 2015). The authors note that further research should be conducted to optimize grit interlock and embedment. Varedian (2016) presented research on the use of small metal spheres measuring 2.5 mm diameter, referred to as indenters, which were clamped between the faying surfaces of steel slip-critical connections. Aluminum oxide, stainless steel, and tungsten carbide indenters were studied, however only connections with aluminum oxide and stainless steel indenters were loaded in shear. The gain in frictional resistance was found to be dependent on the number of indenters used, as well as the initial condition of the faying surfaces, and a maximum gain of about 300% was achieved through the use of 58 stainless steel indenters (Varedian, 2016). The author notes that the aluminum oxide indenters yielded inconsistent results as they tended to crush under the clamping force.

# 3 Ridge Geometry Study

This chapter describes a parametric study, which was used to assess the impact of ridge geometry on the performance of aluminum ridged slip-resistant connections. First, the finite element (FE) models that were used for the study are presented, along with the process that was used to automate the creation of the models. The results of the study are then presented and discussed.

## 3.1 Finite Element Modelling

The parametric study was carried out using simple 2D FE models, which were created using the ABAQUS software suite by Dassault Systèmes. The general arrangement of a typical model is shown in Figure 3.1. In this figure, a 2D model is shown, which consists of two plates with interlocking ridges in contact with each other and subjected to a clamping pressure and tensile load.

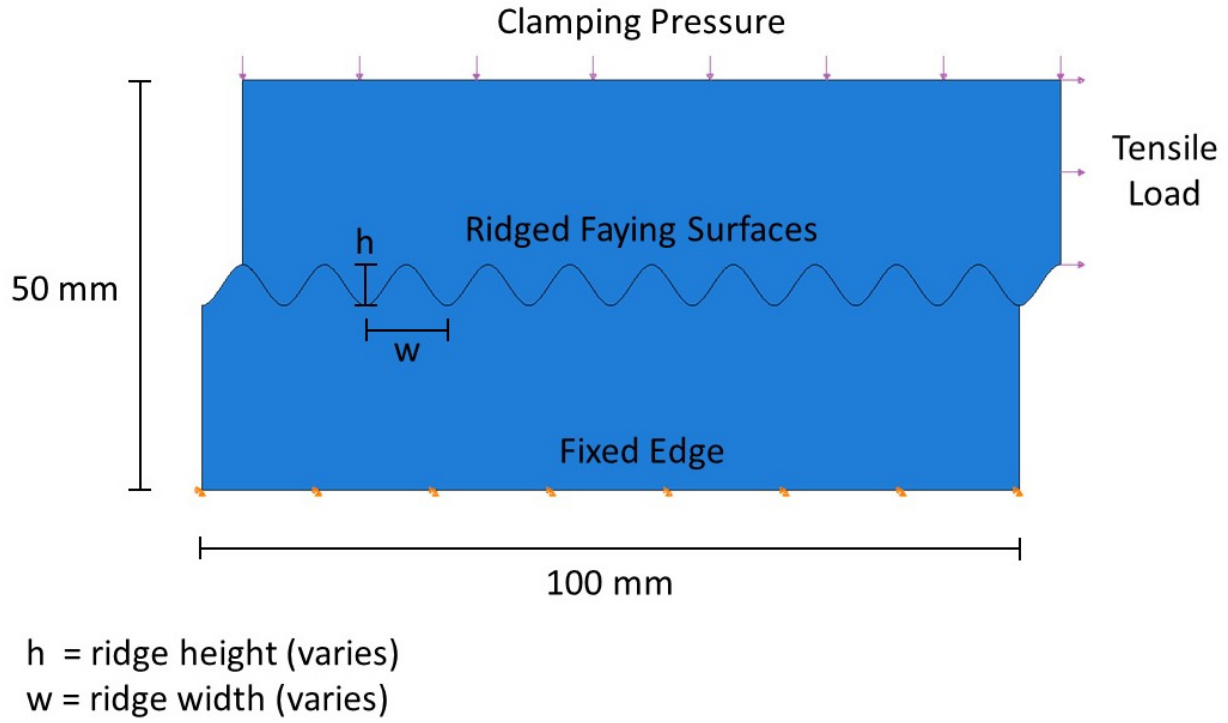


Figure 3.1: General arrangement of FE models used for parametric study

The modelled plate material was 6061-T6 aluminum, with assumed linear elastic material behaviour. The aluminum was defined as having an elastic modulus of 68.9 GPa and a Poisson's

ratio of 0.33. Hard contact was specified for the normal behaviour of the faying (contact) surfaces using the penalty constraint enforcement method with linear contact stiffness. Contact separation was enabled so that only compressive forces could be transferred between the faying surfaces, and any tensile forces would result in surface separation. The penalty friction formulation was selected for the tangential behaviour of the faying surfaces with an isotropic coefficient of 0.3, which corresponds to the minimum allowable coefficient of friction for aluminum slip-resistant connections as specified by CSA S6 (CSA Group, 2014). A fixed displacement boundary condition was applied to the bottom surface of the lower plate and a uniformly distributed clamping pressure was applied to the top surface of the upper plate. The clamping pressure was applied so that the total clamping force would be equal to 10 kN for an out-of-plane thickness of 100 mm.

Quadratic plain strain triangular elements (CPE6) were used for each model with an average element size of approximately 0.5 mm. A typical FE mesh is shown in Figure 3.2 for a single plate. Implicit time integration was adopted using the built-in implicit solver and general static time steps. The clamping pressure was applied in the first time step of the analyses using linear load increments. Contact stabilization was used for the faying surfaces in this step in order to achieve a converged solution. This contact control introduces viscous damping terms to the governing equilibrium equations so that a state of equilibrium can be obtained and the equations can be solved (Dassault Systèmes, 2013). Without contact stabilization, it would not have been possible to obtain a converged solution to the contact problem because the top component lacked the boundary conditions necessary to prevent rigid body motion prior to the application of the clamping pressure. A tensile load was applied to the rightmost surface of the upper plate in the second time step using a uniformly distributed pressure and linear load increments.

## 3.2 Mesh Refinement Study

A mesh refinement study was performed for the models that were used in the parametric study to confirm that the meshes were fine enough to produce converged results. Four models were selected for the mesh refinement study that captured a range of ridge aspect ratios. It was found that doubling the number of elements in each of the four models resulted in a change of at most 8% in the maximum von Mises stress values. Although this demonstrated that the stress results were not fully converged for the meshes used in the parametric study, it was determined that the meshes

were able to provide satisfactory results with a good balance between accuracy and computation time. Doubling the number of elements had a negligible impact on the load-displacement behaviour of the models, which was expected since displacement values are known to converge much faster than stress values.

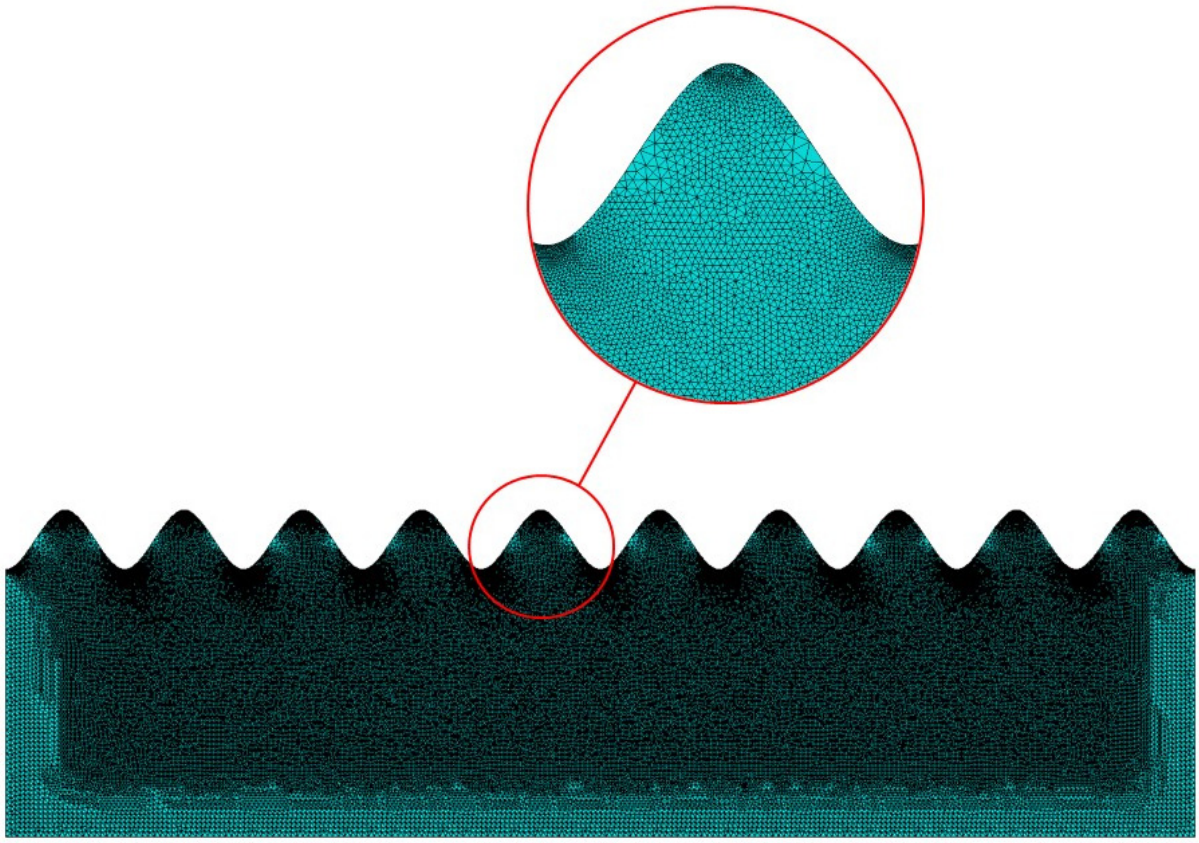

Figure 3.2: Typical FE mesh used for parametric study

### 3.3 Model Validation

A baseline connection model with flat faying surfaces was created to confirm the accuracy of the modelling techniques that were used for the contact behaviour between the faying surfaces. The only difference between the baseline model and the ridged models that were previously described was the lack of ridges on the faying surfaces. When two flat plates are clamped together, the theoretical slip-resistance of the connection can be computed as the product of the clamping force and the frictional coefficient of the faying surfaces. Since a clamping force of 10 kN was applied to the connection with a frictional coefficient of 0.3, the expected slip-resistance of the baseline

connection model was therefore 3 kN. The baseline FE model predicted a slip load of 3.00 kN, which is in line with the theoretical solution.

### 3.4 Automation

A series of VBA macros and python scripts were created to fully automate the parametric study process. A user of the macros only needs to input the desired plate length and thickness for the connection to be studied, along with the range of ridge widths and heights to be analyzed. Given this information, a VBA macro in Microsoft Excel is used to generate nodal coordinates for the geometry of each FE model that is to be created. A VBA macro in AutoCAD is then used to generate a 2D sketch of each model based on the nodal coordinates that are imported from Excel. The curved ridges are created by fitting third-order spline curves between the nodes. A python script is then executed in ABAQUS which automatically builds and analyzes an FE model for each connection in the study by importing the 2D sketches. The script builds the models and queues submissions to the kernel simultaneously, and can run multiple analyses in parallel to maximize efficiency based on the computational resources available. Once all of the simulations are completed, a second python script is used to extract and compile all of the desired data from the models.

### 3.5 Results

A total of 152 FE models were analyzed for the parametric study with ridge widths ranging from 2 mm to 50 mm and ridge heights ranging from 1 mm to 15 mm. The four extreme geometries are shown in Figure 3.3. The slip load of each model was taken as the magnitude of the applied tensile load at the point when the FE solution diverged and a state of equilibrium could no longer be maintained. The magnitude of the maximum von Mises stress along the faying surfaces was extracted from each model at the point in time just prior to slip. These stress values were plotted against the slip loads for each model as shown in Figure 3.4. A clear relationship can be seen between the slip loads and the maximum von Mises stress values. However, the degree of scatter tends to increase as the slip loads and stress values increase. This can be attributed to computational errors in the connection models with the largest geometric discontinuities. In this study, the largest geometric discontinuities were present in the models that had the sharpest ridges (For example, ridges that were 2 mm wide and 15 mm tall). These connections were generally able to carry the

greatest amount of load prior to slip. However, the severe geometric discontinuities resulted in unreliable predictions of stress. More reliable results could have been obtained by using finer meshes and incorporating non-linear material behaviour. However, this was deemed not feasible due to the increase in computation time that would have been required. The von Mises stress values exceeded the yield strength of aluminum in a number of models, and the stress results from these models in particular are therefore questionable. However, the overall load-displacement behaviour of the models was deemed to be satisfactory for the purpose of a preliminary study and comparison of ridge geometry effects.

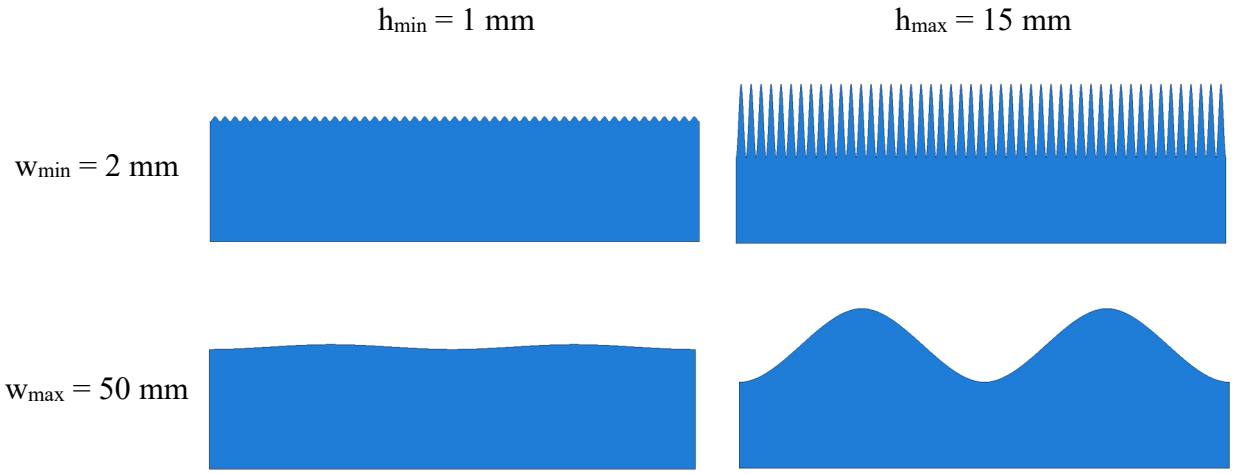


Figure 3.3: Range of Ridge Geometries in Parametric Study

The magnitude of the maximum von Mises stress along the faying surfaces was extracted from each model at the point in time between the application of the clamping pressure and the application of the tensile load. These stress values were plotted as a function of the ridge width and height for each of the models as shown in Figure 3.5. Clear relationships can be seen between the maximum stress values and the ridge geometry from inspecting this figure. The stress values generally increase as the ridge height is increased, and decrease as the ridge width is increased. This relationship can be demonstrated further by plotting the maximum von Mises stress values against the ridge aspect ratio for each model as shown in Figure 3.6. It is clear that the maximum stress on the faying surfaces increases drastically as the ridge aspect ratio is decreased and the ridges become more distorted. A similar trend can be seen between the slip loads and the ridge aspect ratios as shown in Figure 3.7.

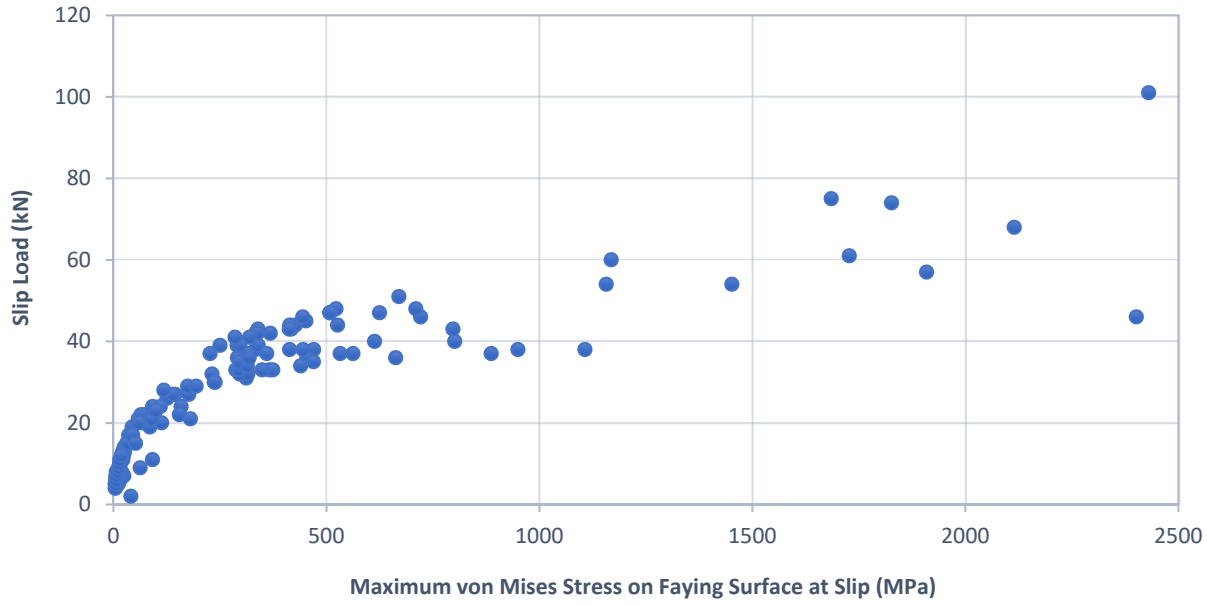


Figure 3.4: Parametric study slip loads versus maximum von Mises stresses on faying surfaces at slip

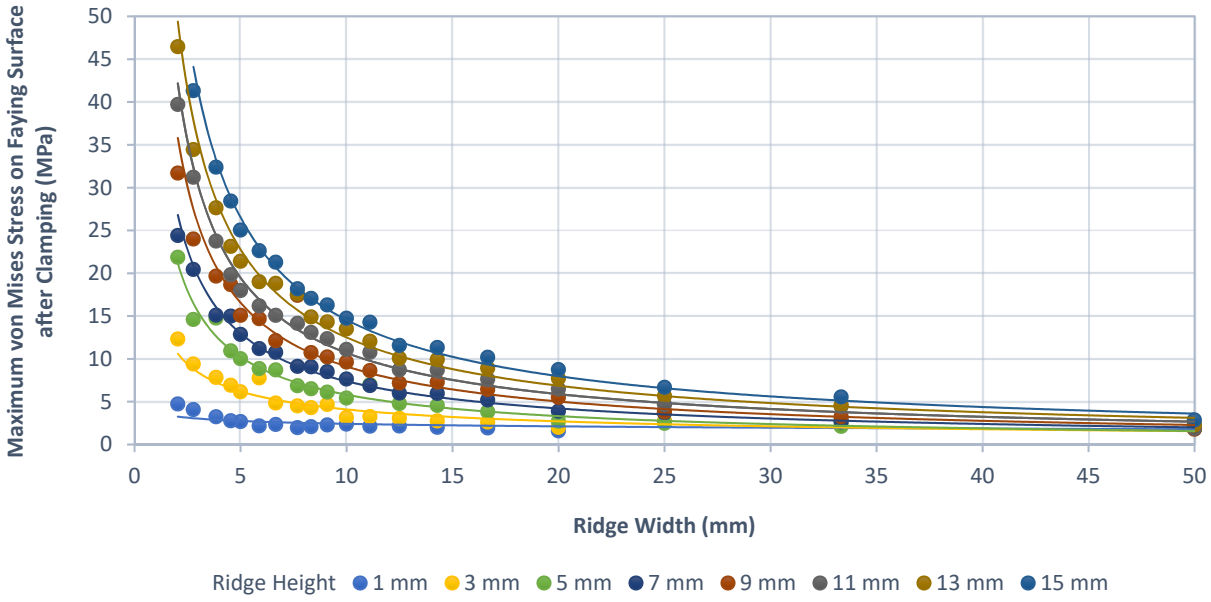


Figure 3.5: Parametric study maximum von Mises stresses on faying surfaces after clamping versus ridge geometry

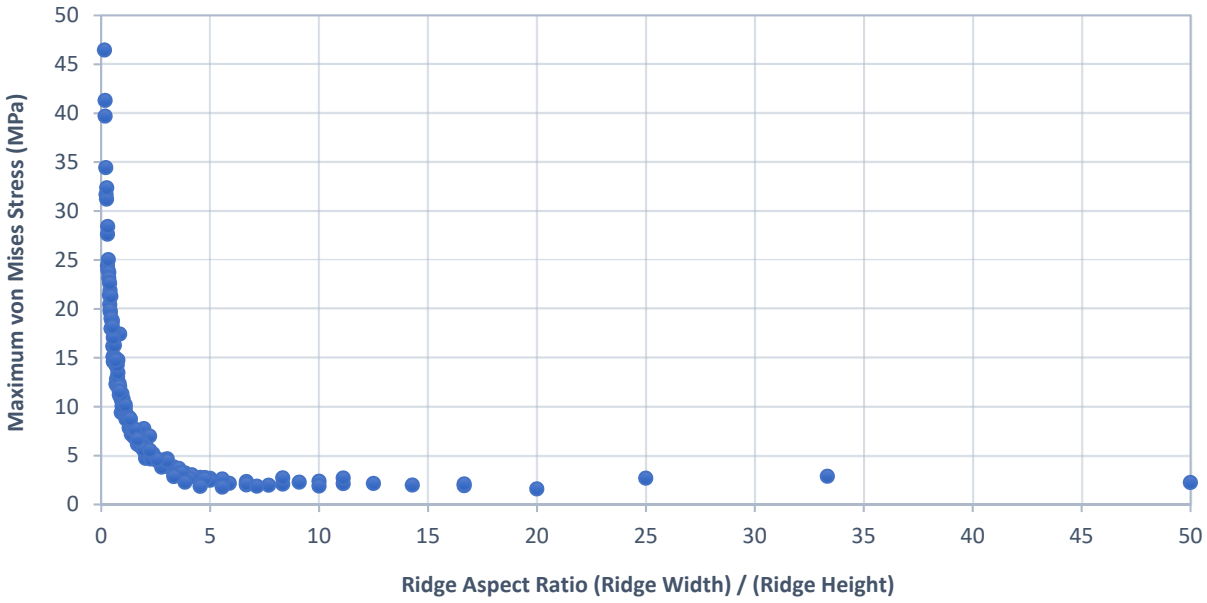


Figure 3.6: Parametric study maximum von Mises stresses on faying surfaces after clamping versus ridge aspect ratio

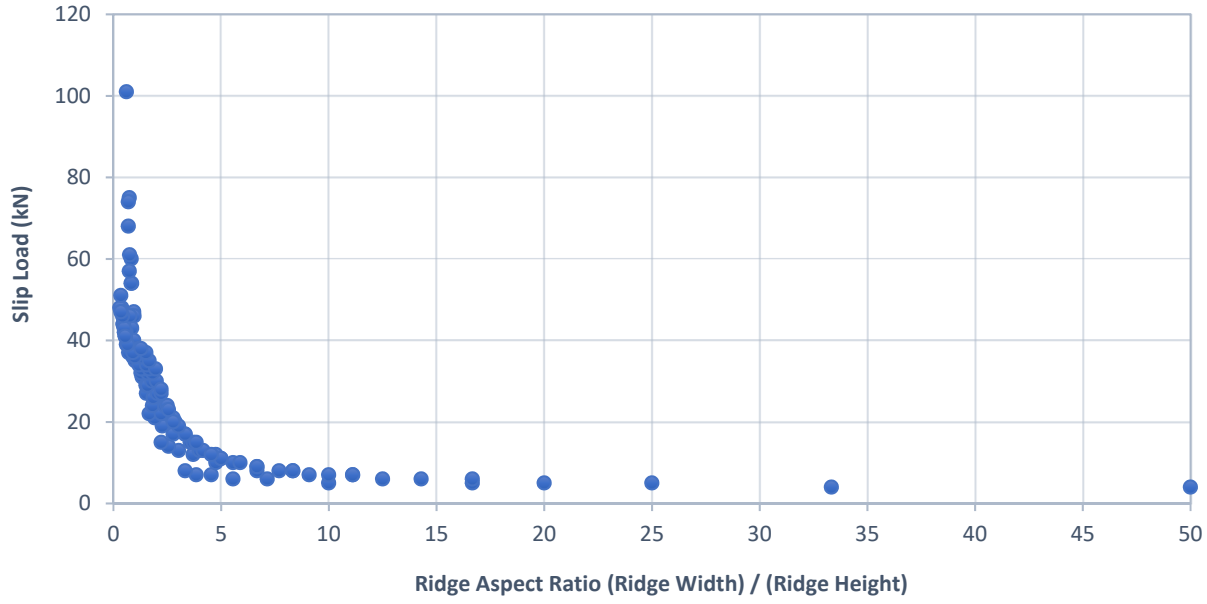


Figure 3.7: Parametric study slip loads versus ridge aspect ratio

As seen in Figure 3.7, the maximum tensile load carried by one of the connections in the parametric study prior to slip was just over 100 kN, which is more than thirty-three times the slip-resistance of the baseline connection. However, the model for this connection predicted a maximum von Mises stress of more than 2,000 MPa on the faying surfaces. Therefore, the accuracy of this result cannot be relied upon as the yield stress of the aluminum was exceeded and non-linear material properties were not considered in the model. It is likely that the connection would not be able to withstand an applied load of 100 kN in reality due to yielding. In order to select an optimal ridge geometry, both the maximum slip load and the maximum surface stress must be considered. The connection in the parametric study that had the greatest slip-resistance without yielding was able to resist a load of 37 kN just prior to slip. This is more than twelve times the slip-resistance of the baseline connection. The ridges of this connection were 5 mm in width and 7 mm in height, as shown in Figure 3.8, which corresponds to an aspect ratio of approximately 0.71. This is the optimal ridge geometry for the given model parameters, which provides the maximum slip-resistance without yielding the aluminum plates. If model parameters such as clamping pressure and material behaviour were varied in the parametric study, it is possible that different optimal ridge geometries would have been found, however it was not possible to explore every possible combination of parameters due to computational constraints. Fatigue considerations would also have an impact on the optimal ridge geometry, however fatigue was not considered in the parametric study. In addition, fabrication costs and reductions in the cross-sectional area of the base material may also affect the selection of an optimal ridge profile.

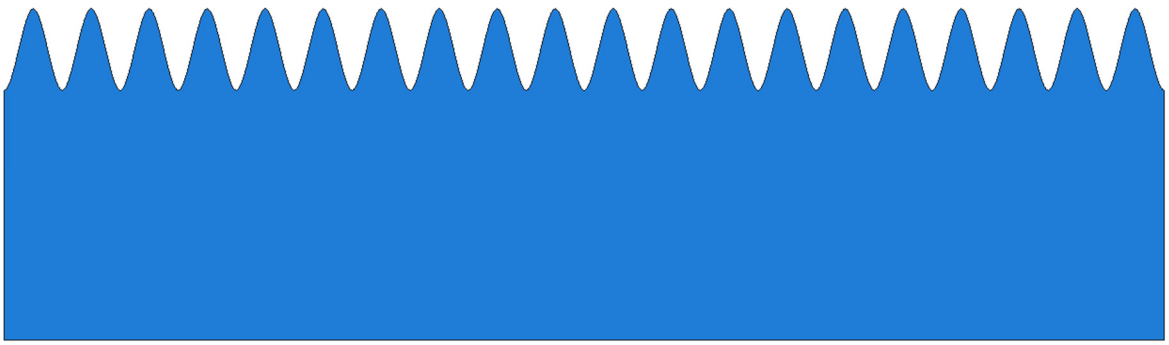

Figure 3.8: Optimal ridge geometry from parametric study

# 4 Analytical Model for Computing the Slip-Resistance of Ridged Connections

This chapter describes a simple mechanistic model, which was developed for predicting the slip-resistance of ridged slip-resistant connections. The derivation of the model is described, and the results are then compared to the finite element (FE) results presented in Chapter 3.

## 4.1 Derivation

The mechanistic model for predicting the slip-resistance of ridged connections was developed by considering the equilibrium of two rigid plates with triangular interlocking ridges. Two equilibrium equations were derived, which correspond to two possible plate orientations at slip. The first consists of two plates oriented parallel to the applied loading (Case 1), and the second consists of two plates oriented at an angle with respect to the applied loading (Case 2). This is demonstrated by the free body diagrams in Figures 4.1 and 4.2. The relative rotation between the plates and the applied loading in Case 2 would occur due to the eccentricity of the applied loading if rotation were not restrained, and is denoted as $\beta$. In both scenarios, the ridge angle is defined relative to the orientation of the plates, and is denoted as $\alpha$.

The equilibrium equations for Case 1 and Case 2 are presented as Equations 4.1-a and 4.2-a, respectively. Equations 4.1-b and 4.2-b are conditions on the respective equilibrium equations, which restrict the denominators to only positive values. If one of these conditions were to be violated by a given connection, then the slip-resistance of that connection would theoretically be infinite as it would not be possible for the applied loading to exceed the resistance provided by the frictional forces. This is only true if the connecting components are non-deformable, which was an assumption that was made in the development of the mechanistic model. Therefore, the presented equilibrium equations can only be used to predict the slip-resistance of ridged connections that satisfy the respective equilibrium conditions.

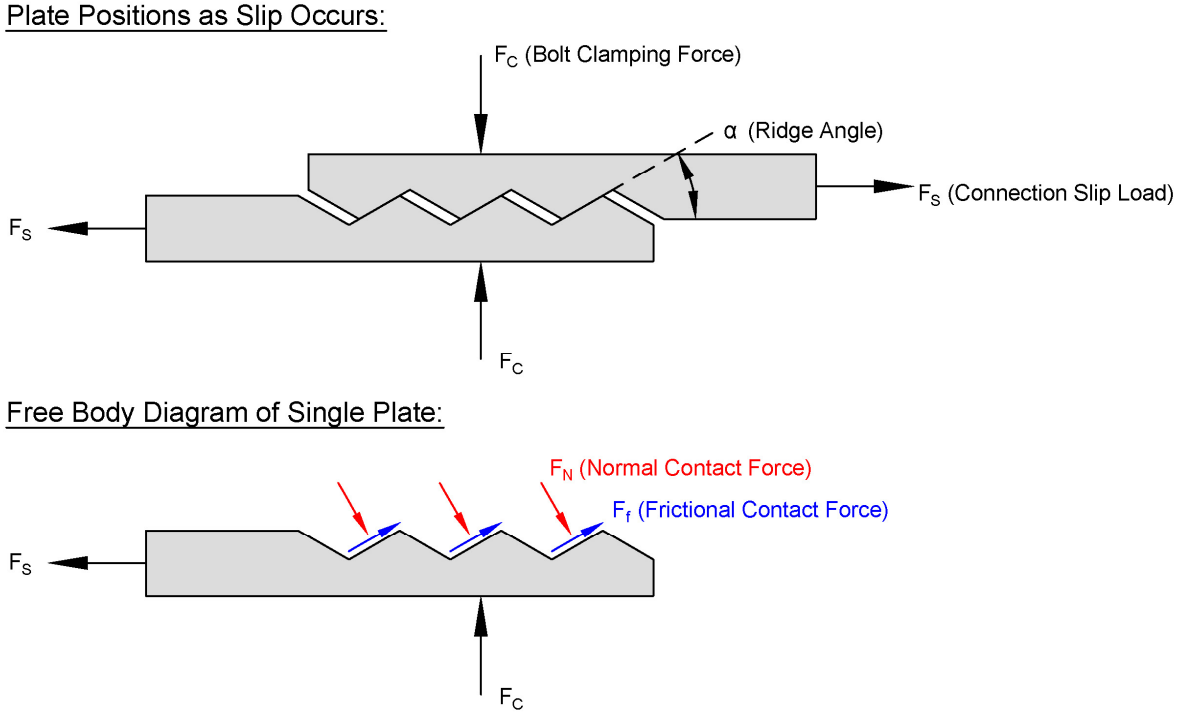


Figure 4.1: Free body diagram of ridged connection for mechanistic model (Case 1)

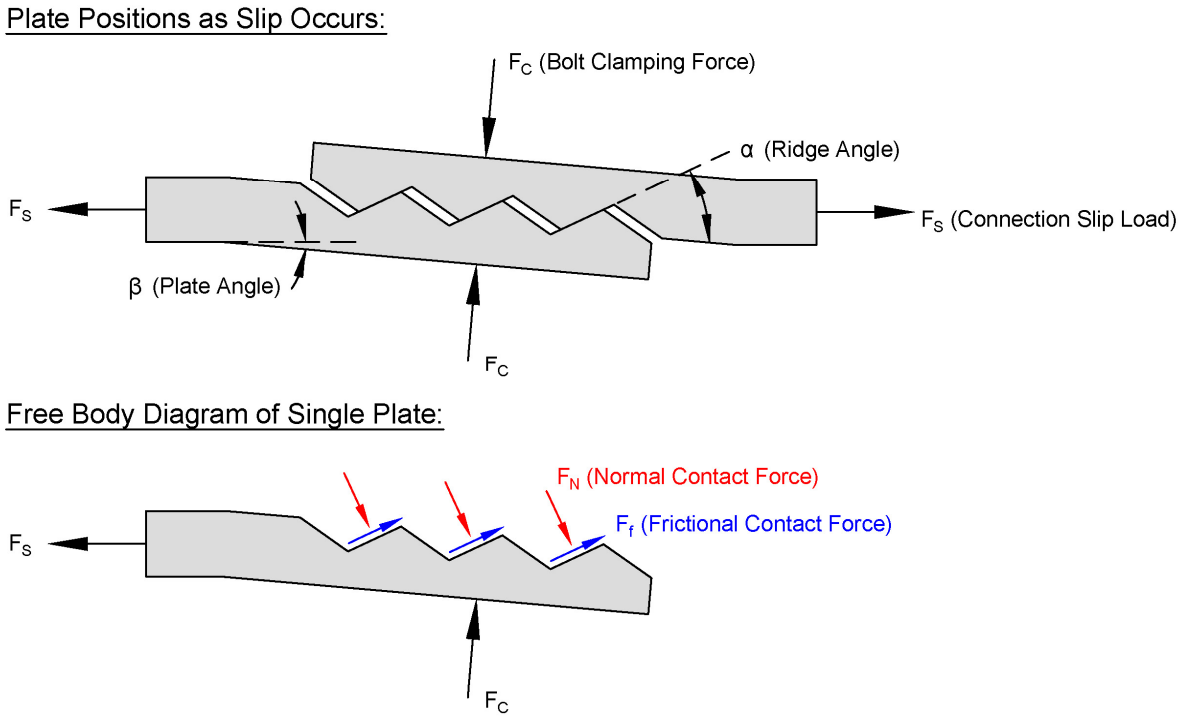


Figure 4.2: Free body diagram of ridged connection for mechanistic model (Case 2)

For Case 1:

$$F_S = F_C \cdot \left(\frac{\mathrm{Sin}(\alpha) + \mu \cdot \mathrm{Cos}(\alpha)}{\mathrm{Cos}(\alpha) - \mu \cdot \mathrm{Sin}(\alpha)}\right) \tag{4.1-a}$$

$$\mathrm{Tan}(\alpha) < {}^{1}/_{\mu} \tag{4.1-b}$$

For Case 2:

$$F_S = F_C \left[\mathrm{Sin}(\beta) + \mathrm{Cos}(\beta) \left(\frac{\mathrm{Sin}(\alpha - \beta) + \mu \cdot \mathrm{Cos}(\alpha - \beta)}{\mathrm{Cos}(\alpha - \beta) - \mu \cdot \mathrm{Sin}(\alpha - \beta)}\right)\right] \tag{4.2-a}$$

$$\mathrm{Tan}(\alpha - \beta) < {}^{1}/_{\mu} \tag{4.2-b}$$

where:

$F_S$ = Connection slip-resistance
$F_C$ = Clamping force
$\alpha$ = Ridge angle
$\beta$ = Connection angle
$\mu$ = Coefficient of friction

## 4.2 Comparison to Ridge Geometry Study

An AutoCAD VBA macro was used to estimate the slip-resistance of each connection model from the parametric study described in Chapter 3 using Equations 4.1-a and 4.1-b of the mechanistic model. For each connection, the ridge angle, α, was taken as the maximum slope along the faying surfaces, which occurs at the inflection point at the mid-height of the ridges as shown in Figure 4.3. The results from the mechanistic model are compared to the FE results in Figure 4.4, where the connections are arranged in order of increasing ridge angle. Slip loads were not computed for connections that violated Equation 4.1-b. A coefficient of friction of 0.3 was used for the parametric study, and so a connection violated Equation 4.1-b if the ridge angle exceeded 73.3°.

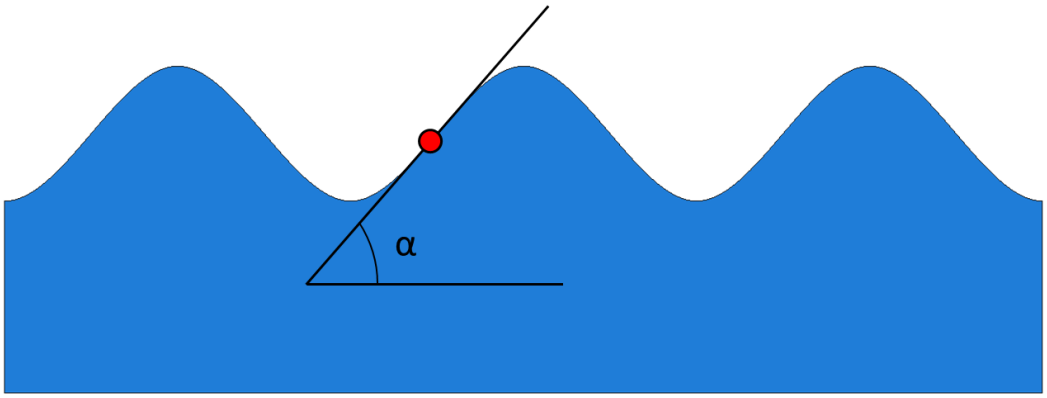


Figure 4.3: Maximum ridge angle of curved ridges used for mechanistic model

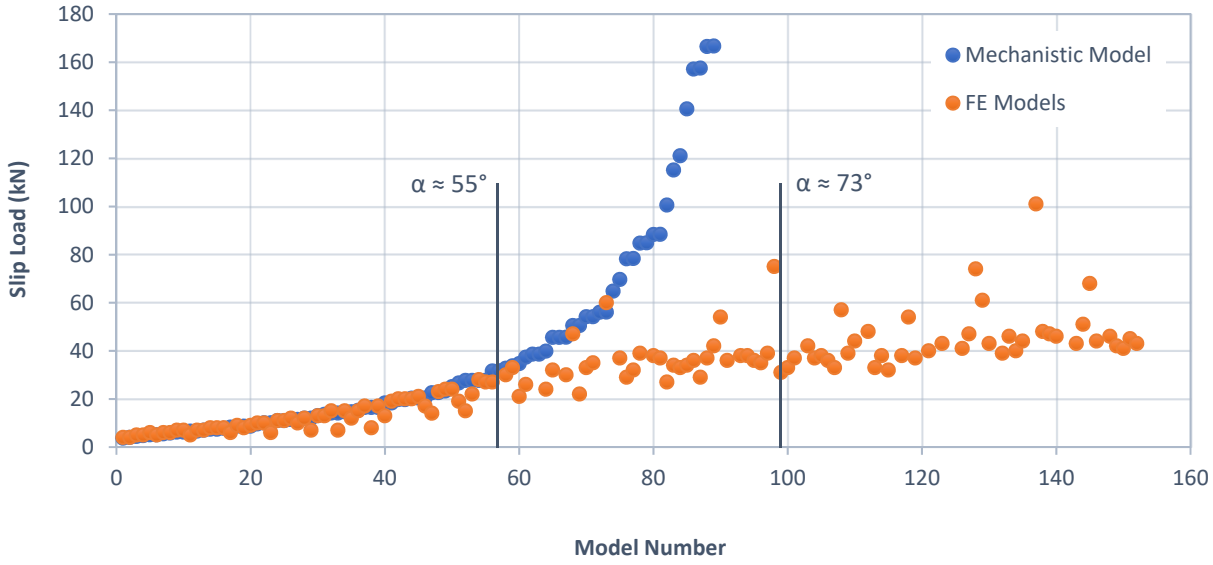


Figure 4.4: Comparison of mechanistic model results and FE results

As seen in Figure 4.4, the mechanistic model results align well with the FE results for connections with shallow ridge angles. As the ridge angle increases, the mechanistic model deviates from the FE results as it approaches a vertical asymptote at the critical ridge angle of 73.3 degrees. The FE results do not approach the vertical asymptote at the critical angle because the FE models account for material deformations that are not captured by the mechanistic model. The material deformations cause the ridges to skew as a tensile load is applied, effectively resulting in reduction of the ridge angle, and thus a reduction in slip-resistance. The amount of deformation is proportional to the magnitude of the applied load, and so the error between the mechanistic model

and the FE models increases as the ridge angle increases. Therefore, the mechanistic model can only be used to predict the slip-resistance of ridged connections with shallow angles and should be considered an upper-bound estimate for slip-resistance. Based on the results shown in Figure 4.4, the mechanistic model appears to be accurate for ridge angles less than or equal to 55 degrees, which is approximately 75% of the critical ridge angle of 73.3 degrees.

# 5 Experimental Program

This chapter describes an experimental program that was carried out to evaluate the performance of aluminum ridged slip-resistant connections. First, the test matrix is introduced, along with the geometry and material properties of the specimens. The specimen design and fabrication methods are also discussed. Next, the instrumentation used for each of the tests is described, and the typical experimental test setup is presented.

## 5.1 Test Specimens

A total of eighteen lap-splice specimens were fabricated to study the effects of four parameters on the behaviour and performance of the connections. The four parameters were faying surface geometry, faying surface finish, fastener type, and number of fasteners. The combinations of parameters are shown in Table 5.1 for each of the tests. The test program consisted of one static "pilot" test, which was used to test the experimental setup, fourteen static tests, and three constant amplitude cyclic tests. Both ridged and non-ridged surface geometries were included in the test program so that the performance of the ridged connections could be compared to that of typical slip-critical connections with flat plates. All of the test specimens with flat faying surfaces were sand-blasted in accordance with CSA S6 (CSA Group, 2014) to achieve an acceptable coefficient of friction. For the specimens with ridged faying surfaces, both sand-blasted and as-machined surface finishes were tested so that the effect of sand-blasting could be studied. Three types of fasteners were used for the test program: stainless steel bolts, galvanized carbon steel bolts, and galvanized ONESIDE$^{TM}$ carbon steel blind bolts. The ONESIDE$^{TM}$ blind bolts were generously donated by Ajax Fasteners of Australia. Although slip-resistant connections typically employ standard carbon steel bolts, carbon steel blind bolts were also included in the study because they have potential to allow for simpler and more creative connection concepts for modular aluminum bridge deck systems. Stainless steel bolts were of interest due to their excellent corrosion resistance, and they were therefore included in the study to determine whether an effective slip-resistant connection could be made with stainless steel fasteners.

Table 5.1: Test matrix for experimental program

| Test No. | Surface Geometry | | Surface Finish | | Bolt Type | | | | No. of Bolts | | Specimen Name |
|---|---|---|---|---|---|---|---|---|---|---|---|
| | Ridged (R) | Flat (F) | Machined (M) | Sand-Blasted (S) | SS | CS | BB | BS | 1 | 2 | |
| Pilot Test (P) | | | | | | | | | | | |
| 1 | * | | * | | * | | | | * | | RMSS1-P |
| Static Tests (S) | | | | | | | | | | | |
| 2 | * | | * | | * | | | | * | | RMSS1-S |
| 3 | * | | * | | | * | | | * | | RMCS1-S |
| 4 | * | | * | | | | * | | * | | RMBB1-S |
| 5 | * | | * | | | | | * | * | | RMBS1-S |
| 6 | * | | * | | * | | | | | * | RMSS2-S |
| 7 | * | | * | | | * | | | | * | RMCS2-S |
| 8 | * | | | * | * | | | | | * | RSSS2-S |
| 9 | * | | | * | | * | | | | * | RSCS2-S |
| 10 | | * | | * | * | | | | * | | FSSS1-S |
| 11 | | * | | * | | * | | | * | | FSCS1-S |
| 12 | | * | | * | | | * | | * | | FSBB1-S |
| 13 | | * | | * | | | | * | * | | FSBS1-S |
| 14 | | * | | * | * | | | | | * | FSSS2-S |
| 15 | | * | | * | | * | | | | * | FSCS2-S |
| Cyclic Tests (C) | | | | | | | | | | | |
| 16 | * | | * | | * | | | | * | | RMSS1-C |
| 17 | * | | * | | * | | | | * | | RMSS1-C |
| 18 | * | | * | | * | | | | * | | RMSS1-C |

**Naming Convention:**

Surface Geometry - Surface Finish - Bolt Type - No. of Bolts - Test Type

**Bolt Type:**

SS - Stainless Steel BB - Blind Bolt (Carbon Steel)

CS - Carbon Steel BS - Blind Bolt with Shear Sleeve (Carbon Steel)

### 5.1.1 Design

The test specimens were designed in accordance with CSA S6 provisions for bolted connections in aluminum structures at the ultimate limit state (CSA Group, 2014). The resistance factors provided by the code were not included in the design calculations, however, as the testing was conducted in a controlled environment, and accurate – rather than safe – predictions of the failure load were needed. The aluminum plate dimensions and bolt locations were chosen so that the ultimate capacity of each specimen would be governed by bolt shear strength. The specimens with ridged faying surfaces were designed using the same provisions as the non-ridged specimens. However, the reduction in plate thickness (and therefore net cross-sectional area) due to the presence of the ridges had to be accounted for.

### 5.1.2 Fabrication

The test specimens were fabricated by the University of Waterloo Engineering Machine Shop (EMS) from 6061-T6 Aluminum plate. The faying surfaces of the ridged connections were created using a CNC machine. However, due to the limitations of the machine, it was not possible to create smooth curved ridges like those explored in the parametric study that was previously discussed in Chapter 3. Instead, a flat-topped ridge profile was adopted as shown in Figure 5.1. This profile was created using a 90° NC spot drill, which is shown in Figure 5.2. Modular aluminum bridge deck panels are typically fabricated using an aluminum extrusion process where there are essentially no limitations on the shapes that can be produced. However, this was not a viable fabrication method due to the cost of creating molds. In addition to the aluminum plates, reusable ridged steel shim plates were also fabricated to ensure proper alignment of the specimens within the test frame. These shim plates used the same ridge profile as the specimens so that they could interlock when clamped together by the grips of the test frame.

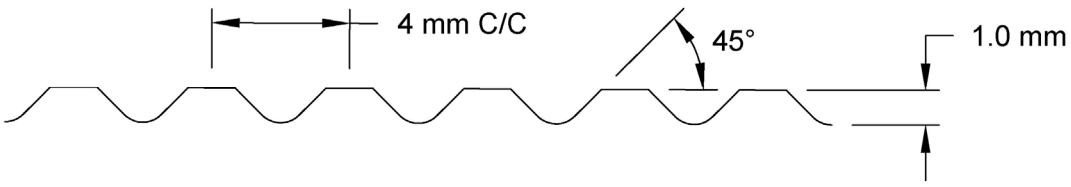


Figure 5.1: Ridge profile of specimens with ridged faying surfaces


Figure 5.2: Spot drill used to create ridge profile for test specimens

Since the various bolts used for the experimental program did not have the same thread length, some of the bolts had to be modified so that their threads intersected the shear plane formed by the connecting plates. The ½" A325 bolts and the ¾" ONESIDE™ blind bolts already had existing threads that intersected the shear plane, and so the threads of the ½" stainless steel bolts, ¾" stainless steel bolts, and ¾" A325 bolts were extended for consistency between tests. The threads of the bolts used for the fatigue tests were not modified, however, so that the fatigue performance of the bolts would not be adversely affected. Examples of unmodified and modified ¾" stainless steel bolts are shown in Figure 5.3.

Figure 5.3: ¾" stainless steel bolt with unmodified threads (top) and extended threads (bottom)

### 5.1.3 Geometry

The geometry of typical aluminum plates used for the experimental program are shown in Figures 5.4 and 5.5. Four plate styles were fabricated to accommodate the four combinations of faying surface geometry and fastener count for the specimens. An example of a fully assembled specimen with ridged faying surfaces and a single bolt is shown in Figure 5.6.

### 5.1.4 Material Properties

The material properties of the aluminum and various fasteners used for the experimental program are presented in the following subsections.

#### 5.1.4.1 Aluminum

The test specimens were fabricated from 6061-T6 aluminum plate. The properties of the 6061-T6 aluminum alloy are provided in Table 5.2. A typical engineering stress-strain curve for the alloy is shown in Figure 5.7. This curve was obtained through previous testing conducted at the University of Waterloo. The fatigue parameters for 6061-T6 aluminum are provided in Table 5.3.

#### 5.1.4.2 Fasteners

The material properties for the various bolts used in the experimental program are provided in Table 5.4. The stainless steel bolts conformed to ASTM F593 and the carbon steel bolts conformed to ASTM A325. Ajax Fasteners states that their ONESIDE$^{TM}$ blind bolts conform to ASTM A325 (Ajax Fasteners, 2017). A typical engineering stress-strain curve for austenitic stainless steel is shown in Figure 5.8. The typical curve was adjusted based on the yield strength and ultimate strength ranges provided by ASTM F593 for both the ¾" and ½" bolts. This provided upper and lower bounds for the expected behaviour of the stainless steel bolts as shown in Figures 5.9 and 5.10. A typical engineering stress-strain curve for A325 steel bolts is shown in Figure 5.11.

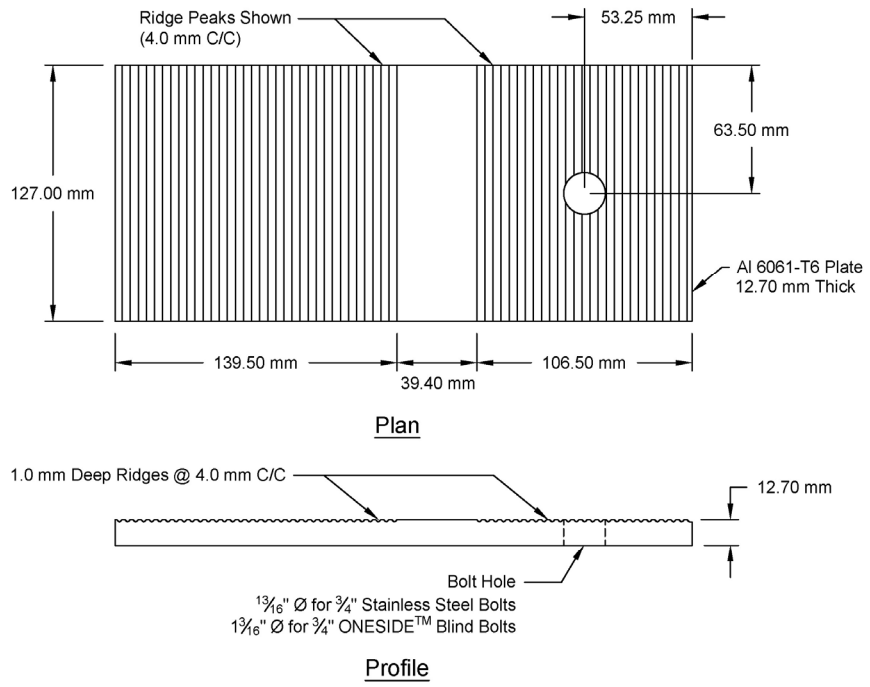


(a) Single bolt

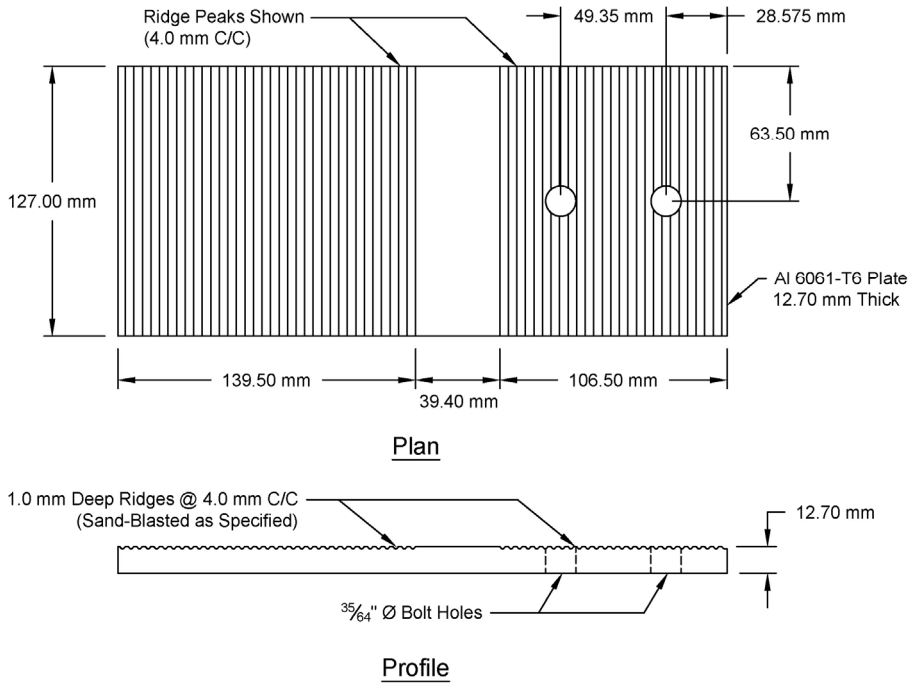


(b) Two bolts

Figure 5.4: Typical ridged aluminum plates used for experimental program

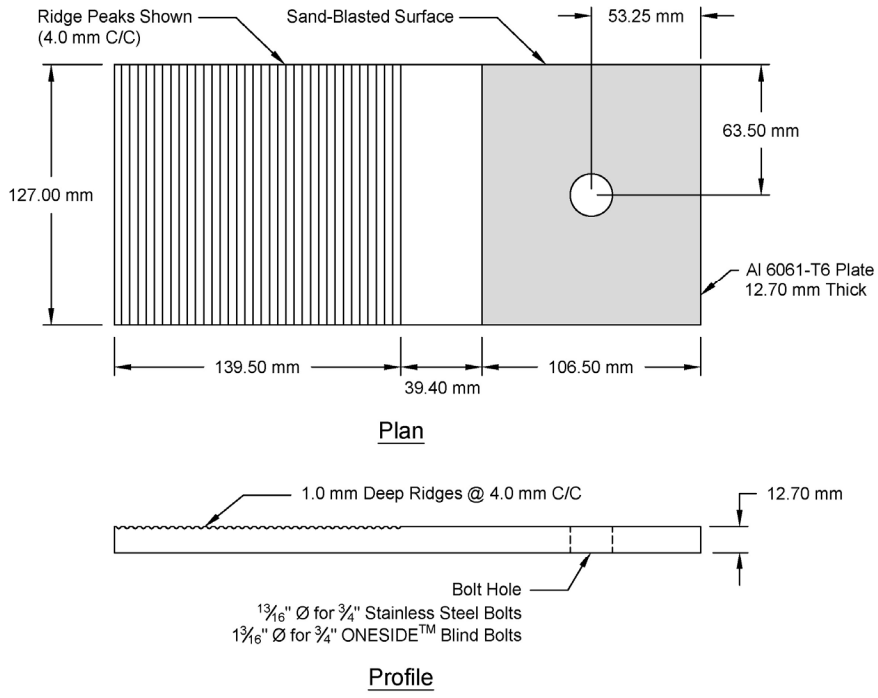


(a) Single bolt

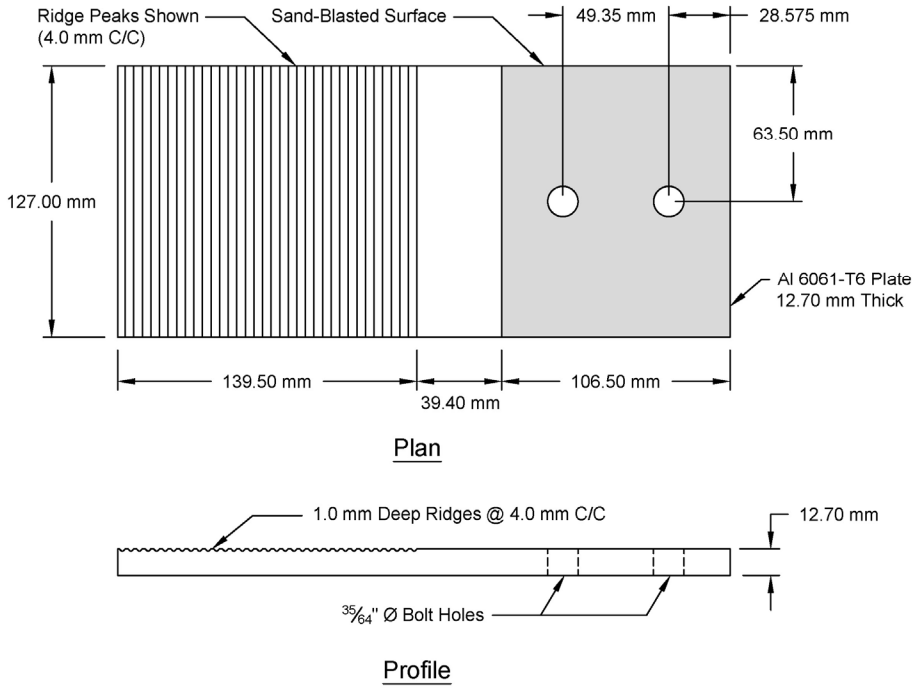


(b) Two bolts

Figure 5.5: Typical flat aluminum plates used for experimental program

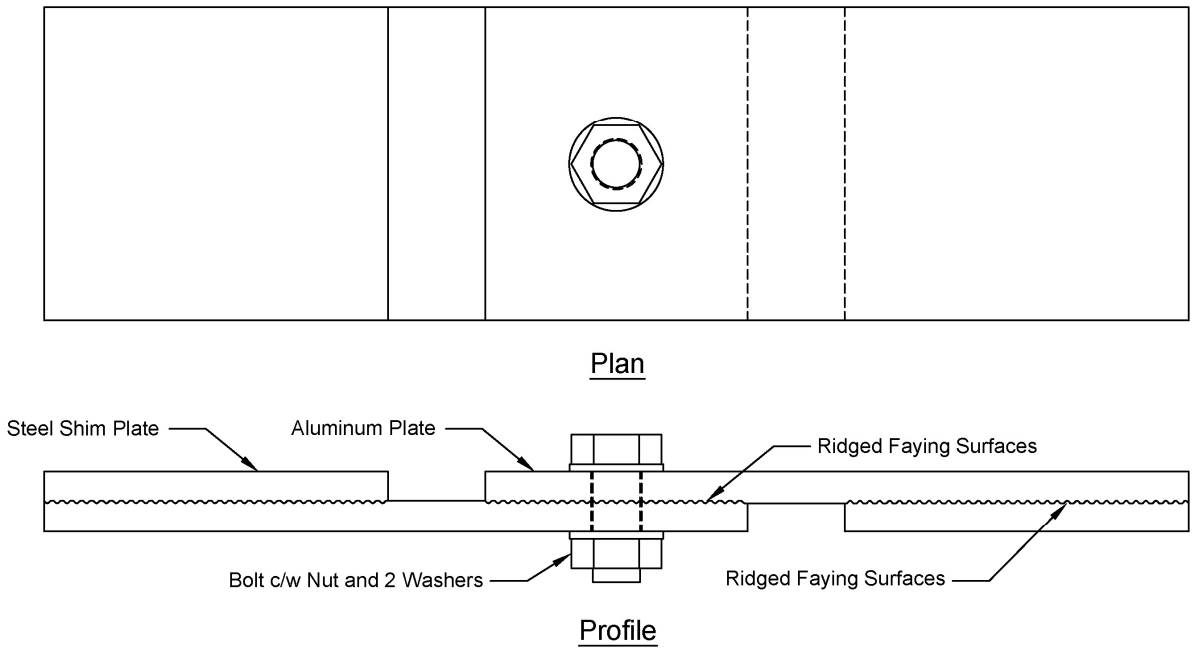


Figure 5.6: Example of a fully assembled specimen with shim plates

Table 5.2: 6061-T6 aluminum material properties (Adapted from: ASTM International, 2010)

| Property | Symbol | Value |
|---|---|---|
| Poisson's Ratio | $\nu$ | 0.33 |
| Elastic Modulus | $E$ | 69 GPa |
| Yield Strength (Min) | $F_y$ | 240 MPa |
| Tensile Strength (Min) | $F_u$ | 260 MPa |

Table 5.3: 6061-T6 aluminum fatigue parameters (Adapted from: Mirza et al., 2017)

| Property | Symbol | Value |
|---|---|---|
| Strength Coefficient | $K'$ | 369 MPa |
| Strain Hardening Exponent | $n'$ | 0.039 |
| Fatigue Strength Coefficient | $\sigma'_f$ | 534 MPa |
| Fatigue Strength Exponent | $b$ | -0.082 |
| Fatigue Ductility Coefficient | $\varepsilon'_f$ | 4.49 |
| Fatigue Ductility Exponent | $c$ | -1.10 |

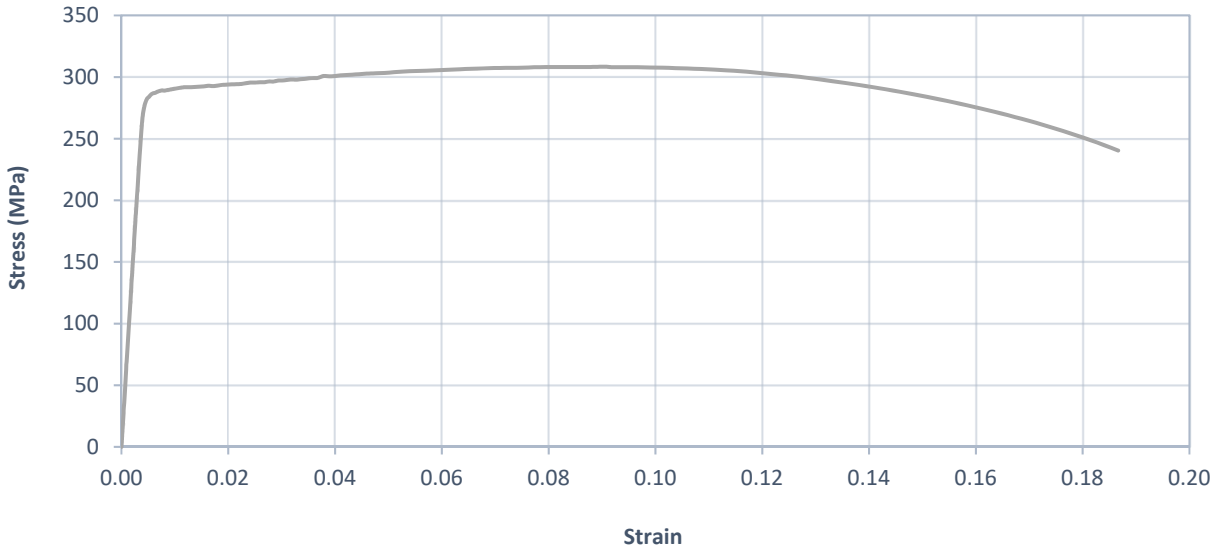


Figure 5.7: Typical engineering stress-strain curve for 6061-T6 aluminum

Table 5.4: Fastener material properties (Adapted from: ASTM International, 2017; 2015)

| Bolt Designation | Poisson's Ratio | Elastic Modulus (GPa) | Yield Strength (MPa) | Tensile Strength (Min) | Tensile Strength (Max) |
|---|---|---|---|---|---|
| F593D (¾" bolts) | 0.30 | 200 | 310 | 586 | 965 |
| F593C (½" bolts) | 0.30 | 200 | 448 | 689 | 1035 |
| A325 | 0.30 | 200 | 660 | 830 | - |

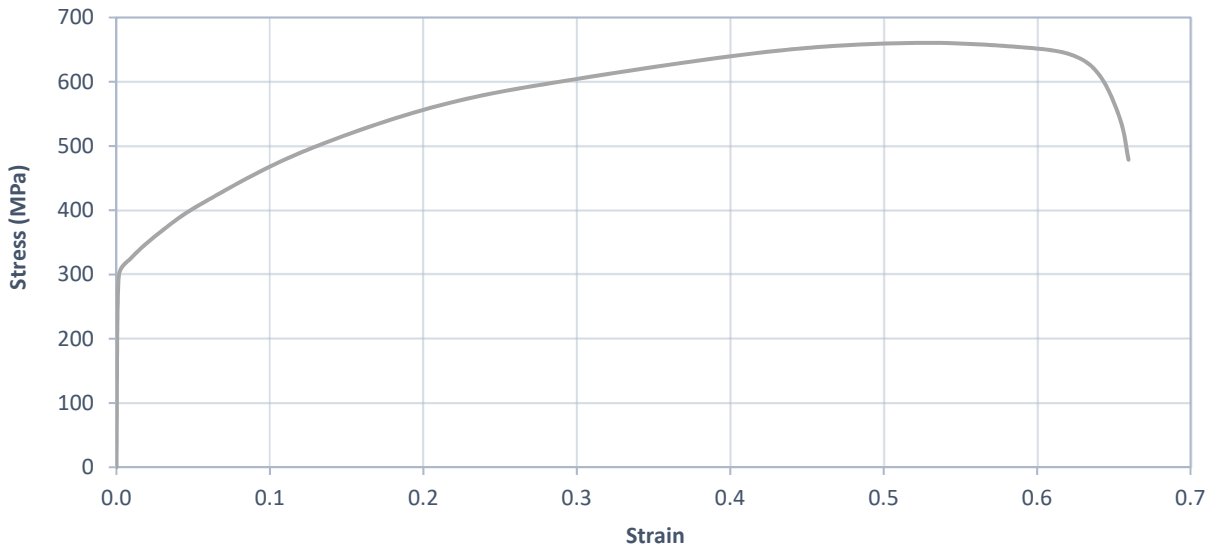


Figure 5.8: Typical engineering stress-strain curve for austenitic stainless steel (Adapted from: Arrayago et al., 2015)

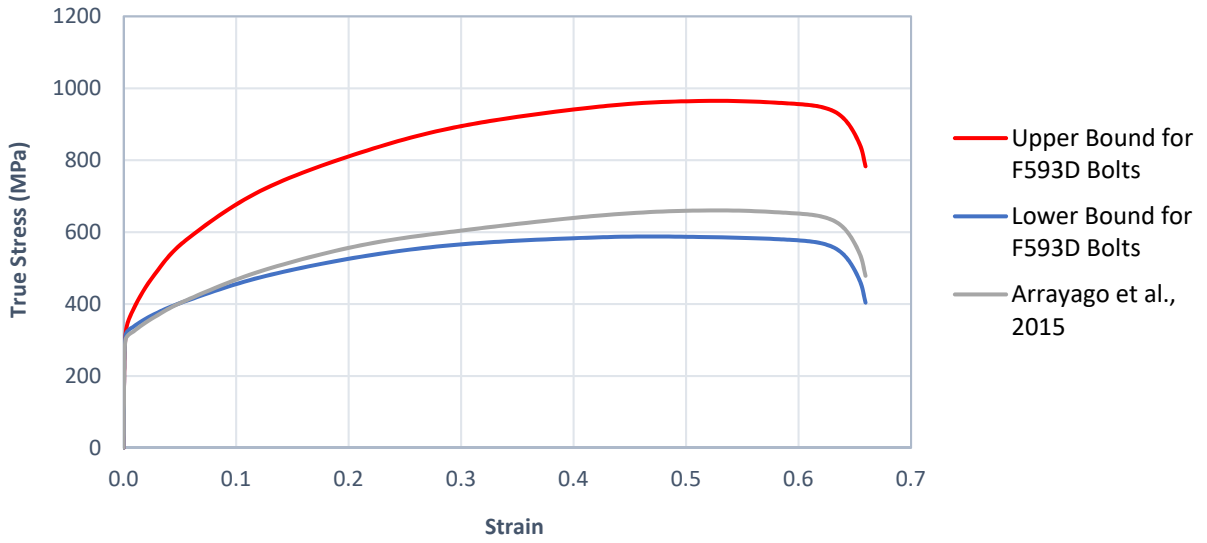


Figure 5.9: Expected range of stress-strain behaviour for F593D stainless steel bolts (Adapted from: Arrayago et al., 2015)

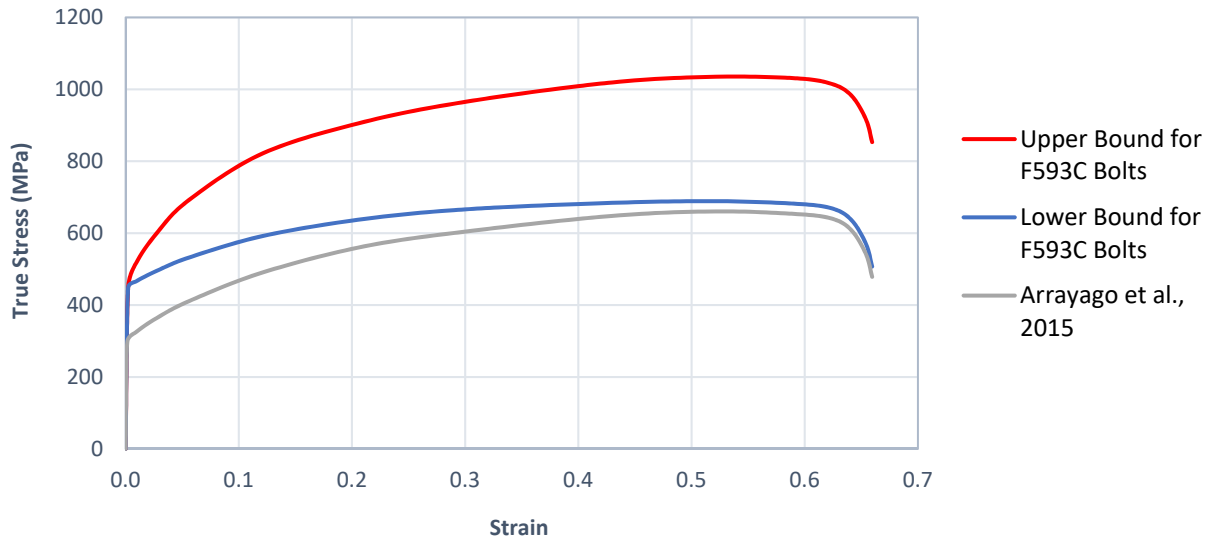


Figure 5.10: Expected range of stress-strain behaviour for F593C stainless steel bolts (Adapted from: Arrayago et al., 2015)

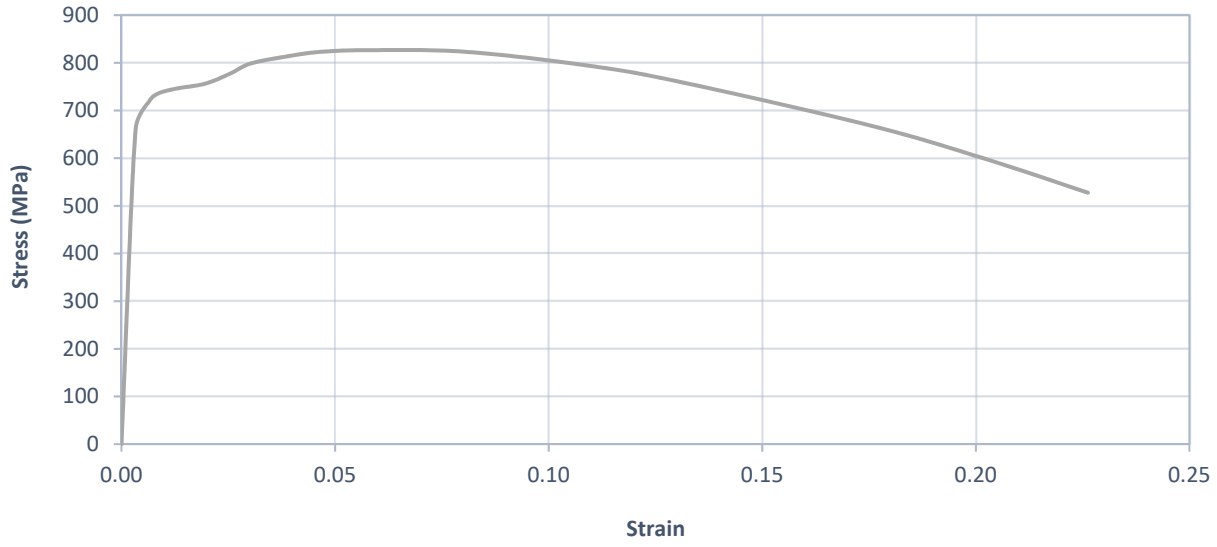


Figure 5.11: Typical engineering stress-strain curve for A325 bolts (Adapted from: Kulak, 2005)

### 5.1.5 Bolt Pre-Tensioning

Each bolt was pre-tensioned to at least 70% of its minimum specified tensile strength using the turn-of-nut method in accordance with CSA S6 (CSA Group, 2014). The code specifies that ¾" bolts must be rotated 120° past their snug-tight position and ½" bolts must be rotated 180° past their snug-tight position. The tolerance on the rotation is +30°. Snug-tight is defined as the tightness of a bolt that is attained after a few impacts of an impact wrench, or by the full effort of a person using a spud wrench. To ensure that the same level of pre-tension was achieved for each bolt, a torque wrench was used to determine the torques that corresponded to the snug-tight conditions for each diameter of bolt. The snug-tight torques were found to be 150 lb-ft for the ¾" bolts and 80 lb-ft for the ½" bolts. A torque wrench was used to tighten each bolt to the corresponding torque before applying the specified angle of rotation. The rotation was applied by rotating the head of the bolt with a wrench, while the nut was held stationary with a second wrench. Markings on the specimens were used to ensure that the bolt heads were rotated by the correct angle as shown in Figure 5.12 for a single ¾" bolt. In the event that a nut slipped during rotation, the head of the bolt was rotated an additional amount corresponding to the angle of slip.

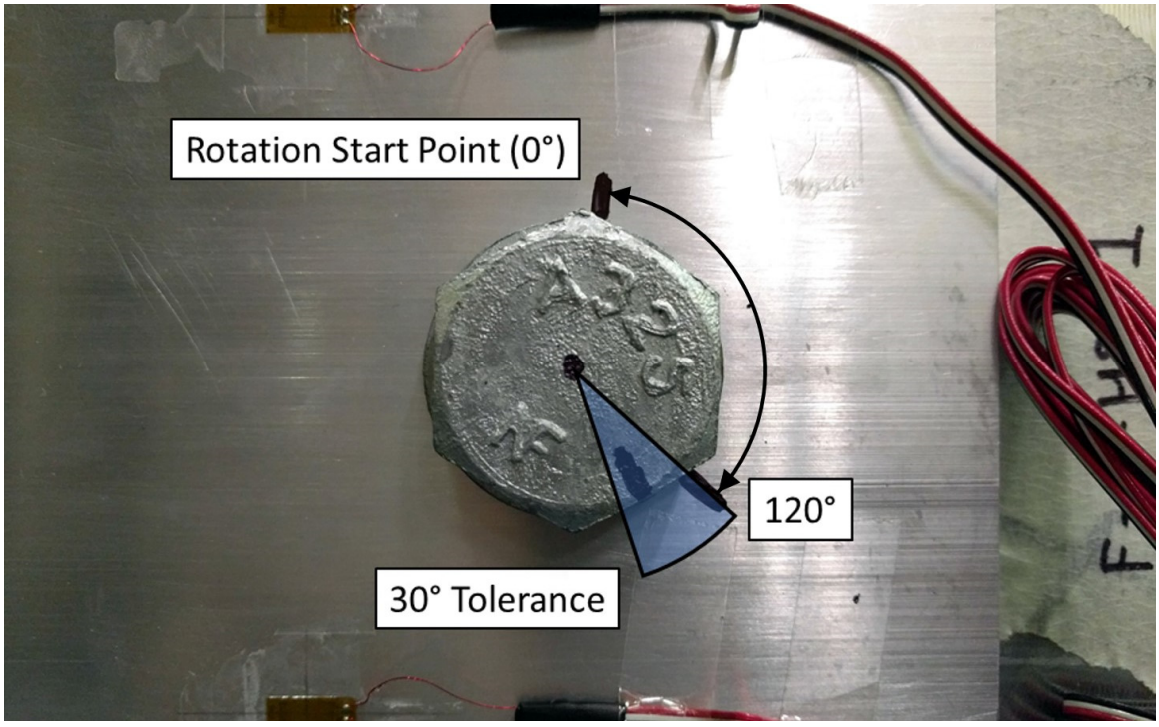


Figure 5.12: Bolt pre-tensioning

## 5.2 Instrumentation

The typical instrumentation that was used for the experimental program is described in the following subsections.

### 5.2.1 Physical Measurement

Four strain gauges were affixed to each specimen in the arrangement shown in Figure 5.13. The purpose of these gauges was to determine whether each specimen was properly aligned within the test frame. Under ideal circumstances, all four gauges should have measured the same strain value throughout each test, and any deviations indicated misalignment of the specimen. In addition, a linear variable differential transformer (LVDT) was fastened to each specimen to measure the relative displacement of the aluminum plates. Aluminum clamps and a protective housing were specially fabricated to fasten the LVDT to the specimens as shown in Figure 5.14.

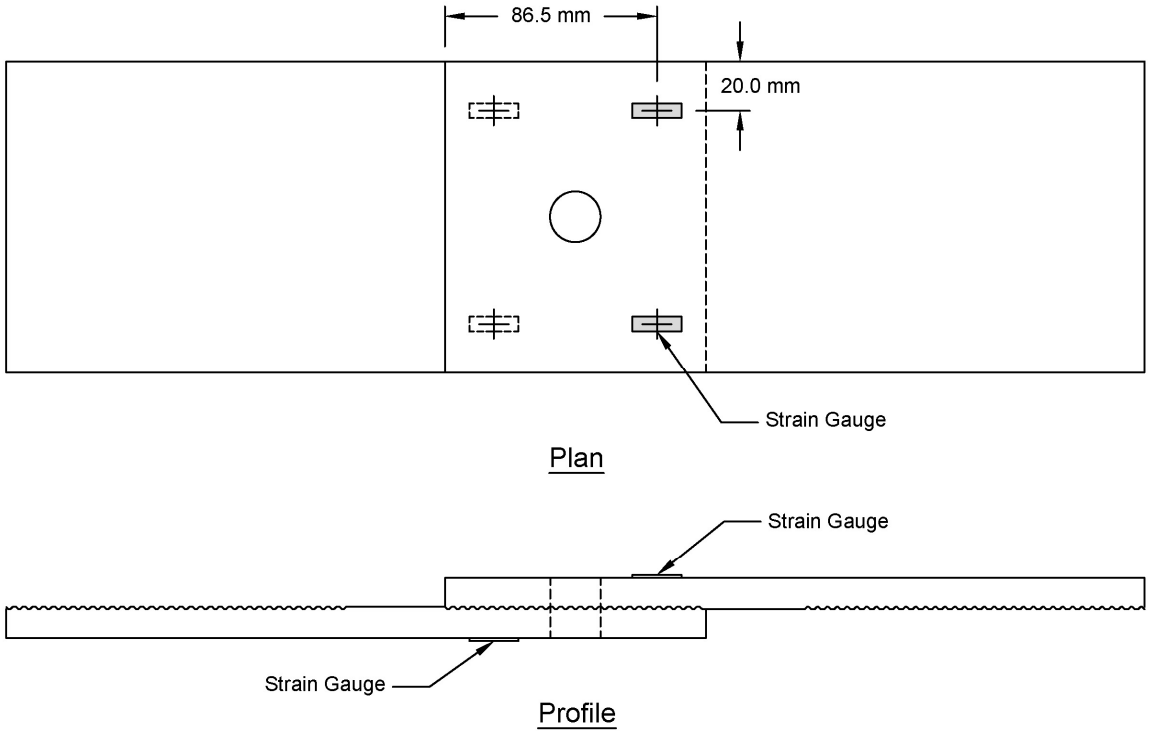


Figure 5.13: Typical arrangement of strain gauges

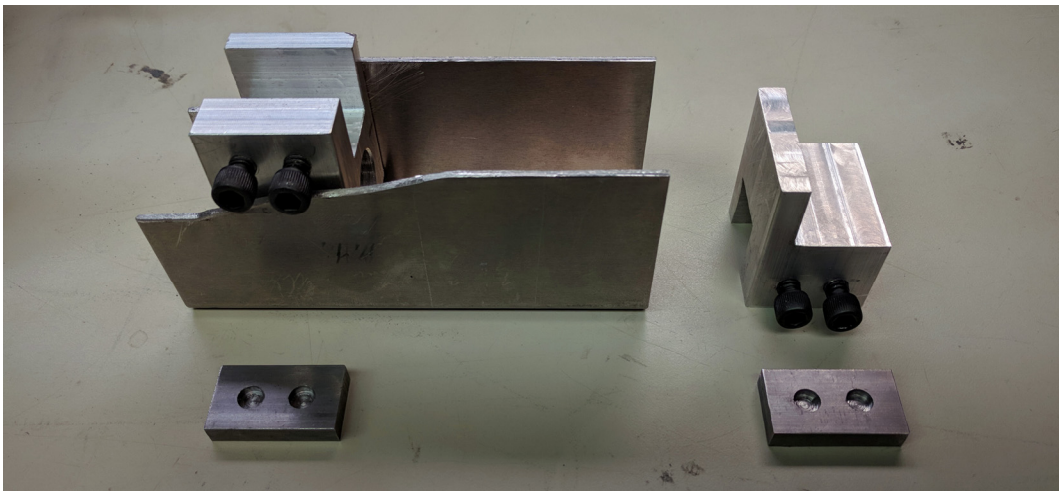

Figure 5.14: Linear variable differential transformer (LVDT) mounting hardware

### 5.2.2 Optical Measurement

A speckle pattern was applied to one side of each specimen as shown in Figure 5.15. Three coats of matte white spray paint were used for the base coast, and matte black spray paint was used to create the speckles. Each test was recorded with a high-speed camera as shown in Figure 5.16, and digital image correlation (DIC) software was used in post-processing to track the movement of the speckles. These data were used to generate time-varying strain and displacement fields for each test. The results from the DIC software were primarily used for a separate DIC research project at the University of Waterloo. However, some of the results are briefly discussed in Chapter 7.

## 5.3 Experimental Setup

All of the laboratory tests were carried out using a Shore Western hydraulic test frame as shown in Figure 5.17. The maximum static capacity of the frame is 1,200 kN and the maximum cyclic capacity is 1,000 kN. The specimens and shim plates were clamped together between the grips of the frame as shown in Figure 5.18. Care was taken to ensure that the specimens were centered between the grips, and that the specimens were plumb. Photographs of a typical experimental setup are shown in Figure 5.19. The static tests were performed in displacement control with a ramp rate of 0.5 mm/minute. The only exception to this was the pilot test, which was performed with a ramp rate of 0.18 mm/minute. The first cyclic test (Test No. 16) was performed with a cyclic loading rate of 1 Hz. The two subsequent cyclic tests were performed with a rate of 2 Hz.

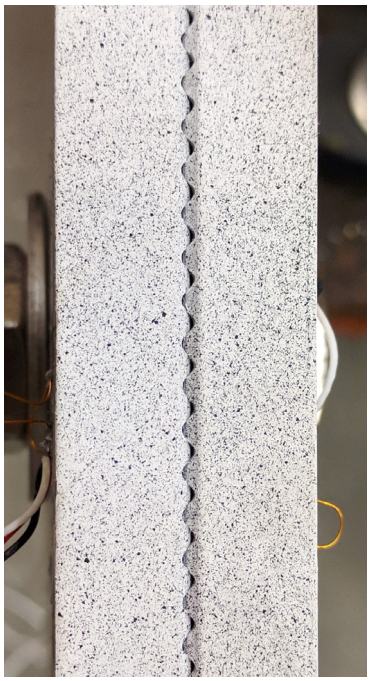

Figure 5.15: Typical speckle pattern used for digital image correlation (DIC)

Figure 5.16: High-speed camera used for digital image correlation (DIC)

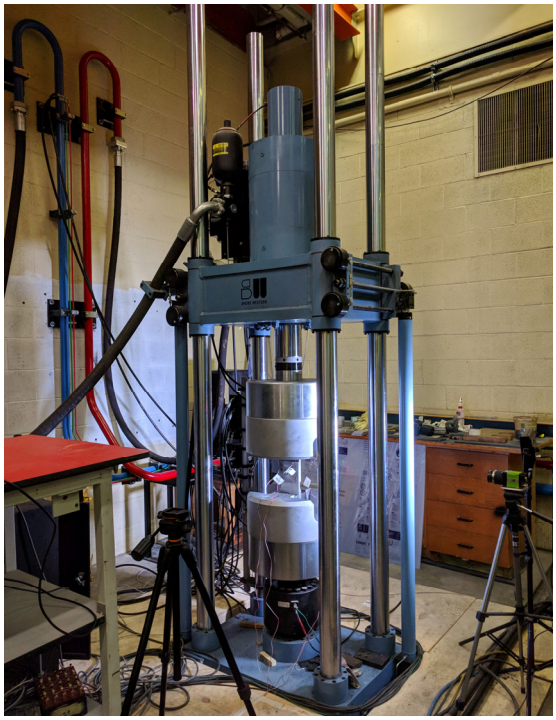

Figure 5.17: Hydraulic frame used for experimental program

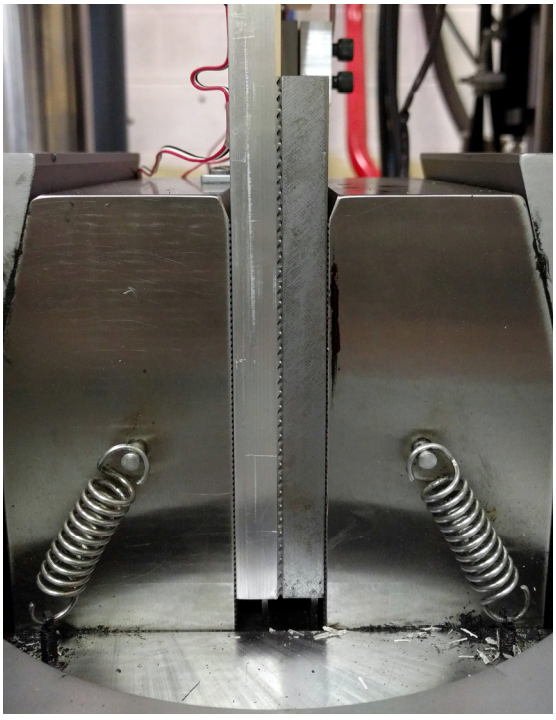

Figure 5.18: Specimen and shim plate clamped together by frame grip

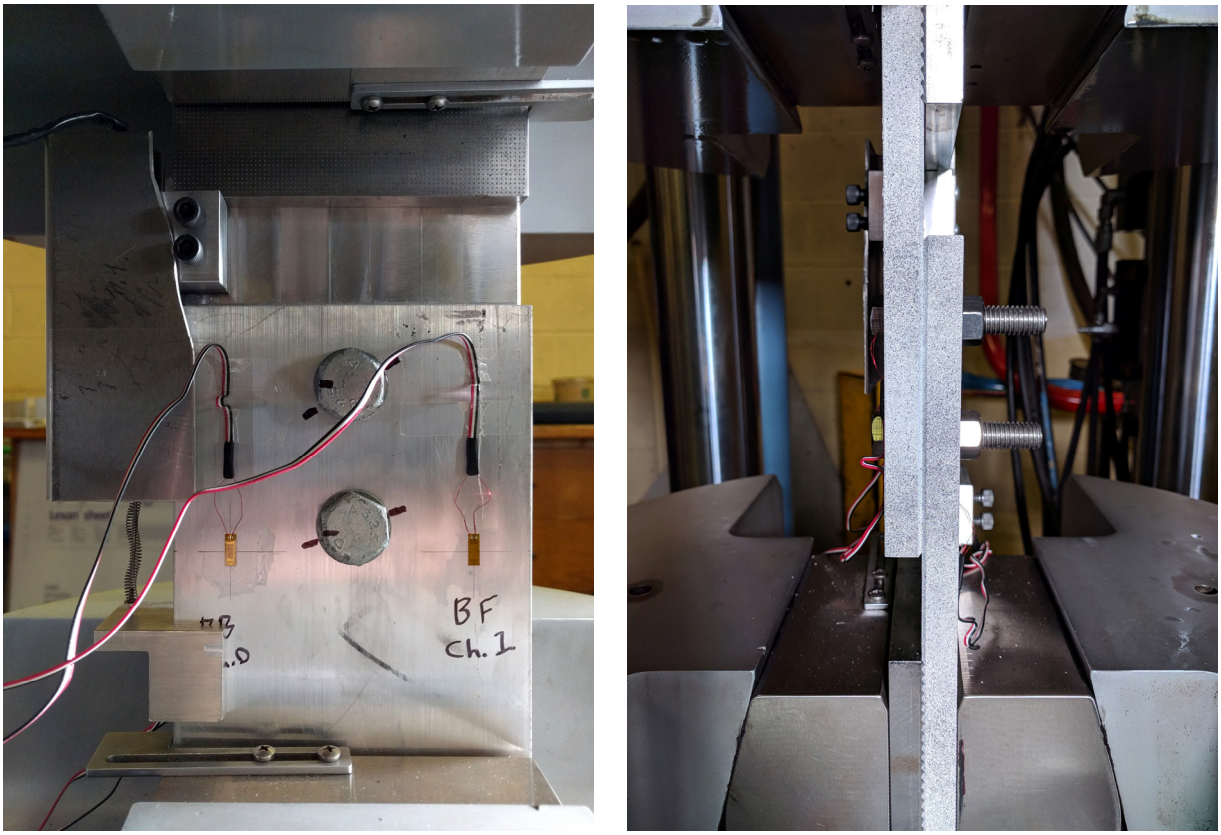


(a) Side View (b) Front View

Figure 5.19: Typical experimental setup

# 6 Results

This chapter presents the results of the experimental program. The observed behaviour of the specimens is discussed, and overall trends are described.

## 6.1 Static Testing

Load-displacement curves were generated for each static test specimen using the displacement measurements from the LVDT and the load measurements from the load cell of the test frame. The load-displacement curves for each individual test are provided in the appendix, along with the analytical results, which are discussed in Chapter 7. The failure loads observed during testing ranged from approximately 98.1 kN to 269.6 kN, and displacements at failure ranged from approximately 5.8 mm to 39.2 mm. All of the specimens failed by shearing of the bolts, with the exception of Specimens FSBS1-S (flat, sand-blasted, one blind bolt w/ sleeve) and RMBS1-S (ridged, not sand-blasted, one blind bolt w/ sleeve), which used ONESIDE$^{TM}$ blind bolts with shear sleeves. Typical bolt shear failures are shown in Figure 6.1. The bolts shown in the figure were re-assembled after failure to compare the shear deformation experienced by each bolt type. The shear sleeves increased the shear resistance of the ONESIDE$^{TM}$ bolts so greatly that the aluminum plates failed before the bolts reached their ultimate capacity. Specimen FSBB1-S (flat, sand-blasted, one blind bolt w/o sleeve) failed by block shear as shown in Figure 6.2, and Specimen RMBS1-S (ridged, not sand-blasted, one blind bolt w/ sleeve), which consisted of aluminum plates with a reduced cross-section due to the presence of ridges, failed by net section rupture as shown in Figure 6.3. The code-predicted failure loads corresponding to the observed failure modes are shown on the load-displacement curves for each specimen in the appendix. The code-predicted values were calculated using CSA S6 (2014) both with and without the specified resistance factors. The observed failure loads exceeded the code-predicted values for all of the specimens, with the exception of Specimen RMBS1-S (ridged, not sand-blasted, one blind bolt w/ sleeve), which used a ONESIDE$^{TM}$ blind bolt with a shear sleeve and failed by net section rupture at approximately 78% of the net section resistance predicted by CSA S6.

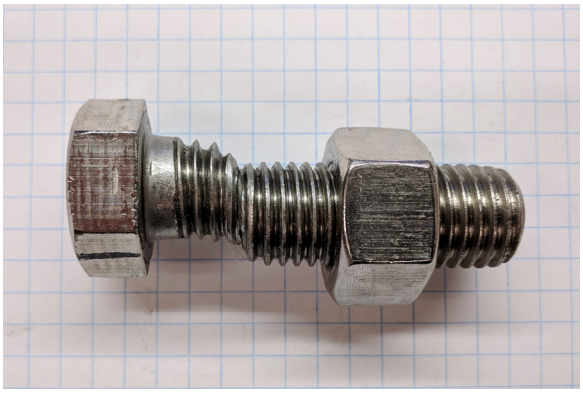

(a) ¾” stainless steel bolt

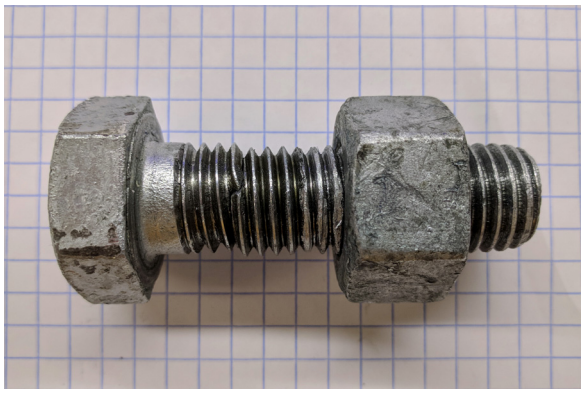

(b) ¾” carbon steel bolt

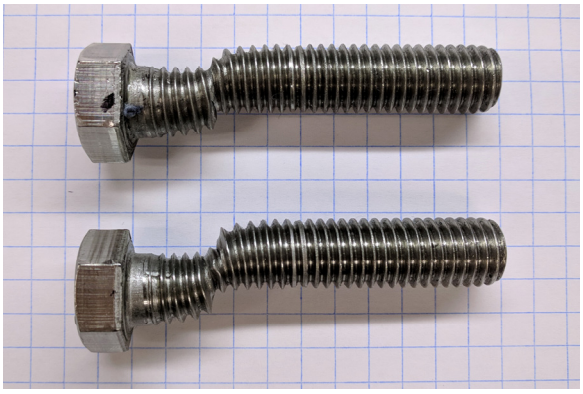

(c) ½” stainless steel bolts

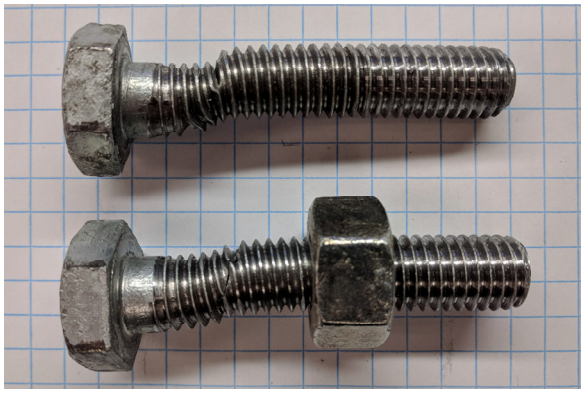

(d) ½” carbon steel bolts

Figure 6.1: Typical bolt shear failures

Figure 6.2: Block shear failure of Specimen FSBS1-S

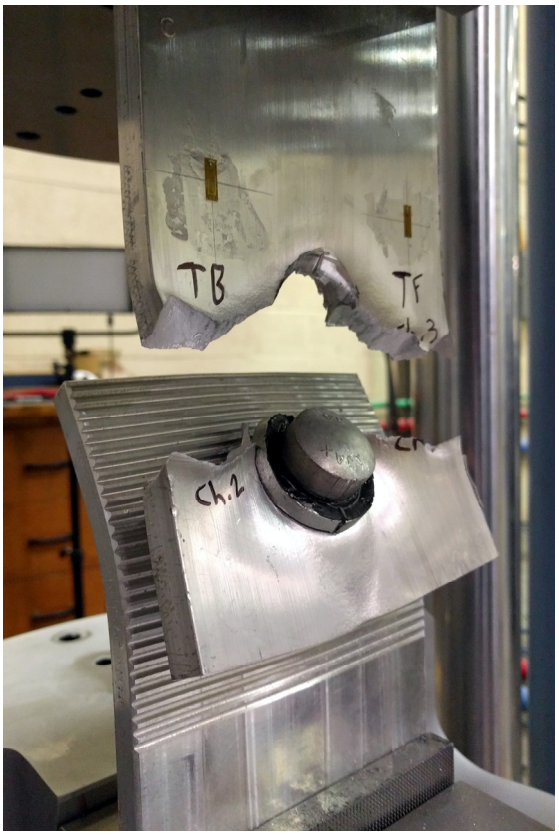


Figure 6.3: Net section failure of Specimen RMBS1-S

### 6.1.1 Non-Ridged Specimen Behaviour

Similar load-displacement behaviour was observed for each of the non-ridged specimens as shown in Figures 6.4 and 6.5. The behaviour was generally characterized by a steep linear initial slope, followed by a sudden decrease in load and plateau as the applied load reached the frictional resistance of the faying surfaces and the aluminum plates began to slip. Only a portion of the faying surface area contributed to the frictional resistance, as shown in Figure 6.6 where a polished zone is visible around the bolt holes where the clamping force was greatest. Following the plateau, the load then began to increase again as the bolts were engaged in shear. Localized yielding was observed on the inner surface of the bolt holes where the bolts bore against the aluminum plates as shown in Figure 6.7. A crest was formed as the applied load approached the ultimate capacity of the connection, followed by a rapid decrease in load and failure of the specimen. The length of

the flat plateau was seen to vary in each of the tests, which can be partially attributed to how well the bolts were centered within the bolt holes during assembly.

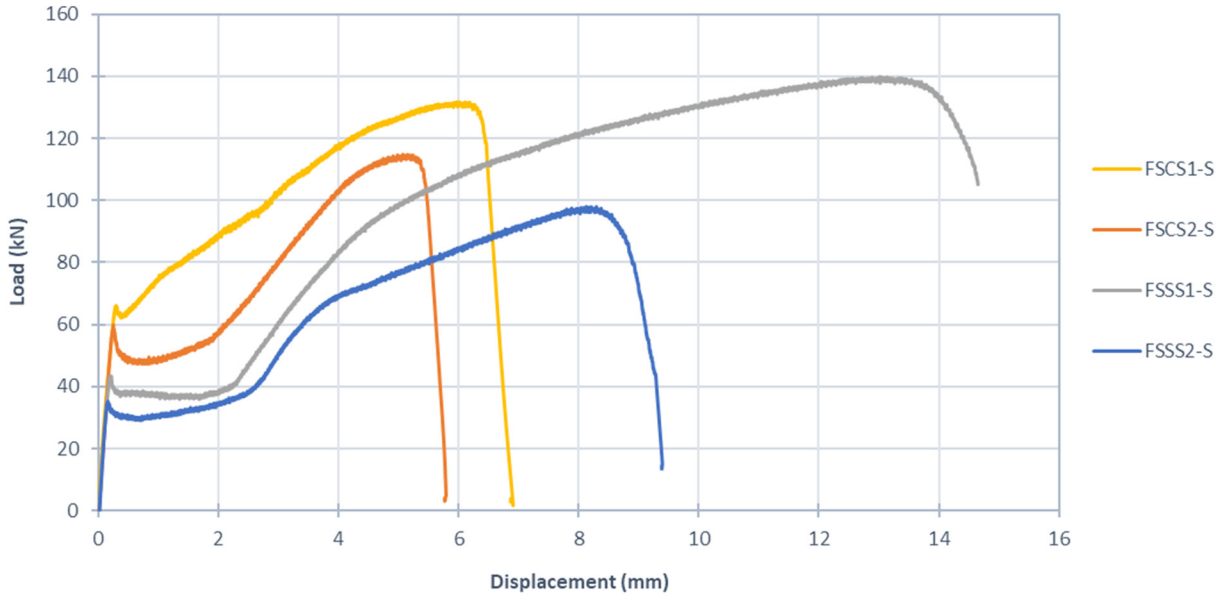


Figure 6.4: Load-displacement curves for non-ridged specimens with F593 or A325 bolts

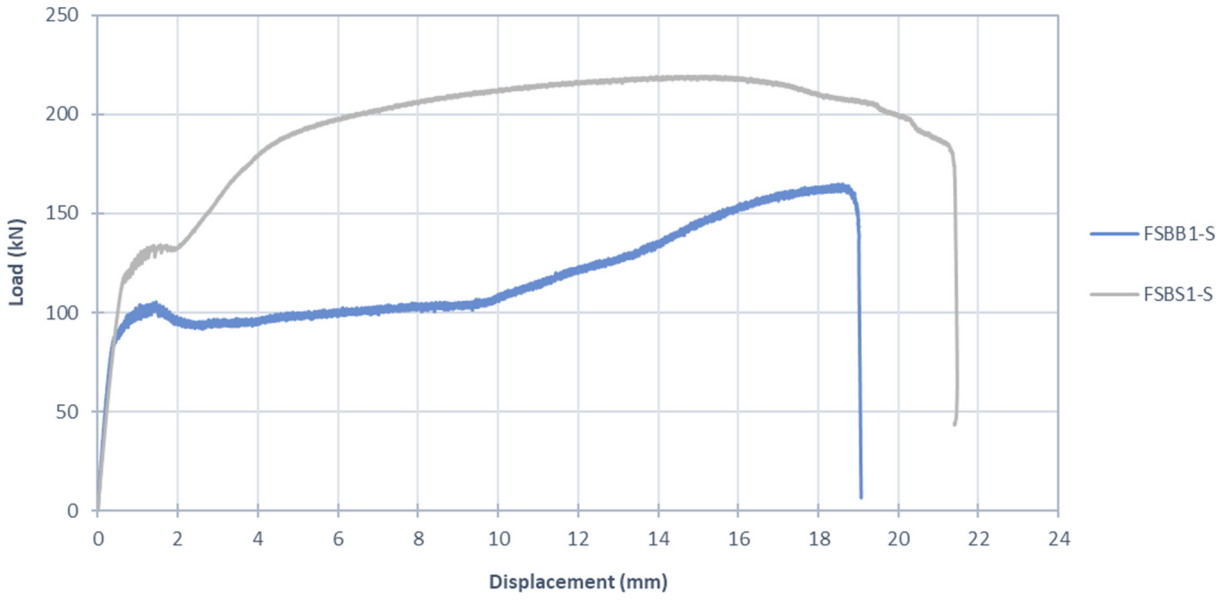


Figure 6.5: Load-displacement curves for non-ridged specimens with ONESIDE$^{TM}$ blind bolts

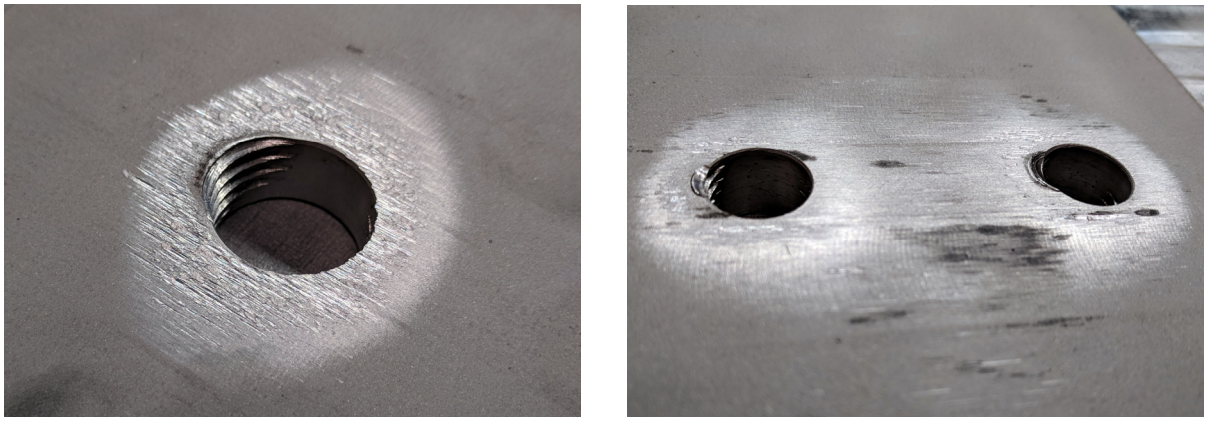

(a) Single bolt (b) Two bolts

Figure 6.6: Polished zone of flat faying surfaces due to slippage

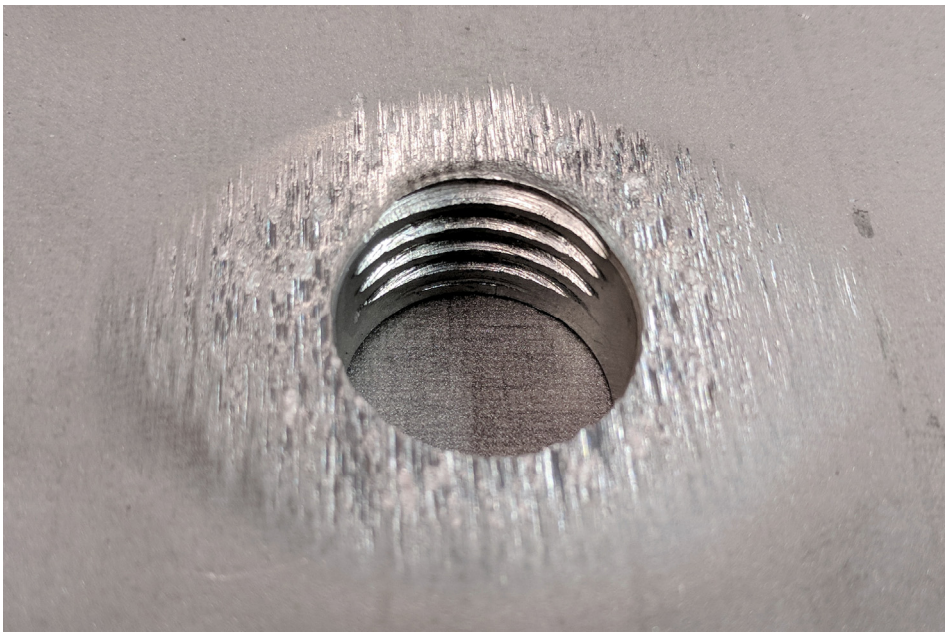

Figure 6.7: Localized yielding on inner surface of bolt hole due to bolt bearing

The short plateau observed for Specimen FSBS1-S (flat, sand-blasted, one blind bolt w/ sleeve) was a result of the shear sleeve that was used to fill the empty space between the bolt and the inner surface of the bolt hole. The stepped washers, which were used with the ONESIDE$^{TM}$ blind bolts, also helped to resist slip between the aluminum plates, as they bore on the inside surface of the bolt holes. This resulted in localized yielding around the edge of the bolt holes, however, as shown

in Figure 6.8. It is believed that the stepped washers contributed to the high slip loads that were observed for the specimens with ONESIDE$^{TM}$ bolts in comparison to those with standard stainless steel and carbon steel bolts. The two specimens that used ONESIDE$^{TM}$ blind bolts were observed to be much more ductile than the other non- ridged specimens, which can be attributed to the ability of the blind bolts to undergo greater rotation when used in eccentric connections. The blind bolts were able to rotate more than the standard stainless steel and carbon steel bolts due to a combination of three factors: The use of oversized bolt holes, the localized yielding around the bolt holes caused by the stepped washers, and the ability of the folded stepped washer to separate into two pieces as shown in Figure 6.9.

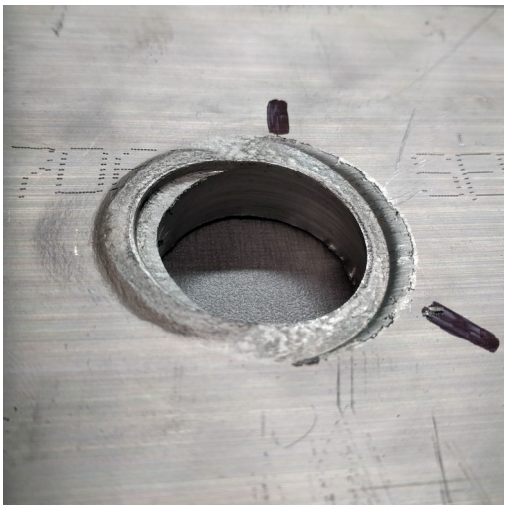

Figure 6.8: Localized yielding around bolt hole caused by stepped washer

Figure 6.9: Separation of folded stepped washer

As seen in Figure 6.4, the non-ridged specimens with stainless steel bolts exhibited more ductility than those with carbon steel bolts. This can be attributed to the higher ductility of stainless steel and the ability of the stainless steel bolts to undergo greater shear deformation before failure. In Figure 6.1, a greater difference in shear deformation between stainless steel and carbon steel can be seen for the ¾" bolts than for the ½" bolts. This supports the observed load-displacement curves shown in Figure 6.4, where Specimen FSSS1-S (flat, sand-blasted, one stainless steel bolt) failed at a displacement that was approximately 2.1 times greater than that of Specimen FSCS1-S (flat, sand-blasted, one carbon steel bolt), and Specimen FSSS2-S (flat, sand-blasted, two stainless steel bolts) failed at a displacement that was approximately 1.6 times greater than that of Specimen

FSCS2-S (flat, sand-blasted, two carbon steel bolts). In addition, each specimen with a single ¾" bolt exhibited more ductility than the corresponding specimen with two ½" bolts of the same material type. Specimen FSSS1-S (flat, sand-blasted, one stainless steel bolt), which consisted of a single ¾" stainless steel bolt, had both the greatest ductility and load-carrying capacity of all the non-ridged specimens, excluding those with ONESIDE$^{TM}$ blind bolts. Specimen FSCS2-S (flat, sand-blasted, two carbon steel bolts), which consisted of two ½" carbon steel bolts, had the lowest ductility, although it did not have the lowest load-carrying capacity. Specimens FSBS1-S (flat, sand-blasted, one blind bolt w/ sleeve) and FSBB1-S (flat, sand-blasted, one blind bolt w/o sleeve), which consisted of ONESIDE$^{TM}$ blind bolts, outperformed all of the other non-ridged specimens in terms of ductility, slip load, and maximum load-carrying capacity. It is also highly likely that Specimen FSBS1-S (flat, sand-blasted, one blind bolt w/ sleeve) could have carried more load if premature failure had not occurred due to block shear, although this may have also resulted in a reduction in ductility. The slip loads, peak loads, and displacements at failure for all of the non-ridged specimens are summarized in Table 6.1.

Table 6.1: Summary of slip loads, peak loads, and failure displacements for non-ridged specimens

| Specimen | Slip Load (kN) | Peak Load (kN) | Displacement at Failure (mm) | Failure Mode |
|---|---|---|---|---|
| FSCS1-S | 64.8 | 131.7 | 6.9 | Bolt Shear |
| FSCS2-S | 59.9 | 114.9 | 5.8 | Bolt Shear |
| FSSS1-S | 43.4 | 139.9 | 14.7 | Bolt Shear |
| FSSS2-S | 35.3 | 98.1 | 9.4 | Bolt Shear |
| FSBS1-S | 134.2 | 219.4 | 21.5 | Plate Block Shear |
| FSBB1-S | 105.4 | 164.9 | 19.1 | Bolt Shear |

### 6.1.2 Ridged Specimen Behaviour

The load-displacement behavior of the ridged specimens varied more widely than the non-ridged specimens as shown in Figures 6.10, 6.11, and 6.12. However, the behaviour was generally characterized by a linear initial slope, followed by the formation of a crest as the applied load approached the first slip load. During this time, the interlocking ridges were observed to gradually

disengage. At the point when the first slip load was reached, the ridges were seen to be fully disengaged and all of the shear force was being carried by the bolt(s). The load then decreased to a local minimum as the ridges slipped over one another and re-engaged in a new position. This ridge slip process repeated itself between one and five times during each of the tests before failure occurred. If the magnitude of the first slip load exceeded the shear capacity of the bolt(s), then the magnitude of the subsequent slip load(s) did not surpass the first. However, if the magnitude of the first slip load did not exceed the shear capacity of the bolt(s), then the magnitude of the subsequent slip load(s) increased until the shear capacity of the bolt(s) was exceeded. The only exception to this was Specimen RMBS1-S (ridged, not sand-blasted, one blind bolt w/ sleeve), which failed prematurely by net section rupture as previously discussed. Like the non-ridged specimens, only a portion of the faying surface area contributed to the frictional resistance, as shown in Figure 6.13 where a polished zone and ridge damage is visible around the bolt holes where the clamping force was greatest. Localized yielding was also observed on the inner surface of the bolt holes, which is consistent with the observations for the non-ridged specimens.

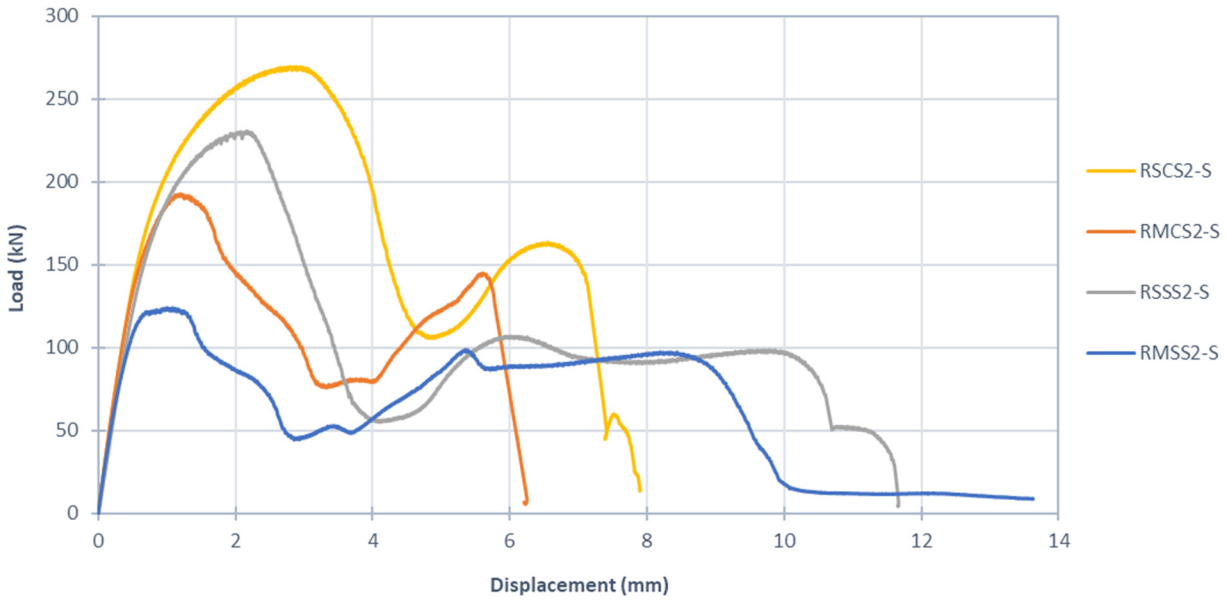


Figure 6.10: Load-displacement curves for ridged two-bolt specimens with F593 or A325 bolts

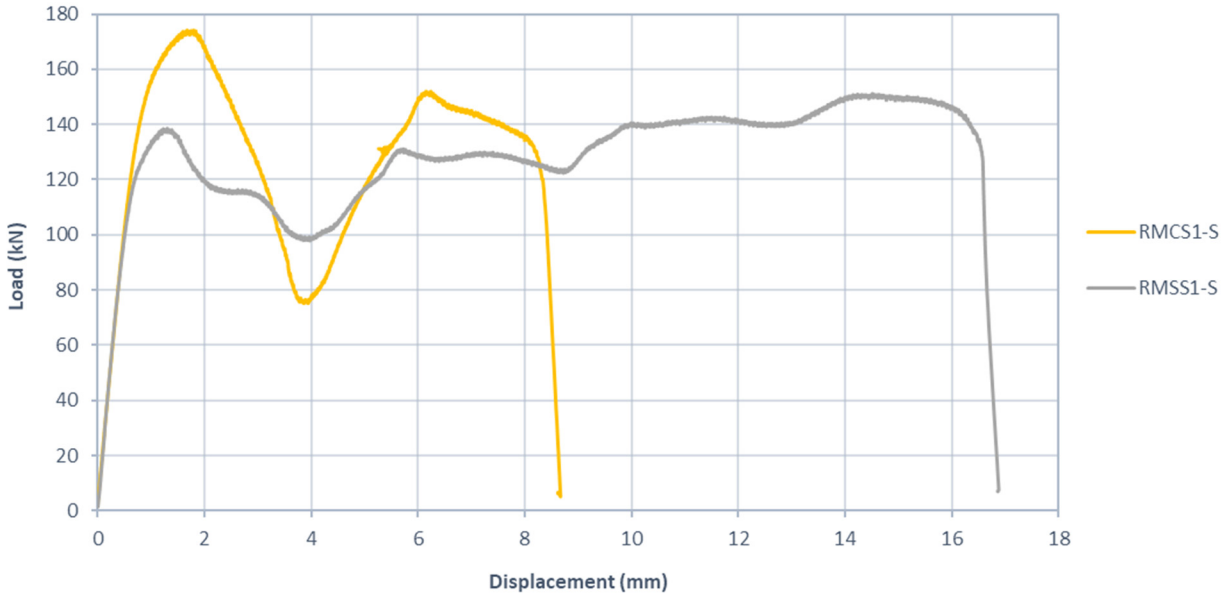


Figure 6.11: Load-displacement curves for ridged single-bolt specimens with F593 or A325 bolts

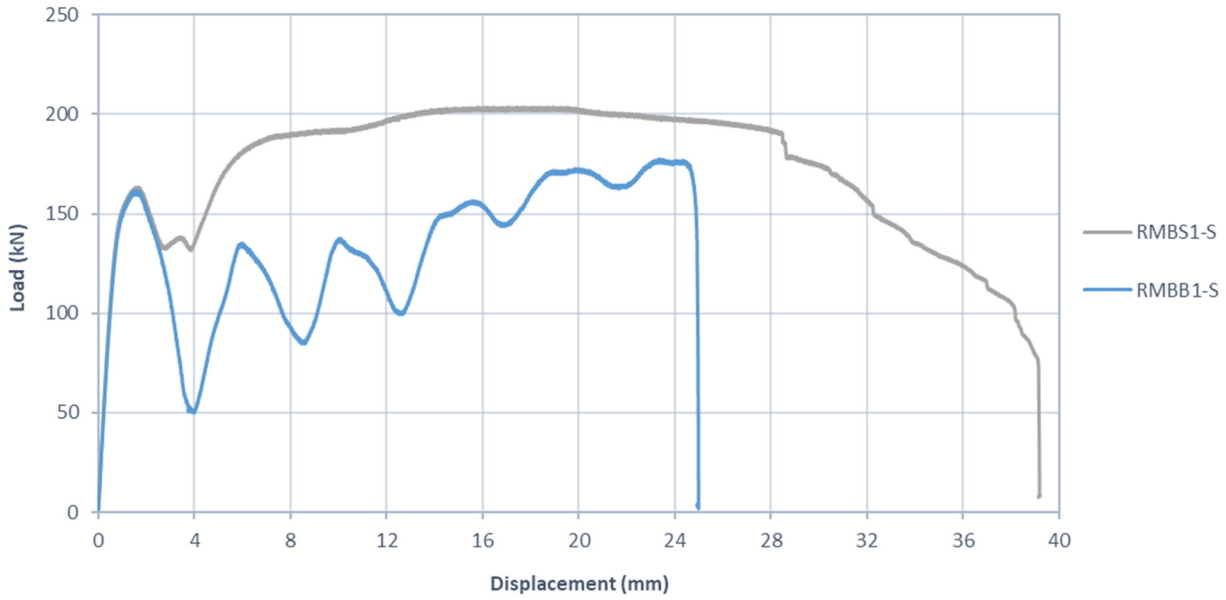


Figure 6.12: Load-displacement curves for ridged specimens with ONESIDE$^{TM}$ blind bolts

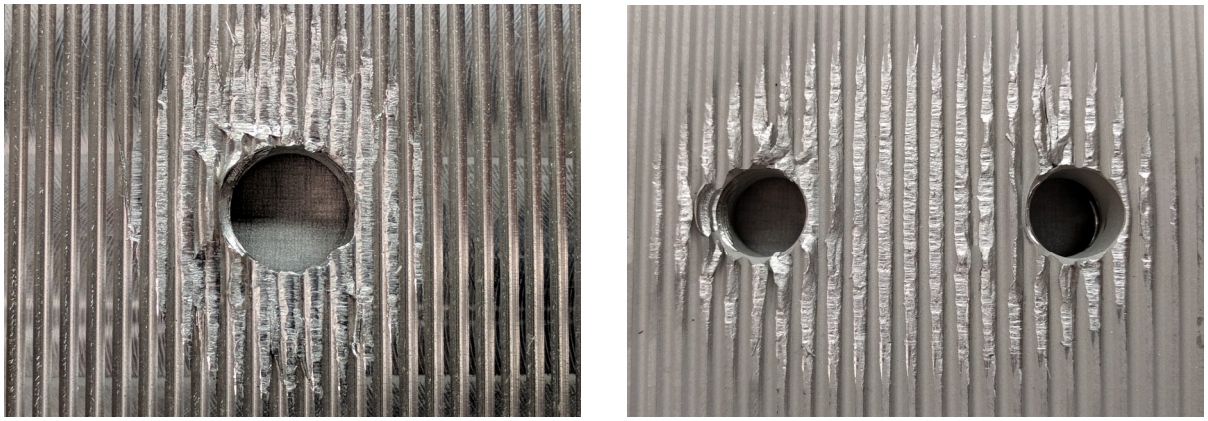

(a) Single bolt (b) Two bolts

Figure 6.13: Polished zone and ridge damage of ridged faying surfaces due to slippage

As seen in Figure 6.12, the two specimens that used ONESIDE$^{TM}$ blind bolts exhibited much more ductility than the other ridged specimens. The reasons for this are the same as those previously described for the non-ridged specimens with ONESIDE$^{TM}$ blind bolts. Specimen RMBB1-S (ridged, not sand-blasted, one blind bolt w/o sleeve) did not use a shear sleeve with the blind bolt, and so ridge slippage occurred more readily than for Specimen RMBS1-S (ridged, not sand-blasted, one blind bolt w/ sleeve). In Figure 6.12, the oscillatory behaviour of the load-displacement curve for Specimen RMBB1-S (ridged, not sand-blasted, one blind bolt w/o sleeve) shows that the interlocking ridges slipped six times during loading before failure. In contrast, the ridges of Specimen RMBS1-S (ridged, not sand-blasted, one blind bolt w/ sleeve), which did use a shear sleeve, only slipped once before the onset of net section yielding.

As seen in Figures 6.10 and 6.11, the ridged specimens with stainless steel bolts exhibited more ductility than those with carbon steel bolts, and a greater increase in ductility was observed for the single ¾” bolts than for the double ½” bolts. These results are in line with the observations previously made for the non-ridged specimens. Greater ductility was also observed for the two-bolt specimens with sand-blasted faying surfaces than for the two-bolt specimens with non-sand-blasted faying surfaces and the same bolt material type. In addition, the use of sand-blasted faying surfaces increased the load-carrying capacity of the two-bolt specimens by approximately 40% and 87% for the specimens with carbon steel bolts and stainless steel bolts, respectively, in comparison to the as-machined specimens. Specimen RSCS2-S (ridged, sand-blasted, two carbon

steel bolts) had the greatest load-carrying capacity of all the ridged specimens, however it was also one of the least ductile. Specimen RSSS2-S (ridged, sand-blasted, two stainless steel bolts) had the second-greatest load-carrying capacity, and it exhibited much more ductility than Specimen RSCS2-S (ridged, sand-blasted, two carbon steel bolts) with a 48% greater displacement at failure. In general, the specimens with carbon steel bolts were able to carry more load than those with stainless steel bolts when faying surface finish and bolt count remained constant. The load-carrying capacities of the single-bolt specimens with stainless steel and carbon steel bolts were comparable to those of the respective two-bolt specimens with the same bolt material type. However, the single-bolt specimens exhibited more ductility than the two-bolt specimens. The load-carrying capacity of Specimen RMBB1-S (ridged, not sand-blasted, one blind bolt w/o sleeve), which used a ONESIDE$^{TM}$ blind bolt without a shear sleeve, was comparable to that of Specimen RMCS1-S (ridged, not sand-blasted, one carbon steel bolt), however the displacement at failure was nearly three times greater. Specimen RMBS1-S (ridged, not sand-blasted, one blind bolt w/ sleeve) was able to carry more load than Specimen RMBB1-S (ridged, not sand-blasted, one blind bolt w/o sleeve) and had greater ductility, however it also failed prematurely due to net section rupture. It is likely that Specimen RMBS1-S (ridged, not sand-blasted, one blind bolt w/ sleeve) could have carried more load if net section rupture had not occurred, however this may have also resulted in reduced ductility. The slip loads, peak loads, and displacements at failure for all of the ridged specimens are summarized in Table 6.2.

Table 6.2: Summary of slip loads, peak loads, and failure displacements for ridged specimens

| Specimen | Slip Load (kN) | Peak Load (kN) | Displacement at Failure (mm) | Failure Mode |
|---|---|---|---|---|
| RSCS2-S | 269.6 | 269.6 | 7.9 | Bolt Shear |
| RMCS2-S | 192.7 | 192.7 | 6.3 | Bolt Shear |
| RSSS2-S | 230.8 | 230.8 | 11.7 | Bolt Shear |
| RMSS2-S | 124.0 | 124.0 | 10.1 | Bolt Shear |
| RMCS1-S | 174.2 | 174.2 | 8.7 | Bolt Shear |
| RMSS1-S | 137.0 | 151.2 | 16.9 | Bolt Shear |
| RMBS1-S | 163.5 | 203.8 | 39.2 | Plate Rupture |
| RMBB1-S | 161.6 | 177.6 | 25.0 | Bolt Shear |

### 6.1.3 Comparison of Ridged and Non-Ridged Specimen Behaviour

The load-displacement behaviour of the ridged and non-ridged specimens with two ½" carbon steel bolts are compared in Figure 6.14. It can be seen that the two ridged specimens outperformed the non-ridged specimen in terms of both strength and ductility. Specimen FSCS2-S (flat, sand-blasted, two carbon steel bolts) had sand-blasted faying surfaces and was still outperformed by Specimen RMCS2-S (ridged, not sand-blasted, two carbon steel bolts), which did not have sand-blasted faying surfaces. Specimens RMCS2-S (ridged, not sand-blasted, two carbon steel bolts) and RSCS2-S (ridged, sand-blasted, two carbon steel bolts) exceeded that ultimate load-carrying capacity of Specimen FSCS2-S (flat, sand-blasted, two carbon steel bolts) by factors of approximately 1.7 and 2.3, respectively. The ultimate capacities of Specimens RMCS2-S (ridged, not sand-blasted, two carbon steel bolts) and RSCS2-S (ridged, sand-blasted, two carbon steel bolts) also defined the slip loads of these two specimens, which exceeded the slip load of Specimen FSCS2-S (flat, sand-blasted, two carbon steel bolts) by factors of approximately 3.2 and 4.5, respectively.

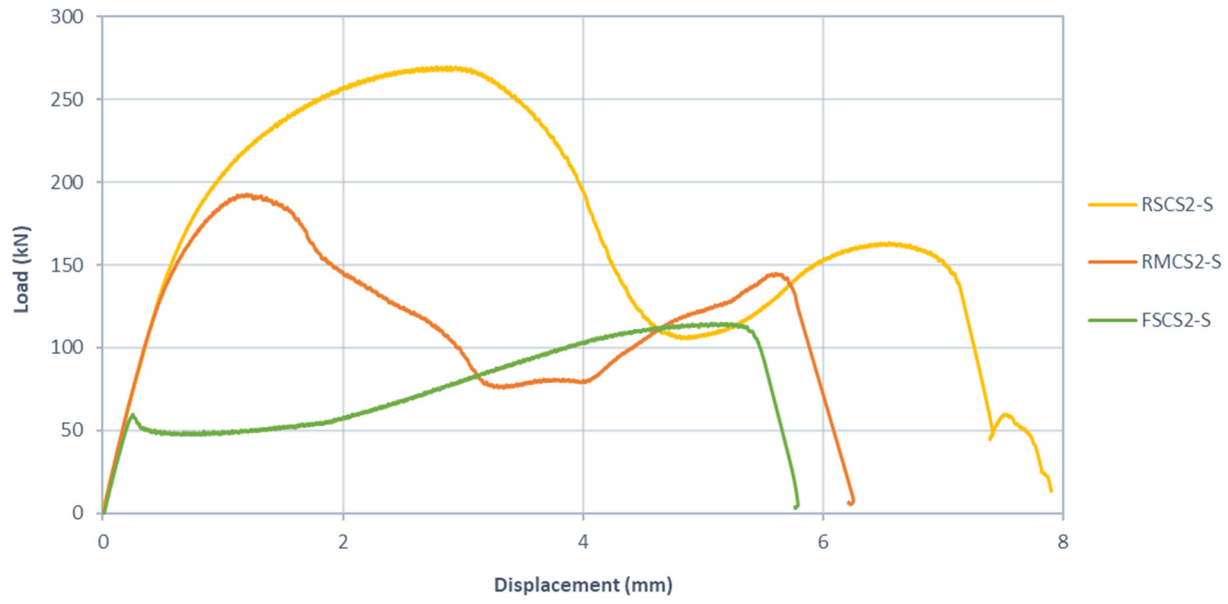


Figure 6.14: Load-displacement curves for specimens with ½" carbon steel bolts

The load-displacement behaviour of the ridged and non-ridged specimens with two ½" stainless steel bolts are compared in Figure 6.15. Like the specimens with carbon steel bolts, the ridged specimens again outperformed the non-ridged specimen in terms of strength and ductility. However, the gain in ultimate load-carrying capacity between the non-sand-blasted ridged specimen and the sand-blasted non-ridged specimen was far less than that observed with the carbon steel bolts. The load-carrying capacities of Specimens RMSS2-S (ridged, not sand-blasted, two stainless steel bolts) and RSSS2-S (ridged, sand-blasted, two stainless steel bolts) exceeded that of Specimen FSSS2-S (flat, sand-blasted, two stainless steel bolts) by factors of approximately 1.3 and 2.4, respectively. Like the specimens with carbon steel bolts, the ultimate capacities of Specimens RMSS2-S (ridged, not sand-blasted, two stainless steel bolts) and RSSS2-S (ridged, sand-blasted, two stainless steel bolts) again defined the slip loads of these two specimens, which exceeded the slip load of Specimen FSSS2-S (flat, sand-blasted, two stainless steel bolts) by factors of approximately 3.5 and 6.5, respectively. The increase in slip load between Specimens RSSS2-S (ridged, sand-blasted, 2 stainless steel bolts) and FSSS2-S (flat, sand-blasted, 2 stainless steel bolts) was about 44% greater than that between specimens RSCS2-S (ridged, sand-blasted, 2 carbon steel bolts) and FSCS2-S (flat, sand-blasted, 2 carbon steel bolts). In contrast, the increase in slip load between Specimens RMSS2-S (ridged, not sand-blasted, 2 stainless steel bolts) and FSSS2-S (flat, sand-blasted, 2 stainless steel bolts) was only about 9% greater than that between Specimens RMCS2-S (ridged, not sand-blasted, 2 carbon steel bolts) and FSCS2-S (flat, sand-blasted, 2 carbon steel bolts).

The load-displacement behaviour of the ridged and non-ridged specimens with single ¾" carbon steel bolts are compared in Figure 6.16. The load-carrying capacity of Specimen RMCS1-S (ridged, not sand-blasted, one carbon steel bolt) exceeded that of Specimen FSCS1-S (flat, sand-blasted, one carbon steel bolt) by a factor of approximately 1.3, and Specimen RMCS1-S (ridged, not sand-blasted, one carbon steel bolt) also exhibited greater ductility. The ultimate capacity of Specimen RMCS1-S (ridged, not sand-blasted, one carbon steel bolt) also defined the slip load of this specimen, which exceeded the slip load of specimen FSCS1-S (flat, sand-blasted, one carbon steel bolt) by a factor of approximately 2.7. This increase in slip load is about 16% less than that observed between Specimens RMCS2-S (ridged, not sand-blasted, two carbon steel bolts) and FSCS2-S (flat, sand-blasted, two carbon steel bolts), which had two carbon steel bolts each.

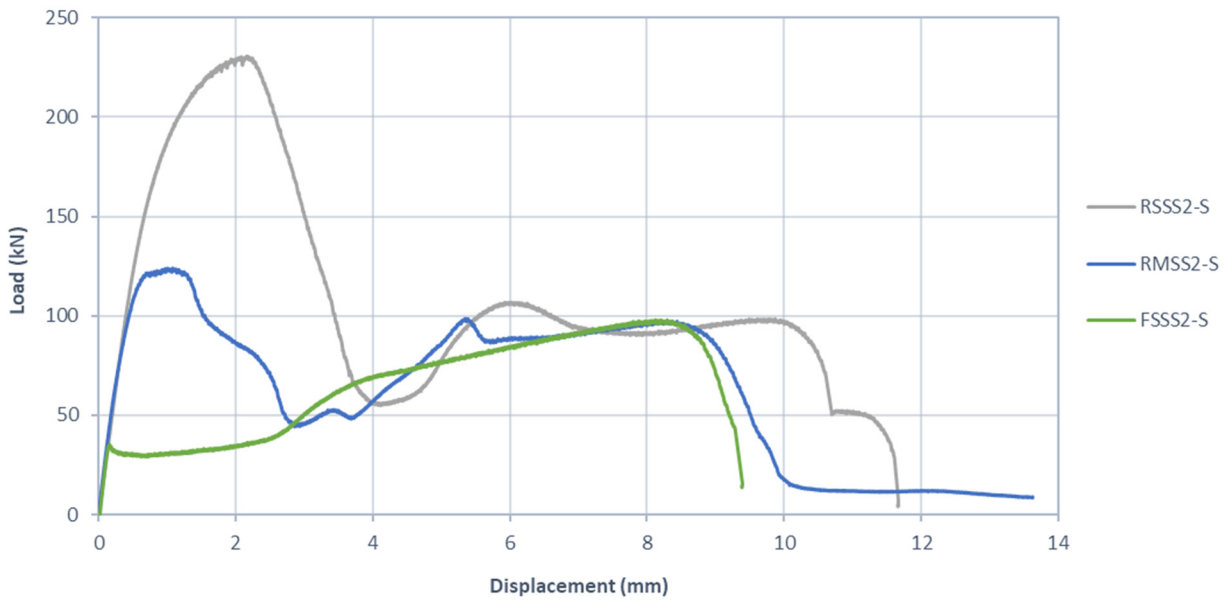


Figure 6.15: Load-displacement curves for specimens with ½" stainless steel bolts

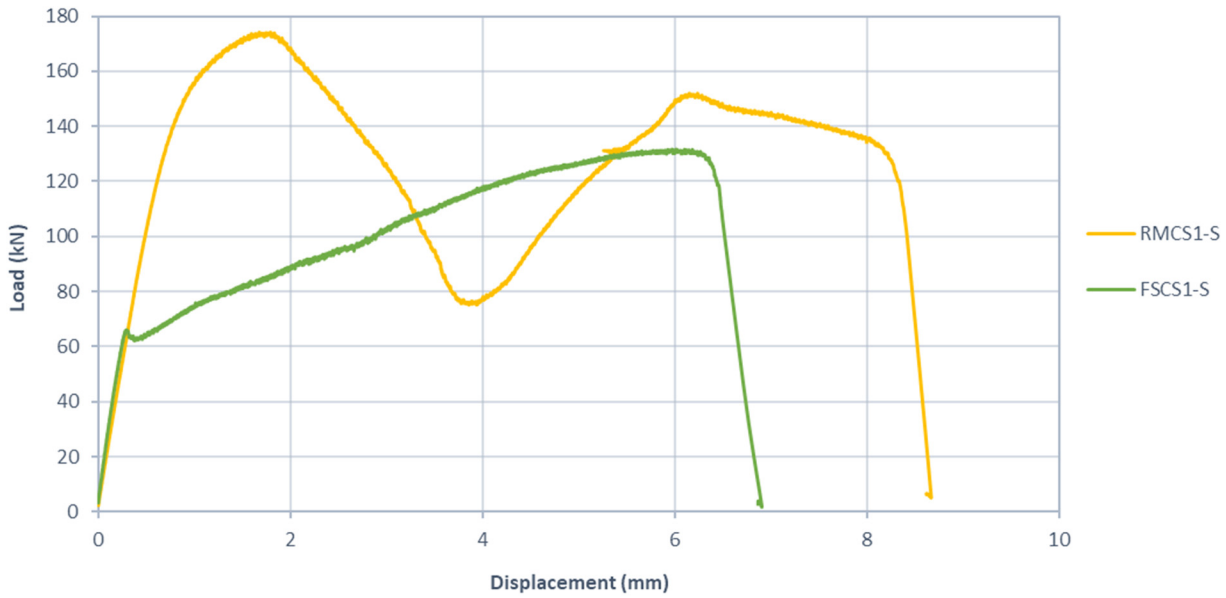


Figure 6.16: Load-displacement curves for specimens with ¾" carbon steel bolts

The load-displacement behaviour of the ridged and non-ridged specimens with single ¾" stainless steel bolts are compared in Figure 6.17. Like the specimens with single carbon steel bolts, the ridged specimen exhibited increased strength and ductility compared to the non-ridged specimen. However, the gain in strength was much less than that observed for the specimens with single

carbon steel bolts. The load-carrying capacity of Specimen RMSS1-S (ridged, not sand-blasted, one stainless steel bolt) exceeded that of Specimen FSSS1-S (flat, sand-blasted, one stainless steel bolt) by a factor of approximately 1.1. This increase in strength is about 15% less than that observed between Specimens RMCS1-S (ridged, not sand-blasted, one carbon steel bolt) and FSCS1-S (flat, sand-blasted, one carbon steel bolt). Unlike Specimen RMCS1-S (ridged, not sand-blasted, one carbon steel bolt), the ultimate capacity of Specimen RMSS1-S S (ridged, not sand-blasted, one stainless steel bolt) did not correspond with the slip load of this specimen. However, the slip load of specimen RMSS1-S S (ridged, not sand-blasted, one stainless steel bolt) still exceeded that of Specimen FSSS1-S (flat, sand-blasted, one stainless steel bolt) by a factor of approximately 3.2. This increase in slip load is about 9% less than that observed between Specimens RMSS2-S (ridged, not sand-blasted, two stainless steel bolts) and FSSS2-S (ridged, sand-blasted, two stainless steel bolts), which had two stainless steel bolts each.

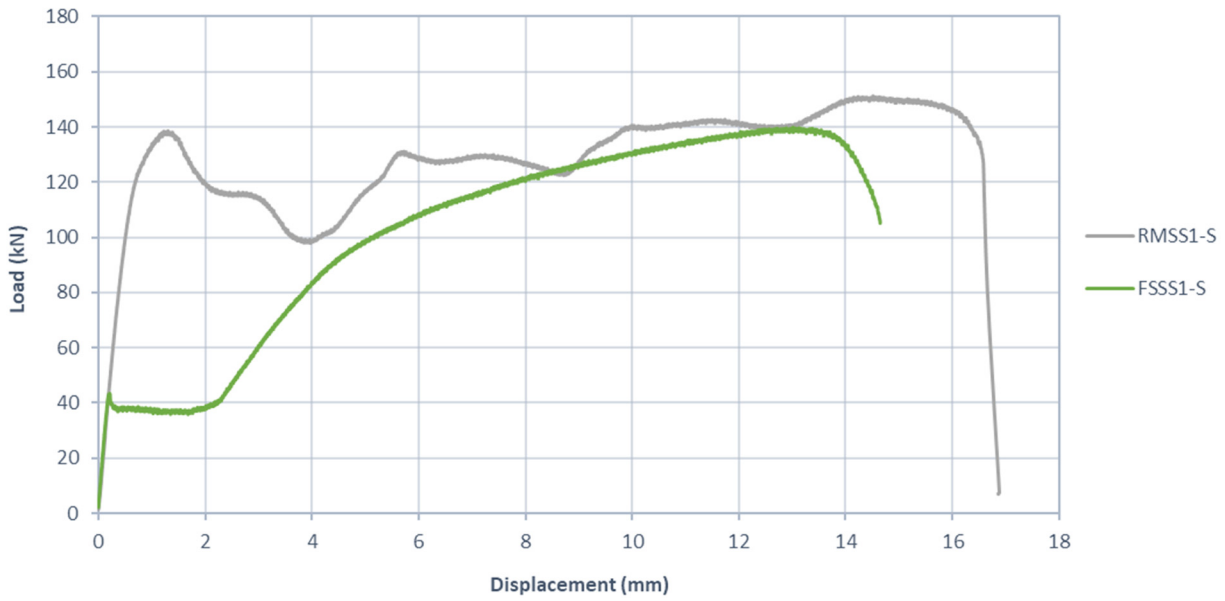


Figure 6.17: Load-displacement curves for specimens with ¾" stainless steel bolts

The load-displacement behaviour of the ridged and non-ridged specimens with single ¾" ONESIDE$^{TM}$ blind bolts are compared in Figure 6.18. The load-carrying capacity of Specimen RMBB1-S (ridged, not sand-blasted, one blind bolt w/o sleeve) exceeded that of Specimen FSBB1-S (flat, sand-blasted, one blind bolt w/o sleeve) by a factor of approximately 1.1, and Specimen RMBB1-S (ridged, not sand-blasted, one blind bolt w/o sleeve) also exhibited much

more ductility. However, the load-carrying capacity of Specimen RMBS1-S (ridged, not sand-blasted, one blind bolt w/ sleeve), which used a blind bolt shear sleeve, did not exceed that of Specimen FSBS1-S (flat, sand-blasted, one blind bolt w/ sleeve). This can be attributed to the fact that Specimen RMBS1-S (ridged, not sand-blasted, one blind bolt w/ sleeve) failed by net section rupture and specimen FSBS1-S (flat, sand-blasted, one blind bolt w/ sleeve) failed by block shear, whereas all of the other specimens failed by bolt shear. The aluminum plates of Specimen RMBS1-S (ridged, not sand-blasted, one blind bolt w/ sleeve) had a reduced cross-sectional area due to the presence of ridges on the faying surfaces, and thus had reduced capacity. All four specimens that utilized ONESIDE$^{TM}$ blind bolts had ultimate load-carrying capacities that exceeded their slip loads. The slip load of Specimen RMBB1-S (ridged, not sand-blasted, one blind bolt w/o sleeve) exceeded that of Specimen FSBB1-S (flat, sand-blasted, one blind bolt w/o sleeve) by a factor of approximately 1.5. This increase is about 44% less than that observed between Specimens RMCS1-S S (ridged, not sand-blasted, one carbon steel bolt) and FSCS1-S (flat, sand-blasted, one carbon steel bolt). The slip load of Specimen RMBS1-S (ridged, not sand-blasted, one blind bolt w/ sleeve) exceeded that of Specimen FSBS1-S (flat, sand-blasted, one blind bolt w/ sleeve) by a factor of approximately 1.2, which is an even smaller increase. The gains in slip load, peak load, and ductility are summarized in Table 6.3 for all of the ridged specimens.

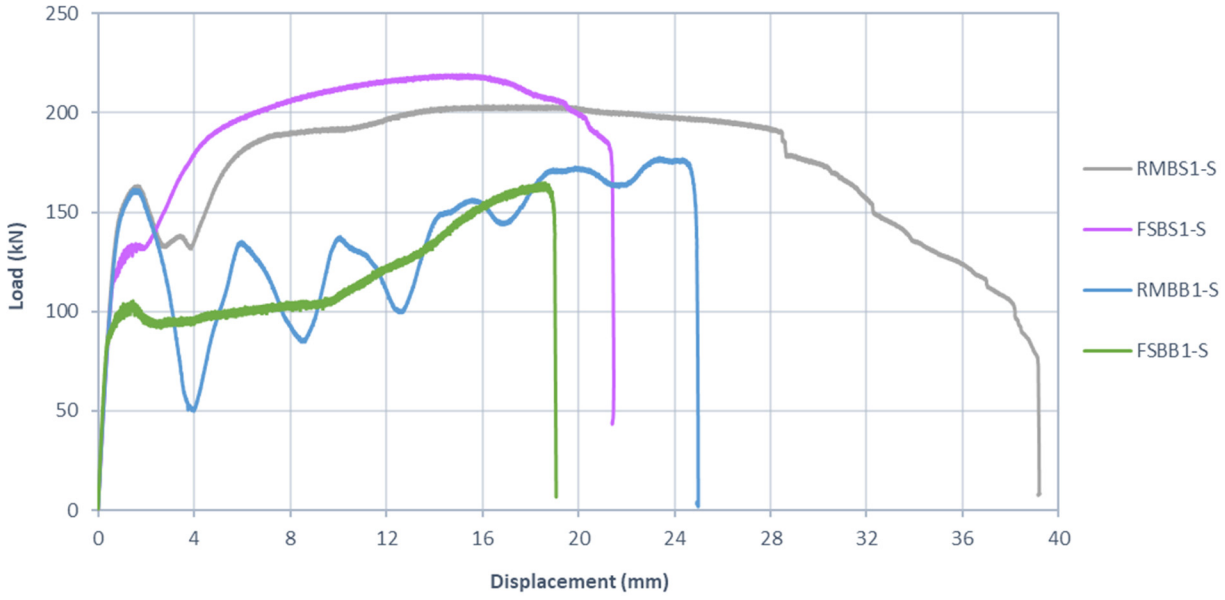


Figure 6.18: Load-displacement curves for specimens with ¾" ONESIDE$^{TM}$ blind bolts

Table 6.3: Summary of slip-load, peak load, and ductility gains for ridged specimens

| Ridged Specimen | Non-Ridged Specimen | Slip-Load Increase (%) | Peak Load Increase (%) | Ductility Increase (%) |
|---|---|---|---|---|
| RMCS1-S | FSCS1-S | 169 | 32 | 26 |
| RMCS2-S | FSCS2-S | 222 | 68 | 8.6 |
| RSCS2-S | FSCS2-S | 350 | 135 | 36 |
| RMSS1-S | FSSS1-S | 216 | 8.1 | 15 |
| RMSS2-S | FSSS2-S | 251 | 26 | 7.4 |
| RSSS2-S | FSSS2-S | 554 | 135 | 24 |
| RMBS1-S | FSBS1-S | 22 | -7.1 | 82 |
| RMBB1-S | FSBB1-S | 53 | 7.7 | 31 |

## 6.2 Fatigue Testing

The results from the three cyclic tests were used to generate S-N curves for Specimen RMSS1-C (ridged, not sand-blasted, one stainless steel bolt), as shown in Figure 6.19. Each cyclic test specimen consisted of ridged non-sand-blasted faying surfaces and a single ¾" stainless steel bolt. A different load amplitude was used for each test. However, a constant stress ratio ($R = S_{min} / S_{max}$) of 0.1 was maintained. The load ranges used for each of the tests are summarized in Table 6.4, along with the resulting fatigue lives. The nominal stress ranges shown in Figure 6.19 were calculated based on the geometry of the specimens and the applied loads. One S-N curve was generated using only nominal axial stress, while the other was generated using combined axial and bending stresses at the location of the ridge valleys. The combined axial and bending stress was calculated using Equation 6.1, which was derived from first principles for eccentrically-loaded lap-splice connections with interlocking ridges. The slopes, m, of the line segments shown in the figure are both approximately 3.4 in log-log scale.

Table 6.4: Summary of cyclic loading ranges and resulting fatigue lives

| Test No. | Load Midpoint (kN) | Load Amplitude (kN) | Load Range (kN) | No. of Cycles to Failure |
|---|---|---|---|---|
| 1 | 49.50 | 40.50 | 81.00 | 13,941 |
| 2 | 33.55 | 27.45 | 54.90 | 51,927 |
| 3 | 17.60 | 14.40 | 28.80 | 3,422,910 |

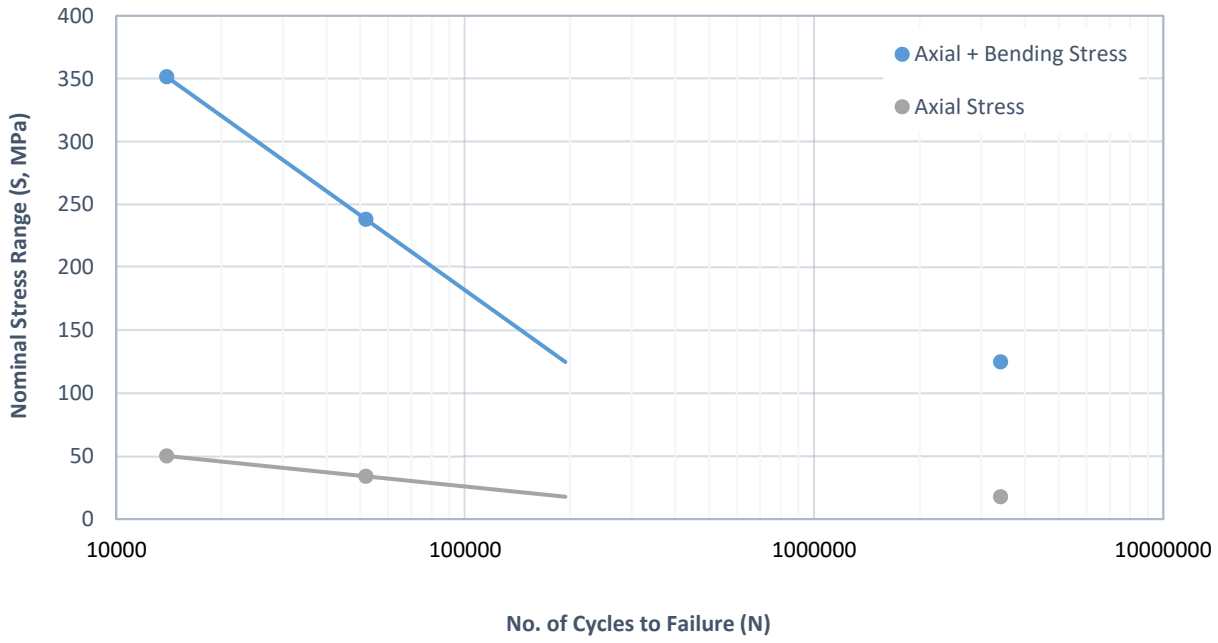


Figure 6.19: S-N results for Specimen RMSS1-C

$$S = \frac{7 \cdot P}{w \cdot (t-h)} \tag{6.1}$$

where:

$S$ = Combined axial and bending stress at ridge valley

$P$ = Applied tensile load

$w$ = Plate width

$t$ = Plate thickness

$h$ = Ridge depth

All three cyclic test specimens developed fatigue cracks, which initiated from two adjacent ridge valleys as shown in Figures 6.20 and 6.21. A polished region can also be seen around the bolt hole in the figure where the clamping force was greatest. The cracks initiated from the middle of each specimen at the ridges located closest to the edge of a washer. They propagated through the specimens until sudden failure occurred by rupture of the remaining cross-sectional area. As seen in Figure 6.19, the first two specimens failed at relatively low cycle counts. The third specimen was able to withstand a much higher cycle count, however the applied peak load was only about 21% of the ultimate capacity observed from the static test of an identical specimen, RMSS1-S (ridged, not sand-blasted, one stainless steel bolt). Based on the S-N results shown in Figure 6.19, it appears that it may be possible to represent the fatigue behaviour of Specimen RMSS1-C (ridged, not sand-blasted, one stainless steel bolt) with a bi-linear curve on a stress range vs. LOG(fatigue life) plot. However, further experimental testing would be required to create a more accurate and complete S-N curve for Specimen RMSS1-C (ridged, not sand-blasted, one stainless steel bolt).

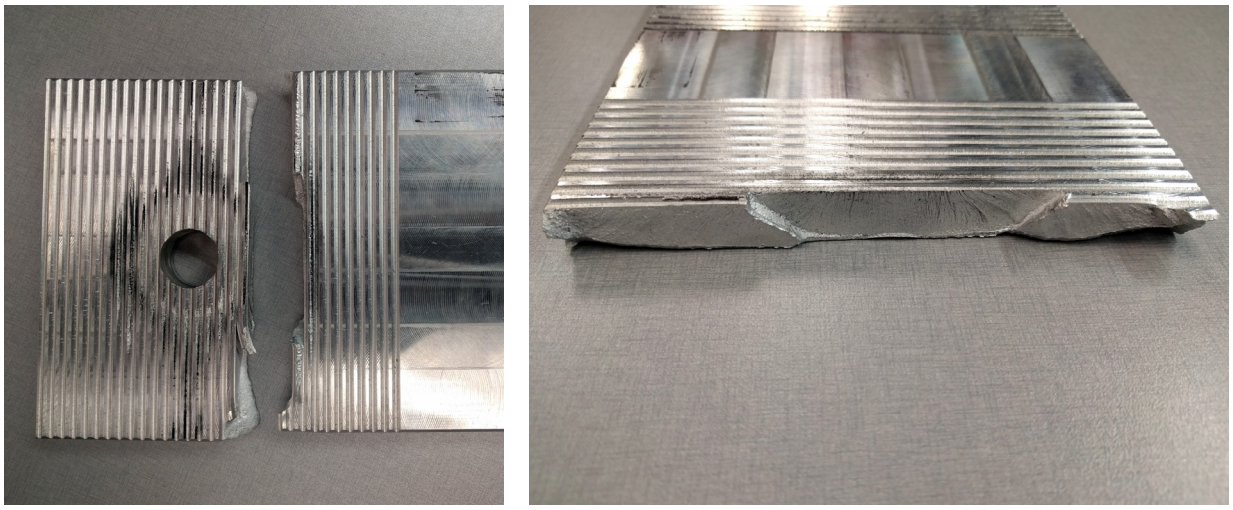

Figure 6.20: Typical fatigue failure

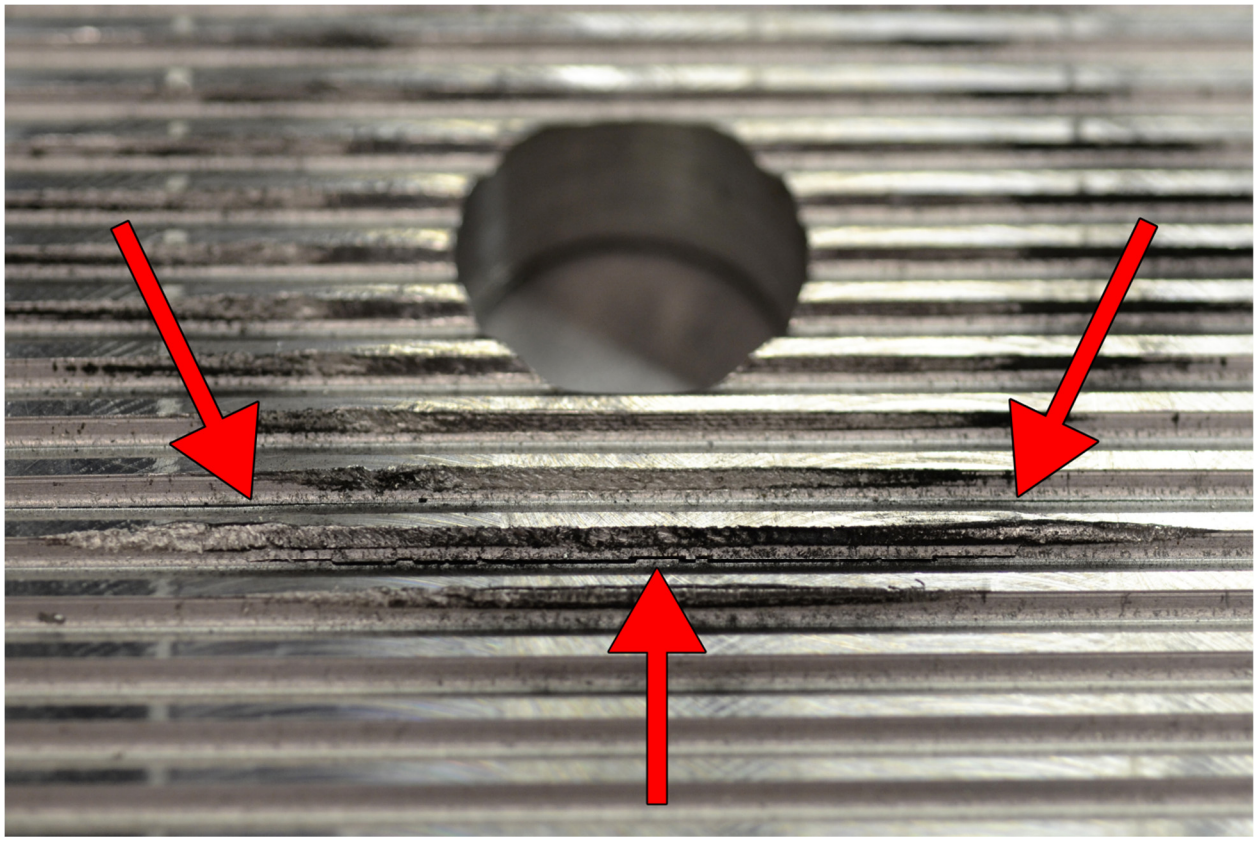

Figure 6.21: Visible fatigue cracks just prior to failure

# 7 Analysis

This chapter compares the experimental results to numerical and mechanistic model solutions. First, the experimental results from the static tests are compared to the mechanistic model presented in Chapter 4. Next, finite element models used to predict the slip loads of the static load test specimens are described, and the modelling assumptions are validated. The experimental results from the static tests are then compared to the predictions made using the finite element models. Next, a strain-life method is used to make fatigue life predictions for the ridged connections, which are compared to experimental results obtained from a pilot study performed to investigate the fatigue performance of this connection type. Finally, preliminary design recommendations for ridged slip-resistant connections are presented, based on the findings presented earlier in the chapter.

## 7.1 Comparison of Mechanistic Model to Experimental Results

The mechanistic model presented in Chapter 4 was used to predict the first slip load of each static test specimen using Equations 4.2-a and 4.2-b. Each slip load was first calculated using nominal values for the friction coefficients of the faying surfaces and the tensile strengths of the fasteners. The nominal friction coefficients were chosen based on Eurocode (2005; 2007) provisions, while the nominal fastener tensile strengths were taken from the relevant ASTM (2015; 2017) standards. The fastener tensile strengths had a direct impact on the predicted slip loads because the clamping force term in Equation 4.2-a, $F_C$, which is equal to the total fastener pre-load, is a function of bolt tensile strength. For the nominal slip load calculations, the connection angle, $\beta$, which measures the angle between the plates and the applied load, was taken as zero for each of the specimens. Once the nominal slip loads were calculated, calibrated friction coefficients and fastener tensile strengths were then computed, which minimized the error between the experimental results and the mechanistic model predictions. These calibrated values are compared to the nominal values in Table 7.1. For the calibration process, upper and lower limits were set on the bolt tensile strengths based on the respective ASTM specifications. A lower limit was not used for the ONESIDE$^{TM}$ blind bolts, however, as it was suspected that blind bolts had a lower tensile strength than standard A325 bolts based on observations made during experimental testing. The calibrated friction coefficients and fastener tensile strengths were believed to be more representative of the actual

experimental testing conditions, and the slip load of each static test specimen was re-calculated using these parameters. For these updated calculations, the connection angle, $\beta$, of each specimen was measured from the footage recorded by the high-speed camera at the point when slip was observed during each test. This yielded the most accurate slip load predictions possible using the mechanistic model.

Table 7.1: Comparison of nominal and calibrated input parameters for mechanistic model

| Parameter | Nominal Value | Calibrated Value |
|---|---|---|
| Machined faying surface friction coefficient | 0.150 | 0.192 |
| Sand-blasted faying surface friction coefficient | 0.370 | 0.500 |
| ¾" F593D stainless steel bolt tensile strength (MPa) | 586 | 642 |
| ½" F593C stainless steel bolt tensile strength (MPa) | 689 | 689 |
| ¾" A325 carbon steel bolt tensile strength (MPa) | 830 | 830 |
| ½" A325 carbon steel bolt tensile strength (MPa) | 830 | 830 |
| ¾" ONESIDE$^{TM}$ blind bolt tensile strength (MPa) | 790 | 790 |

The slip loads predicted by the mechanistic model with both nominal and calibrated input parameters are compared to the experimental results in Figure 7.1. They are also superimposed on the load-displacement curves in the Appendix. The average percent difference between the experimental results and the mechanistic model with calibrated inputs was 12.2%. In contrast, the average percent difference between the experimental results and the mechanistic model with nominal inputs was 19.8%. The greatest error was observed for Specimens FSBB1-S (flat, sand-blasted, one blind bolt w/o sleeve) and FSBS1-S (flat, sand-blasted, one blind bolt w/ sleeve), which consisted of non-ridged sand-blasted faying surfaces and ONESIDE$^{TM}$ blind bolts. The mechanistic model with calibrated inputs under-predicted the slip load of seven static test specimens and predicted the slip load of three specimens with less than 0.02% error. However, it also over-predicted the slip load of four specimens. The mechanistic model with nominal inputs under-predicted the slip load of thirteen specimens and predicted the slip load of one specimen with less than 0.01% error. Overall, the mechanistic model provided improved results with the calibrated input parameters over the nominal input parameters. However, the nominal parameters yielded more conservative results. The slip loads predicted by the mechanistic model generally

aligned well with the experimental observations, although greater deviations were observed for a few of the test specimens.

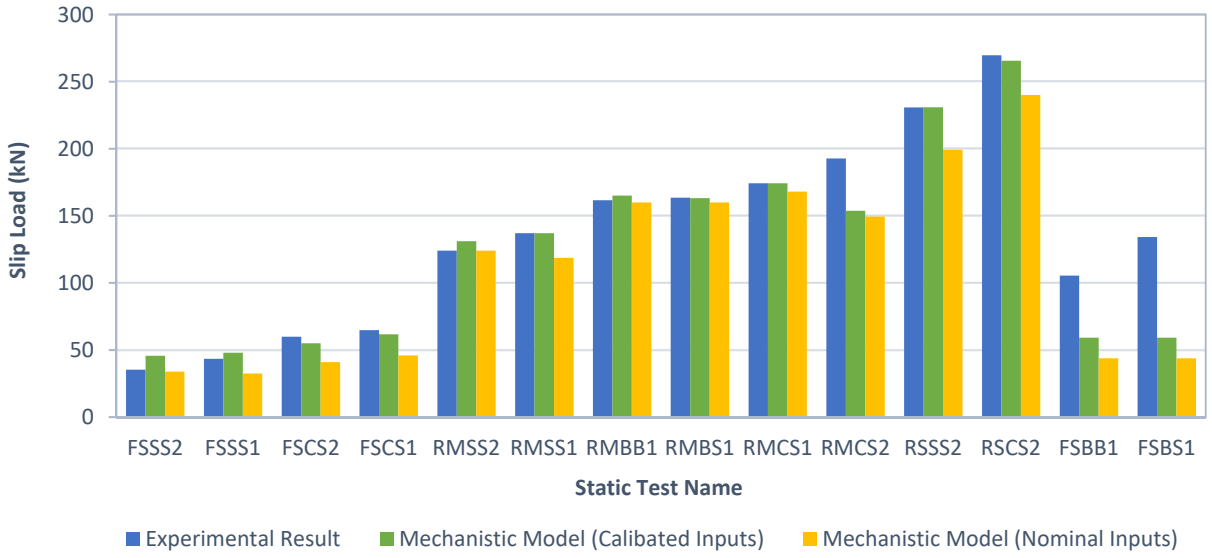


Figure 7.1: Comparison of experimental slip load results to mechanistic model

## 7.2 Finite Element Modelling of Static Test Specimens

The FE models of the static test specimens and the predicted slip loads are presented in the following subsections.

### 7.2.1 Finite Element Models

An FE model of each static test specimen was created using the ABAQUS software suite by Dassault Systèmes. Each model consisted of two 6061-T6 aluminum plates and either one or two fasteners. A typical model assembly is shown in Figure 7.2. Only the unrestrained portion of each specimen was modelled, as the ridged shim plates and test frame grips restricted bending and axial deformations. Each fastener was modelled as a cylinder using the minor diameter of the respective fastener type. The head and nut of each fastener was modelled as a larger cylinder with a diameter equal to the width of the respective washer. Non-linear material behaviour was implemented for each component of the models. Hard contact was specified for the normal behaviour of the faying surfaces between the connecting plates using the penalty constraint enforcement method with linear contact stiffness. Contact separation was enabled so that only compressive forces could be

transferred between the faying surfaces, and any tensile forces resulted in separation of the surfaces. The penalty friction formulation was specified for the tangential behaviour of the faying surfaces with an isotropic frictional coefficient. Similar contact assumptions were specified for the inner surfaces of the bolt holes and the fasteners. However, no contact was observed between the fasteners and the inner surfaces of the bolt holes during the analyses. The head and nut of each fastener was fixed to the exterior face of the respective aluminum plate using tie constraints.

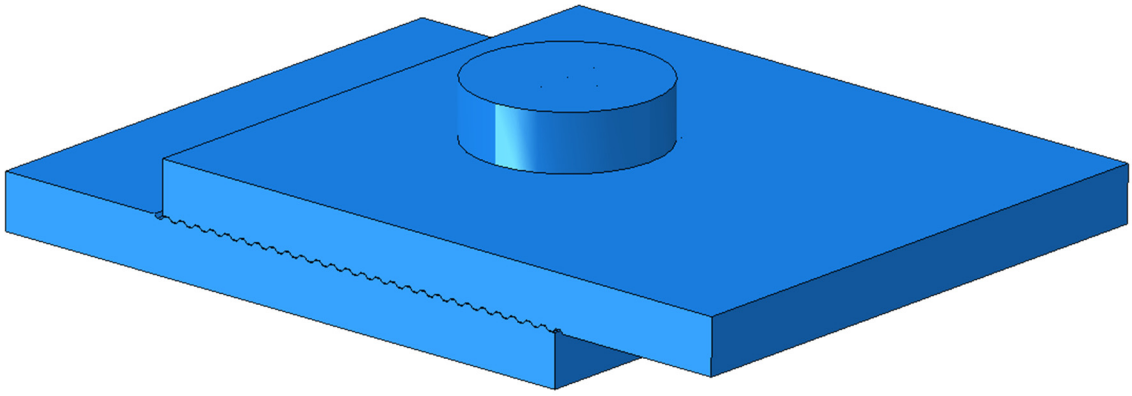

Figure 7.2: Typical FE model of static test specimen

A fixed boundary condition was applied to the end of the lower plate in the initial time step of each simulation. The fasteners were then pre-tensioned to 70% of their minimum specified tensile strength in first time step using temperature loads. A uniaxial coefficient of thermal expansion was specified for each fastener, and the required temperature changes were calculated using the true stress-strain curves of the respective bolt types. The true stress-strain curves used for the models are presented in Section 7.2.3. Contact stabilization was used for all contact surfaces in the first time step to achieve convergence. A uniform displacement boundary condition was applied to the end of the upper plate in the second time step. The displacement of the upper plate was increased from zero in linear increments until a converged solution could no longer be obtained. Implicit time integration was used for each of the time steps.

The FE meshes used for the models consisted of quadratic 3D stress tetrahedrons (C3D10) for the ridged plates and quadratic 3D stress hexahedrons (C3D20R) for the non-ridged plates and fasteners. The curved valley at the bottom of each ridge was simplified to a straight line so that

adequate meshes could be generated for the ridged plates. A structured meshing algorithm was used to generate meshes for the fasteners and non-ridged plates, while a free meshing algorithm was used to generate meshes for the ridged plates. Extensive partitioning was carried out to aid in the generation of adequate meshes. Typical FE meshes for the 3D models are shown in Figures 7.3 through 7.5.

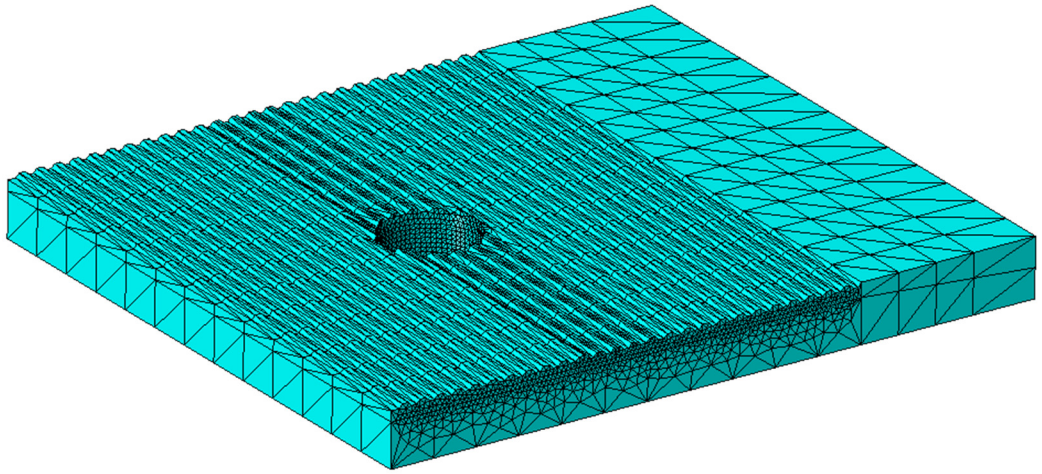

Figure 7.3: Typical FE mesh for ridged plates

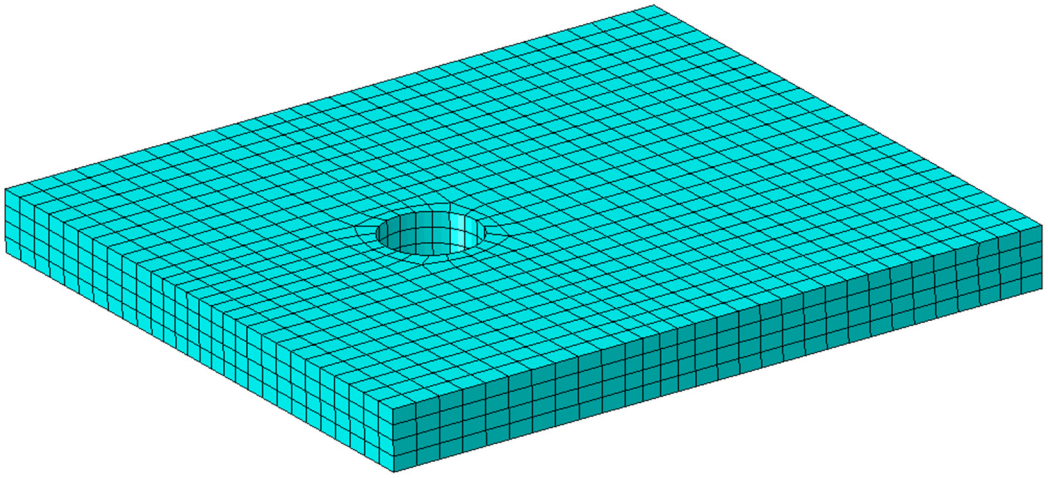

Figure 7.4: Typical FE mesh for non-ridged plates

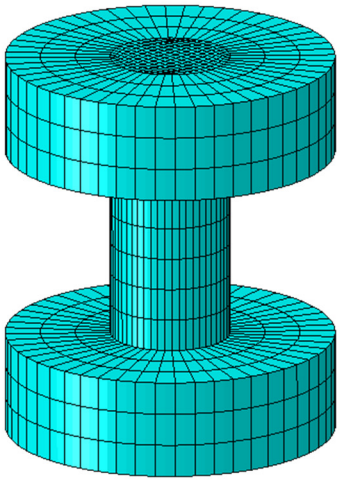

Figure 7.5: Typical FE mesh for fasteners

### 7.2.2 Model Validation

To validate the modelling techniques and assumptions that were used for the FE models of the test specimens, the same modelling techniques and assumptions were used to create a model of a steel slip-critical connection that was previously studied by Ju et al. (2004). The general configuration of the connection is shown in Figure 7.6. A half-geometry model was used for the connection, which was consistent with the original FE model created by Ju et al. A section of the half-geometry model is shown in Figure 7.7. Points A through D shown on the figure represent the points where relative displacement was measured. Relative bolt displacement was computed as the difference between the displacements measured at points A and B, while relative plate displacement was computed as the difference between the displacements measured at points C and D. The FE model that was used for the validation is shown in Figure 7.8.

The results obtained from the FE validation model are compared to the results originally obtained by Ju et al. in Figure 7.9. The load-displacement curves obtained from the FE model generally aligned well with those presented by Ju et al. The greatest difference between the results occurred prior to plate slippage, where the FE model overpredicted stiffness with respect to relative bolt displacement and underpredicted stiffness with respect to relative plate displacement. The FE model underpredicted stiffness with respect to relative plate displacement throughout the entire simulation. These deviations can likely be attributed to the different contact formulations that were

used for the FE validation model compared to the original model developed by Ju et al. Despite the minor differences between the results, the modelling techniques and assumptions used for the test specimen models were shown to be valid.

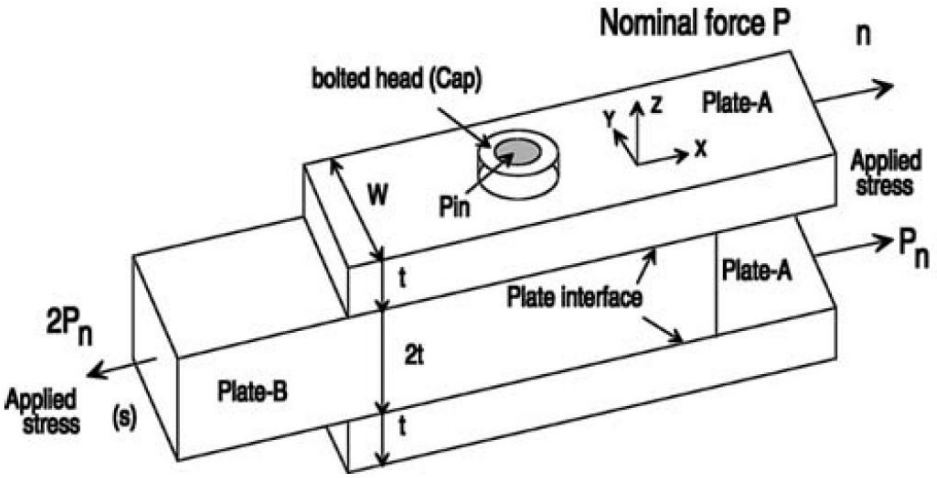


Figure 7.6: General configuration of the slip-critical connection studied by Ju et al. (2004)

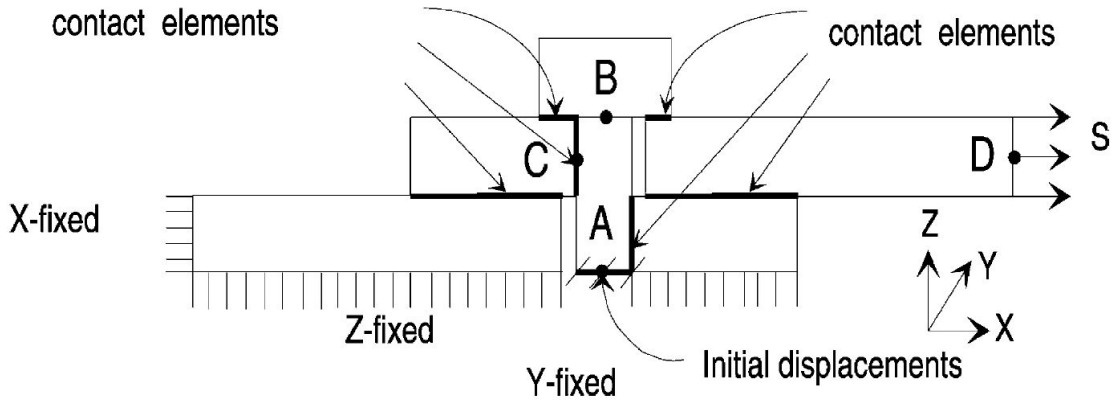


Figure 7.7: Section of half-geometry model used by Ju et al. (2004)

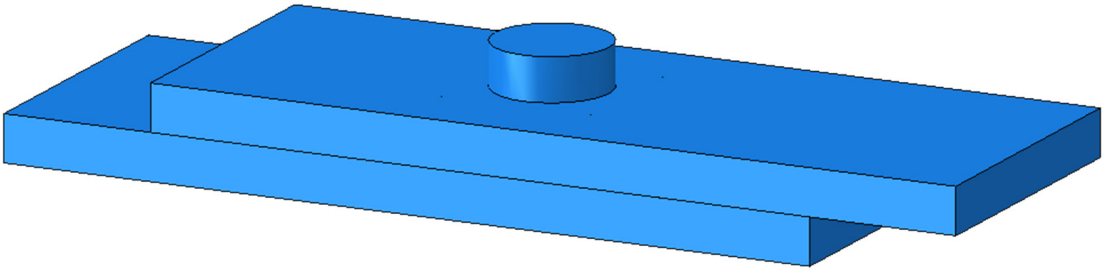

Figure 7.8: FE validation model

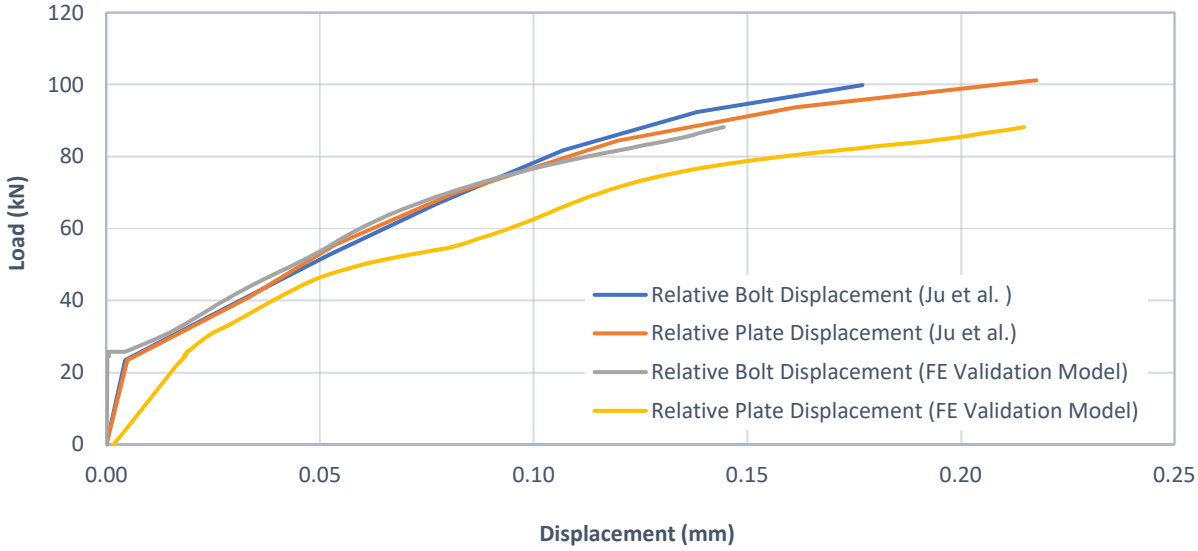


Figure 7.9: Comparison of load-displacement curves for the FE validation model and the original FE model by Ju et al. (2004)

### 7.2.3 Material Properties

Two simulations were completed for each FE model of the static test specimens. The first simulation used the nominal faying surface friction coefficients and fastener tensile strengths presented in Section 7.1, while the second simulation used the calibrated ones. The engineering stress-strain curves associated with the nominal material properties of the stainless steel bolts were previously presented in Figures 5.9 and 5.10 as the lower bound curves. The lower bound curve shown in Figure 5.10 also served as the calibrated engineering stress-strain curve for the F593C stainless steel bolts. A calibrated engineering stress-strain curve was created for the F593D stainless steel bolts by interpolating between the upper and lower bound curves shown in Figure

5.9. The engineering stress-strain curve for the A325 carbon steel bolts was presented in Figure 5.11, and it served as both the nominal and calibrated curves for these bolts. A calibrated engineering stress-strain curve was created for the ONESIDE™ blind bolts by adjusting the curve for the A325 bolts so that it aligned with the calibrated tensile strength presented in Table 7.1. This curve also served as the nominal engineering stress-strain curve for the ONESIDE™ bolts. The engineering stress-strain curve for 6061-T6 aluminum previously presented in Figure 5.7 was used for the aluminum plates in each the FE simulations. Since true stress and logarithmic plastic strain values are required to define non-linear material behaviour for FE models, all of the engineering stress-strain curves were converted to true stress-logarithmic plastic strain curves using Equations 7.1 and 7.2, which are valid up to the onset of necking (Dassault Systèmes, 2013). The resulting curves are presented in Figures 7.10 through 7.14.

$$\sigma_{True} = \sigma_{Engineering} \cdot \left(1 + \varepsilon_{Engineering}\right) \tag{7.1}$$

where:

$\sigma_{True}$ = True stress

$\sigma_{Engineering}$ = Engineering stress

$\varepsilon_{Engineering}$ = Engineering strain

$$\varepsilon_{ln}^{Plastic} = \ln\left(1 + \varepsilon_{Engineering}\right) - \frac{\sigma_{True}}{E} \tag{7.2}$$

where:

$\varepsilon_{ln}^{Plastic}$ = Logarithmic plastic strain

$E$ = Elastic modulus

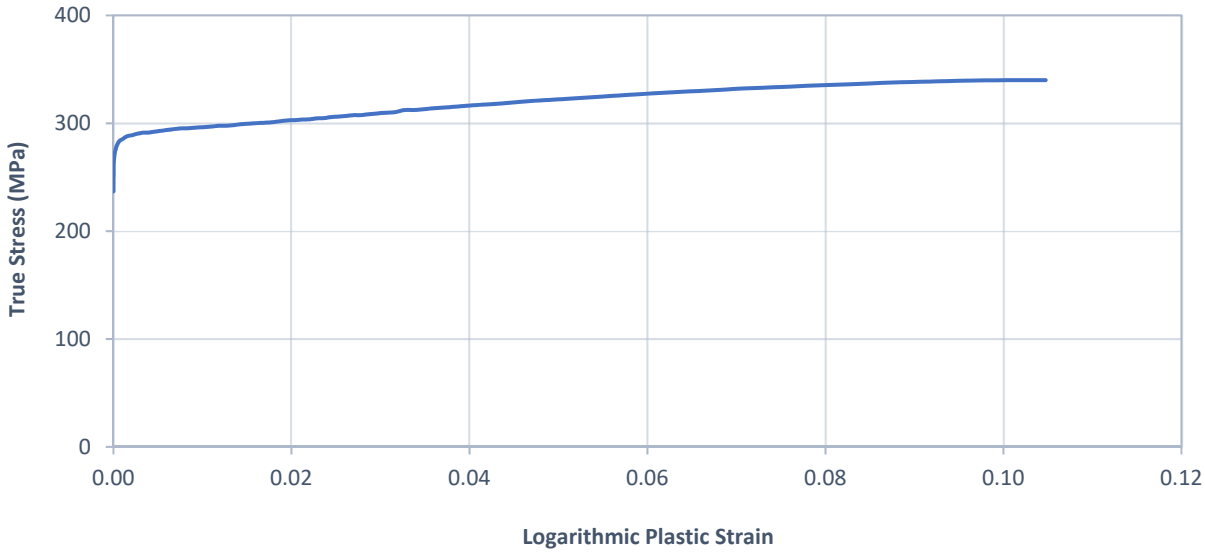


Figure 7.10: True stress-logarithmic plastic strain curve for 6061-T6 aluminum

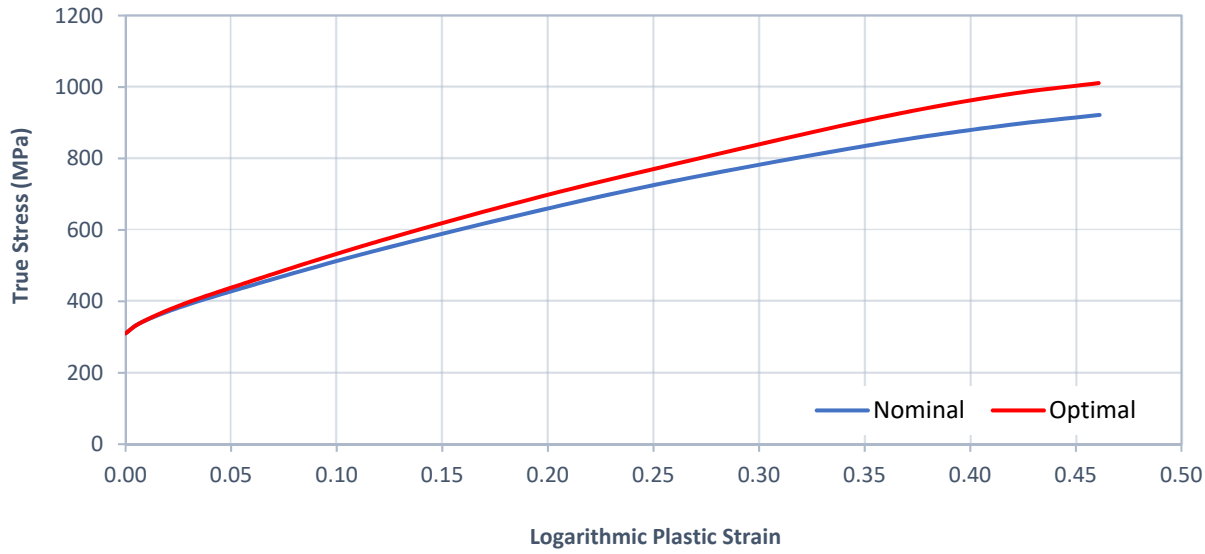


Figure 7.11: True stress-logarithmic plastic strain curves for F593D stainless steel bolts

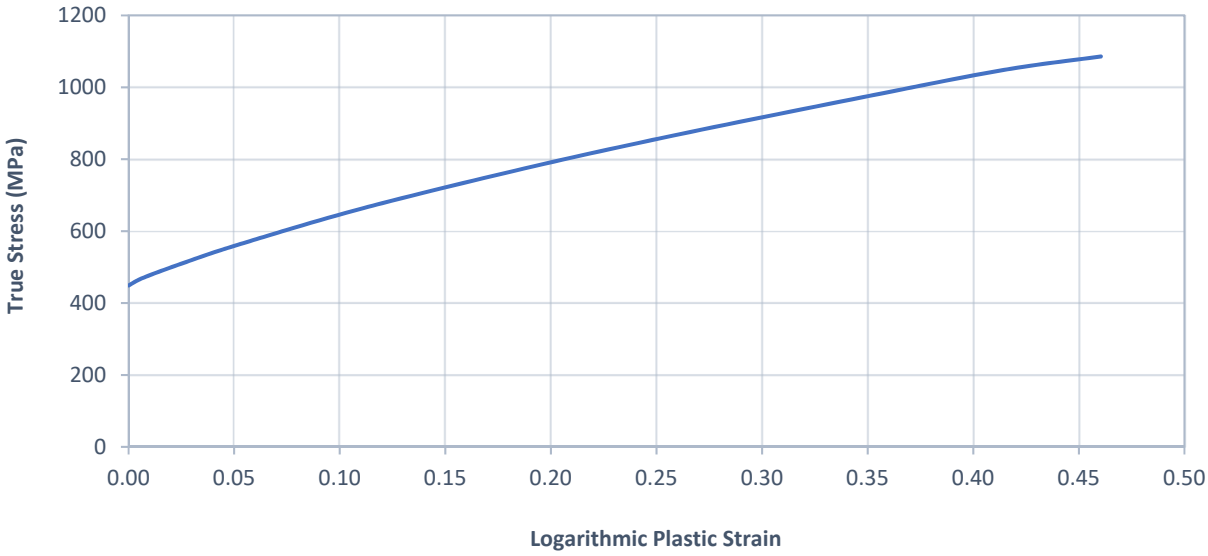


Figure 7.12: True stress-logarithmic plastic strain curve for F593C stainless steel bolts

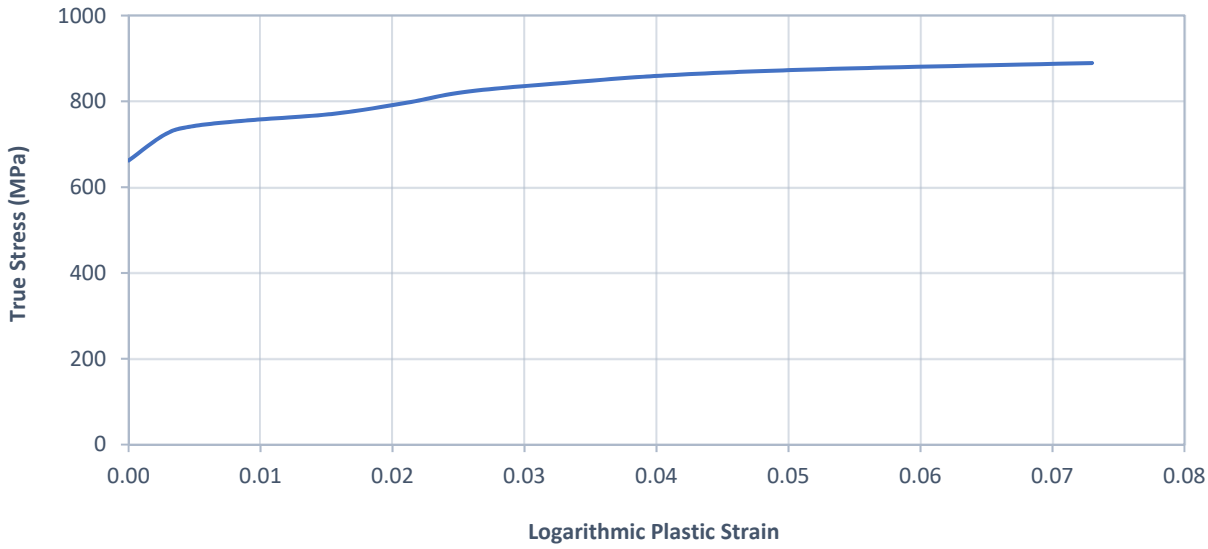


Figure 7.13: True stress-logarithmic plastic strain curve for A325 carbon steel bolts

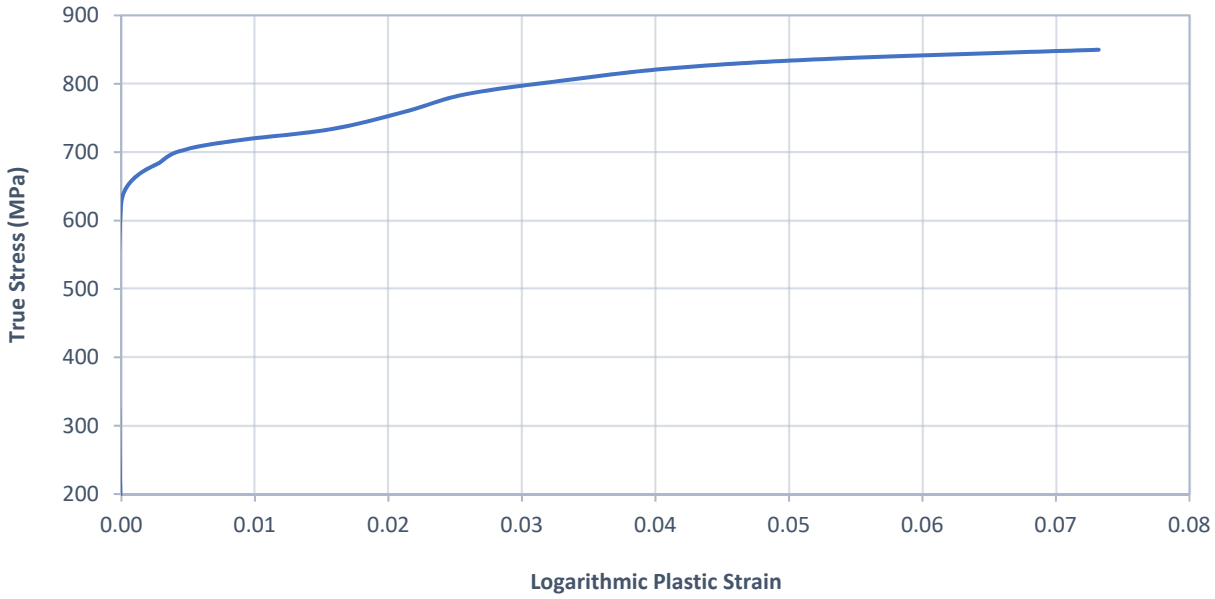


Figure 7.14: True stress-logarithmic plastic strain curve for ONESIDE$^{TM}$ carbon steel blind bolts

### 7.2.4 Comparison of Results to Experimental Tests and Mechanistic Model

The slip loads predicted by the FE models are compared to the experimental results and the mechanistic model results in Figure 7.15. The load-displacement curves predicted by the models up to initial slippage are compared to the experimental load-displacement curves in the Appendix. A typical comparison is provided in Figure 7.16 for Specimen RMSS1-S (ridged, not sand-blasted, on stainless steel bolt). As seen in the figure, the slip load predicted by the FE model with calibrated inputs aligned well with the experimental slip load of this specimen. However, the shapes of the FE load-displacement curves differed from that of the experimental curve. While the experimental curve was quite rounded with no clear transition between linear and non-linear behaviour, the FE curves consisted of linear segments followed by sudden decreases in slope and subtle curvature. The linear portions of the two FE curves had approximately the same slope, however the sudden change in slope occurred at a lower load level for the FE model with nominal inputs compared to the FE model with calibrated inputs. The sudden change from linear to non-linear behaviour was more apparent in the curves predicted by the FE models that included stainless steel bolts than in the curves predicted by the FE models that included carbon steel bolts. In all cases, the load-displacement curves predicted by the FE models initially underpredicted the stiffness of the static test specimens.

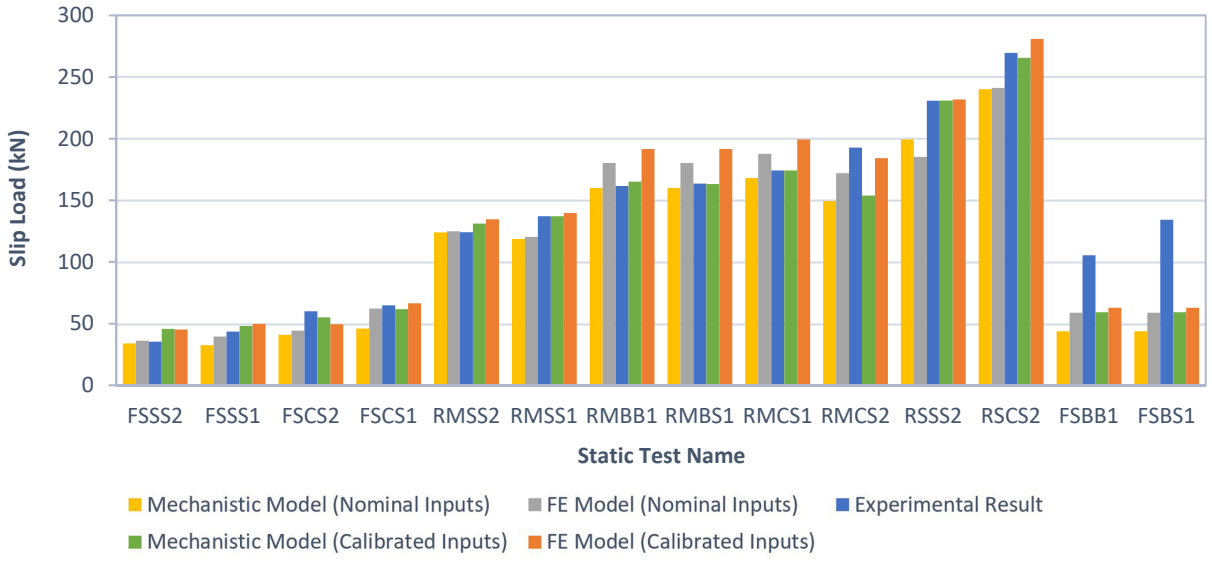


Figure 7.15: Comparison of FE slip load results to experimental tests and mechanistic model

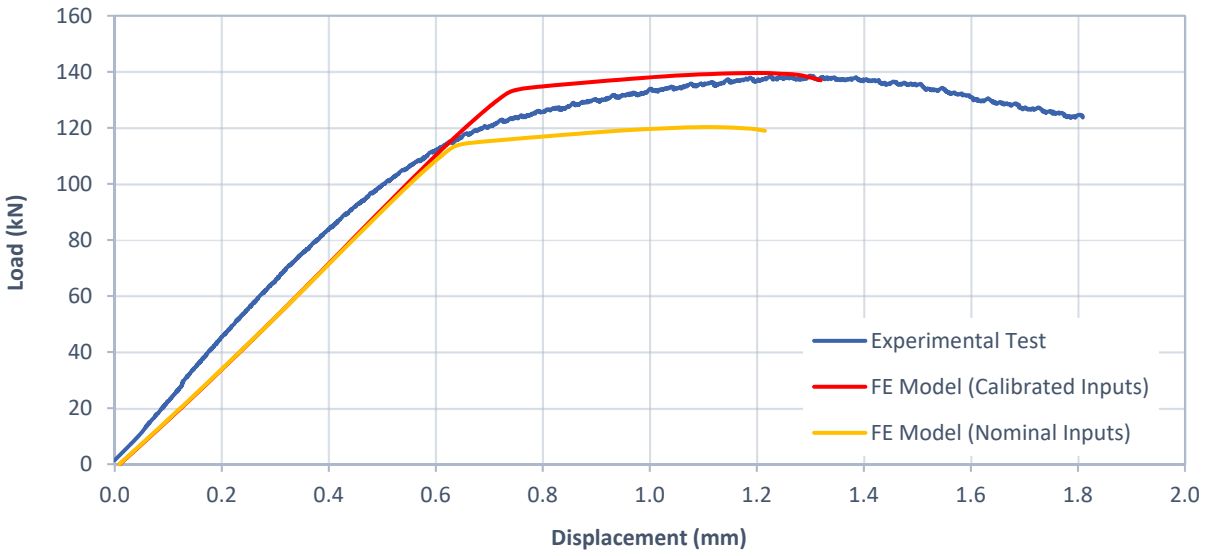


Figure 7.16: Comparison of FE and experimental load-displacement curves for Specimen RMSS1-S

In general, the FE models predicted the slip loads of the static test specimens less accurately than the mechanistic model with calibrated inputs. However, the FE models generally predicted the slip loads more accurately than the mechanistic model with nominal inputs. The average percent difference between the experimental results and the FE models with calibrated inputs was 15.1%,

whereas the average percent difference between the experimental results and the FE models with nominal inputs was 15.9%. The greatest error was observed for Specimens FSBB1-S (flat, sand-blasted, one blind bolt w/o sleeve) and FSBS1-S (flat, sand-blasted, one blind bolt w/ sleeve), which is consistent with the observations previously made for the mechanistic model. The FE models with calibrated inputs under-predicted the slip load of four static test specimens and over-predicted the slip load of ten specimens. The FE models with nominal inputs under-predicted the slip load of nine specimens and over-predicted the slip load of five specimens. This demonstrates that the FE slip load predictions were generally less conservative than the mechanistic model predictions since the mechanistic model provided fewer over-predictions. The FE results aligned fairly well with the mechanistic model, however, with an average percent difference of 10.6% over all 28 models. The average percent difference values between all of the results sets are summarized in Table 7.2 and a detailed breakdown of the slip load results is provided in Table 7.3.

Table 7.2: Summary of average slip load percent difference values for experimental tests, mechanistic model, and FE models (%)

| Results Set | FE-N | FE-C | MM-N | MM-C |
|---|---|---|---|---|
| ET | 15.9 | 15.1 | 19.8 | 12.2 |
| MM-C | 11.9 | 7.7 | 19.8 | - |
| MM-N | 13.6 | 26.5 | - | - |
| FE-C | 12.7 | - | - | - |

FE-N = FE models with nominal input parameters
FE-C = FE models with calibrated input parameter
MM-N = Mechanistic model with nominal input parameters
MM-C = Mechanistic model with calibrated input parameters
ET = Experimental tests

Table 7.3: Comparison of experimental and predicted slip loads with percent difference values

| Specimen | ET | FE-N | | FE-C | | MM-N | | MM-C | |
|---|---|---|---|---|---|---|---|---|---|
| | (kN) | (kN) | (%) | (kN) | (%) | (kN) | (%) | (kN) | (%) |
| FSSS2 | 35.3 | 36.0 | 2.0 | 45.2 | 28.0 | 33.9 | 3.9 | 45.6 | 29.3 |
| FSSS1 | 43.4 | 39.4 | 9.2 | 49.7 | 14.5 | 32.4 | 25.2 | 47.9 | 10.5 |
| FSCS2 | 59.9 | 44.2 | 26.2 | 49.4 | 17.5 | 40.8 | 31.8 | 55.0 | 8.2 |
| FSCS1 | 64.8 | 62.2 | 4.0 | 66.4 | 2.5 | 46.0 | 29.1 | 61.6 | 4.9 |
| RMSS2 | 124.0 | 124.8 | 0.6 | 134.6 | 8.5 | 124.0 | 0.0 | 131.1 | 5.7 |
| RMSS1 | 137.0 | 120.3 | 12.2 | 139.6 | 1.9 | 118.6 | 13.4 | 137.0 | 0.0 |
| RMBB1 | 161.6 | 180.3 | 11.6 | 191.6 | 18.6 | 159.9 | 1.0 | 165.0 | 2.1 |
| RMBS1 | 163.5 | 180.3 | 10.3 | 191.6 | 17.2 | 159.9 | 2.2 | 163.1 | 0.2 |
| RMCS1 | 174.2 | 187.7 | 7.7 | 199.3 | 14.4 | 168.0 | 3.5 | 174.2 | 0.0 |
| RMCS2 | 192.7 | 172.0 | 10.7 | 184.2 | 4.4 | 149.4 | 22.5 | 153.7 | 20.2 |
| RSSS2 | 230.8 | 185.2 | 19.8 | 231.8 | 0.4 | 199.3 | 13.7 | 230.8 | 0.0 |
| RSCS2 | 269.6 | 241.1 | 10.6 | 280.8 | 4.2 | 240.1 | 11.0 | 265.6 | 1.5 |
| FSBB1 | 105.4 | 58.8 | 44.2 | 62.8 | 40.4 | 43.7 | 58.5 | 59.1 | 43.9 |
| FSBS1 | 134.2 | 58.8 | 56.2 | 62.8 | 53.2 | 43.7 | 67.4 | 59.1 | 56.0 |

* Percent difference values are with respect to the experimental slip load results

FE-N = FE model with nominal input parameters
FE-C = FE model with calibrated input parameter
MM-N = Mechanistic model with nominal input parameters
MM-C = Mechanistic model with calibrated input parameters
ET = Experimental test

### 7.2.5 Comparison of Results to Digital Image Correlation Software

The displacement fields predicted by the FE model of Specimen RMCS1-S (ridged, not sand-blasted, one carbon steel bolt) are compared to those computed by the digital image correlation (DIC) software in Figure 7.17. The displacement fields shown in the figure were generated just before ridge slippage occurred. Similar patterns can be seen between the DIC and FE results, however the exact displacement magnitudes were not compared in this study.

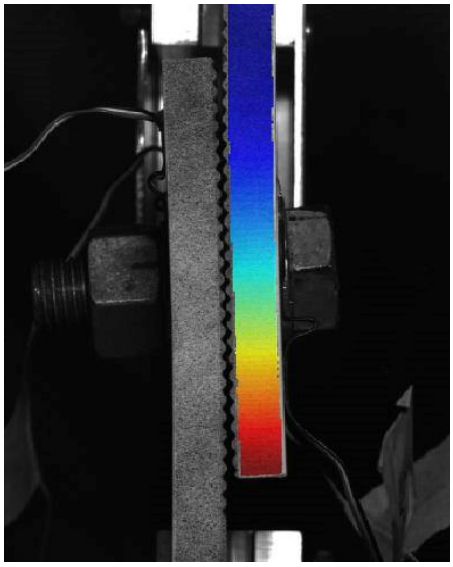

(a) DIC vertical displacement field

(b) FE vertical displacement field

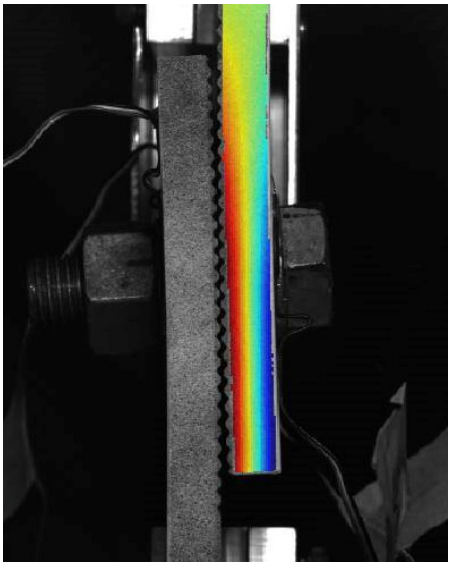

(c) DIC horizontal displacement field

(d) FE horizontal displacement field

Figure 7.17: Comparison of DIC and FE model displacement fields

## 7.3 Strain-Life Analysis of Cyclic Test Specimens

The strain-life methodology and resulting fatigue life predictions for the cyclic load test specimens are presented in the following subsections.

### 7.3.1 Strain-Life Model

The Smith-Watson-Topper (SWT) criterion, given by Equation 7.3, was used to predict the number of cycles required for fatigue crack initiation for each of the three cyclic test specimens using the aluminum fatigue parameters previously provided in Table 5.3. The applied stresses were determined from a 3D FE model of Specimen RMSS1-S (ridged, not sand-blasted, one stainless steel bolt) at the location where fatigue cracks were observed to initiate during experimental testing. This FE model was similar to the one presented in Section 7.2. However, linear-elastic material behaviour was adopted rather than non-linear behaviour. Since the mesh used for the 3D FE model was quite coarse, a 2D model of the specimen was also created, which used a much finer mesh so that a stress correction factor could be derived for the 3D model. The 2D stress correction model is shown in Figure 7.18 and the mesh used for the model, which consisted of biquadratic plane strain quadrilateral elements (CPE8R), is shown in Figure 7.19. A mesh refinement study was performed for the model, and it was found that reducing the number of elements by 50% caused the predicted stress values to decrease by about 0.5% on average. Unlike the 3D model, the 2D model did not include a pre-tensioned stainless steel bolt, and the clamping force was instead applied externally. The principle stresses in the direction of the applied loading were compared between the 2D and 3D models at multiple points along the ridged faying surfaces away from the bolt hole location at varying load levels, and it was found that the stresses predicted by the 2D model were about 1.6 times greater than those predicted by the 3D model on average. The stress distribution predicted by the 2D model around a typical ridge is shown in Figure 7.20. The corrected stress values predicted by the 3D FE model were used to determine the stress concentration factor relating the applied nominal axial stress to the linear-elastic stress at the fatigue crack location. This stress concentration factor was found to be approximately 6.0.

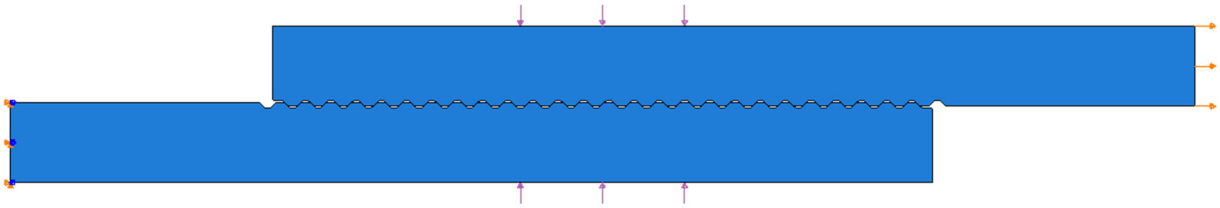

Figure 7.18: 2D stress correction model for strain-life analysis

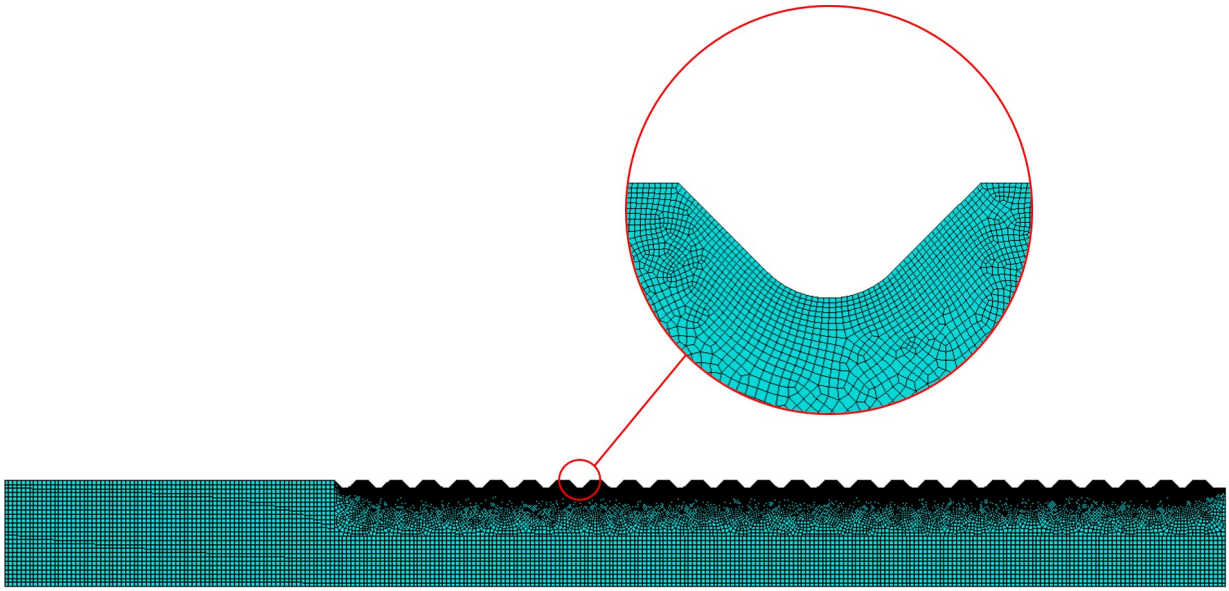

Figure 7.19: FE mesh used for 2D stress correction model

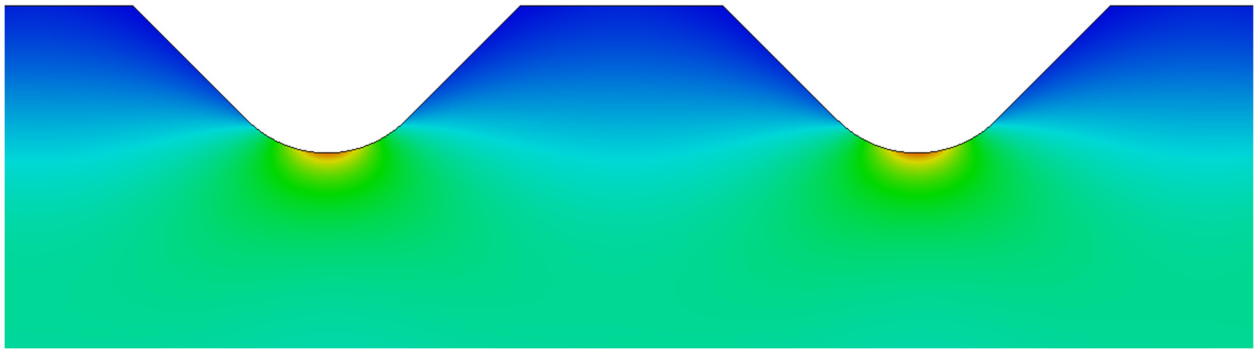

Figure 7.20: Distribution of principle stress in the direction of applied loading around a typical ridge

$$\sigma_{max} \cdot \frac{\Delta\varepsilon}{2} = \frac{(\sigma'_f)^2}{E} \cdot (2 \cdot N_f)^{2 \cdot b} + \varepsilon'_f \cdot \sigma'_f \cdot (2 \cdot N_f)^{b+c} \quad (7.3)$$

where:

$N_f$ = Number of cycles to failure

$\sigma_{max}$ = Maximum true stress

$\Delta\varepsilon$ = True strain range

$E$ = Modulus of elasticity

$\sigma'_f$ = Fatigue strength coefficient

$\varepsilon'_f$ = Fatigue ductility coefficient

$b$ = Fatigue strength exponent

$c$ = Fatigue ductility exponent

The linear-elastic stresses and strains from the 3D FE model were converted to real stresses and strains by implementing Neuber's Rule (NR) and the equivalent strain energy density (ESED) method. It has been shown that NR typically overestimates notch-tip stresses and strains, whereas the ESED method typically underestimates notch-tip stresses and strains, leading to upper and lower bound estimates of fatigue life, respectively (Shin et al., 1994). NR and the ESED method are expressed mathematically by Equations 7.4 and 7.5, and are demonstrated graphically by Figure 7.21. In both cases, the non-linear material behaviour was defined using the Ramberg-Osgood relationship given by Equation 7.6. The maximum true stress values and true stress ranges that were computed for each cyclic test specimen using NR and the ESED method are provided in Table 7.4

Table 7.4: Maximum true stress values and true strain ranges used for strain-life analysis

| Test No. | NR Maximum True Stress (MPa) | NR True Strain Range | ESED Maximum True Stress (MPa) | ESED True Strain Range |
|---|---|---|---|---|
| 1 | 311 | 0.0095 | 304 | 0.0089 |
| 2 | 297 | 0.0060 | 291 | 0.0060 |
| 3 | 213 | 0.0031 | 213 | 0.0031 |

$$\sigma^e \cdot \varepsilon^e = \sigma^a \cdot \varepsilon^a \tag{7.4}$$

$$\int_0^{\varepsilon^e} \sigma^e \, d\varepsilon^e = \int_0^{\varepsilon^a} \sigma^a \, d\varepsilon^a \tag{7.5}$$

where:

$\sigma^e$ = Linear-elastic stress

$\varepsilon^e$ = Linear-elastic strain

$\sigma^a$ = True (actual) stress

$\varepsilon^a$ = True (actual) strain

$$\varepsilon^a = \frac{\sigma^a}{E} + \left(\frac{\sigma^a}{K'}\right)^{\frac{1}{n'}} \tag{7.6}$$

where:

$K'$ = Strength coefficient

$n'$ = Strain hardening exponent

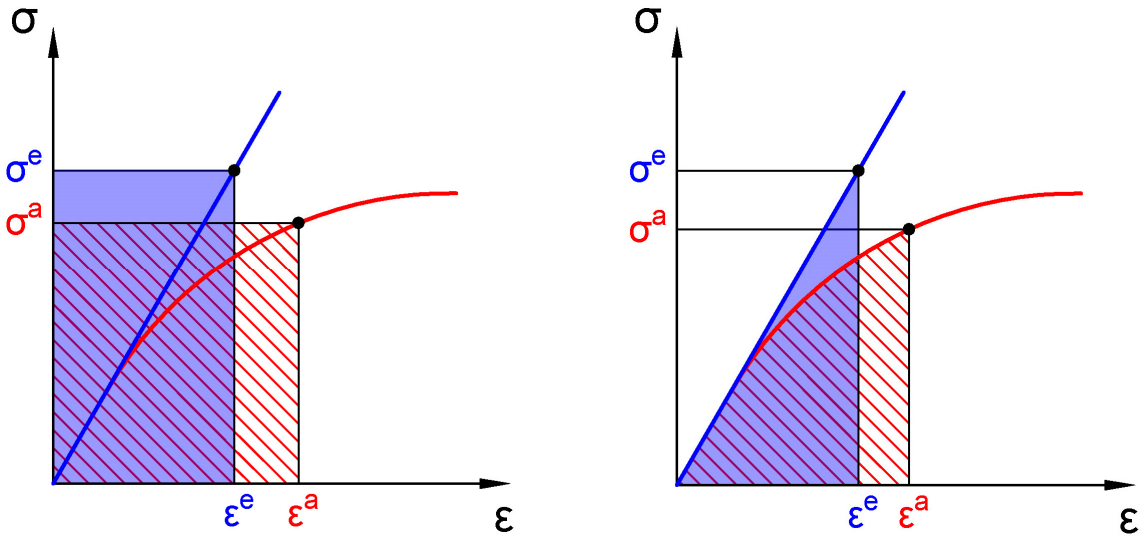


(a) Neuber's Rule (NR) (b) ESED method

Figure 7.21: Visual representation of Neuber's Rule (NR) and the equivalent strain energy density (ESED) method

### 7.3.2 Comparison of Results to Experimental Tests

The fatigue lives of the cyclic test specimens predicted by the strain-life model are compared to the experimental results in Table 7.5. The model greatly underpredicted the fatigue lives of the first two specimens using both NR and the ESED method for computing the non-linear stresses and strains. These first two specimens were subjected to the largest load ranges, and the strain-life results suggest that most of the applied load cycles contributed to crack growth rather than crack initiation. The model also underpredicted the fatigue life of the third specimen by approximately 20% using both NR and the ESED method. It was found that the ESED method provided a slightly more conservative estimate than NR. Based on the results of the strain-life analysis, it appears that the SWT criterion may be able to provide good fatigue life estimates for ridged slip-resistant connections in the high cycle range when used in combination with NR or the ESED method. Further experimental testing would be needed to confirm this, however, and the initial results show that the model may be overly conservative for applied stress ranges which fall above a certain threshold. Since the high cycle (low stress range) domain is generally the most relevant for bridge design, this limitation of the model may not be an issue from a practical standpoint.

Table 7.5: Comparison of strain-life analysis results to experimental tests

| Test No. | Load Range (kN) | NR Prediction (Cycles) | ESED Prediction (Cycles) | Experimental Result (Cycles) |
|---|---|---|---|---|
| 1 | 81.0 | 1,101 | 1,427 | 13,941 |
| 2 | 54.9 | 7,902 | 8,898 | 51,927 |
| 3 | 28.8 | 2,739,178 | 2,733,420 | 3,422,910 |

## 7.4 Design Recommendations for Ridged Slip-Resistant Connections

It has been shown that the mechanistic model presented in Chapter 4 can be used to predict the slip resistance of ridged slip-resistant connections with good accuracy as long as certain conditions are met. A design equation has therefore been proposed for computing the slip-resistance of aluminum ridged slip-resistant connections at the service limit state, and it is given by Equation 7.7. This equation combines the existing design equation for aluminum slip-critical connections presented in CSA S6 (CSA Group, 2014) with Equations 4.1-a and 4.1-b of the mechanistic model

presented in Chapter 4. A faying surface friction coefficient of 0.3 has been built into the design equation, which is in line with the existing CSA S6 provisions. All faying surfaces of ridged slip-resistant connections should be sand-blasted to ensure that a friction coefficient of at least 0.3 is available. A friction coefficient of 0.3 yields a critical ridge angle of about 73.3 degrees in accordance with Equation 4.1-b, and the allowable ridge angle, α, for ridged slip-resistant connections has therefore been set at 75% of the critical angle, or 55 degrees. A limit has also been set on the maximum allowable slip-resistance so that it is not possible for the slip-resistance to exceed the factored shear resistance of the bolts. This was done to ensure a ductile failure mode, and to prevent designers from relying on slip-resistance at the ultimate limit state. The coefficient of 0.5 in the proposed design equation comes from the product of $0.7 \cdot 0.75 \cdot c_1$, where 0.7 is a multiplier for $F_u$ which reflects the CSA S6 requirement that the minimum bolt pre-tension must be at least 70% of the minimum specified bolt tensile strength, 0.75 is a reasonable conversion from nominal bolt area to stress area, and $c_1$ is a coefficient that is used to relate the coefficient of friction and initial specified bolt tension to achieve an acceptable probability of slip (Kulak et al., 2001; Kulak, 2005). The magnitude of $c_1$ in the existing CSA S6 design equation for aluminum slip-critical connections is approximately 0.95. This same value was adopted for the proposed design equation since the minimum specified coefficient of friction is unchanged and the faying surface conditions of aluminum ridged slip-resistant connections should be similar to those of standard aluminum slip-critical connections. However, further research would be required to verify the suitability of this value for aluminum connections with ridged faying surfaces.

$$V_S = 0.5 \cdot n \cdot m \cdot A_b \cdot F_u \cdot \left( \frac{\mathrm{Sin}(\alpha) + 0.3 \cdot \mathrm{Cos}(\alpha)}{\mathrm{Cos}(\alpha) - 0.3 \cdot \mathrm{Sin}(\alpha)} \right) \quad < \quad V_r \quad , \quad \alpha \leq 55° \tag{7.7}$$

where:

$V_S$ = Connection slip-resistance
$n$ = Number of bolts
$m$ = Number of slip planes
$A_b$ = Nominal cross-sectional area of bolts
$F_u$ = Minimum specified bolt tensile strength
$\alpha$ = Ridge angle
$V_r$ = Factored shear resistance of bolts

Unlike Equations 4.2-a and 4.2-b, the proposed design equation does not include any terms to account for the connection angle, $\beta$. Although bending due to eccentric loading can reduce the slip-resistance of ridged slip-resistant connections, it is difficult to predict the angle of rotation at slip without performing experimental testing or computer modelling. However, it was shown in Section 7.1 that the mechanistic model provided conservative results when a connection angle of zero was assumed in combination with nominal input parameters, despite non-zero connection angles being observed during experimental testing.

# 8 Finite Element Modelling of Modular Deck Panels

This chapter presents a finite element (FE) model that was used to predict the normal and shear forces that are transferred between modular aluminum bridge deck panels. The results of the model are then presented and discussed in relation to the experimental observations.

## 8.1 Finite Element Model

A 3D FE model of a modular aluminum bridge deck section was created, which consisted of three extrusions spanning between two longitudinal bridge girders as shown in Figure 8.1. Each extrusion consisted of triangular voids, and measured 312 mm in width, 90 mm in height, and 1,200 mm in length. The top and bottom surface of each extrusion measured 10 mm in thickness, while the diagonal and vertical components measured 5 mm in thickness. The extrusions were modelled using 2D linear quadrilateral shell elements (S4R) with non-linear material behaviour and were connected to one another using rough non-separable contacts between the faying surfaces. The FE mesh used for each extrusion is shown in Figure 8.2. Pin supports were used to model the connections to the bridge girders at each end of the extrusions. A wheel load was applied to the middle extrusion as a uniform pressure to simulate the maximum service wheel load of a CL-625-ONT truck from CSA S6 (CSA Group, 2014).

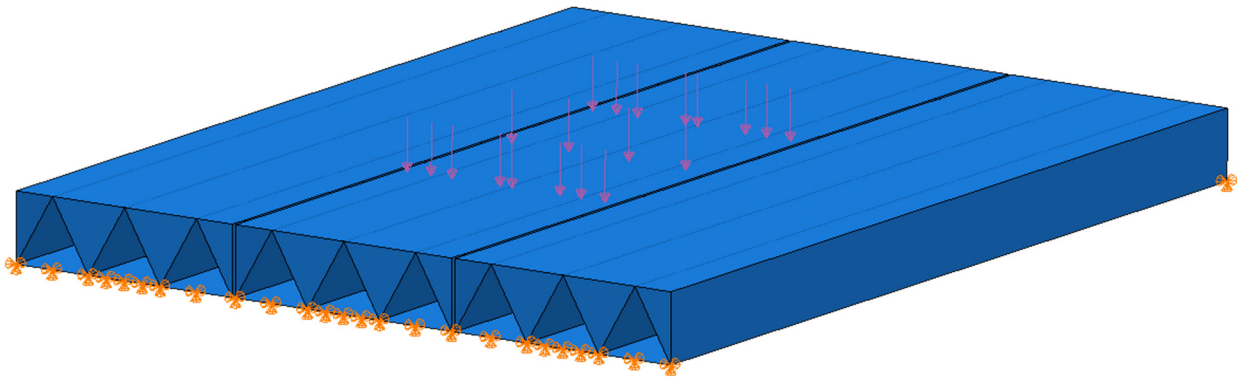

Figure 8.1: FE model of modular aluminum bridge deck section

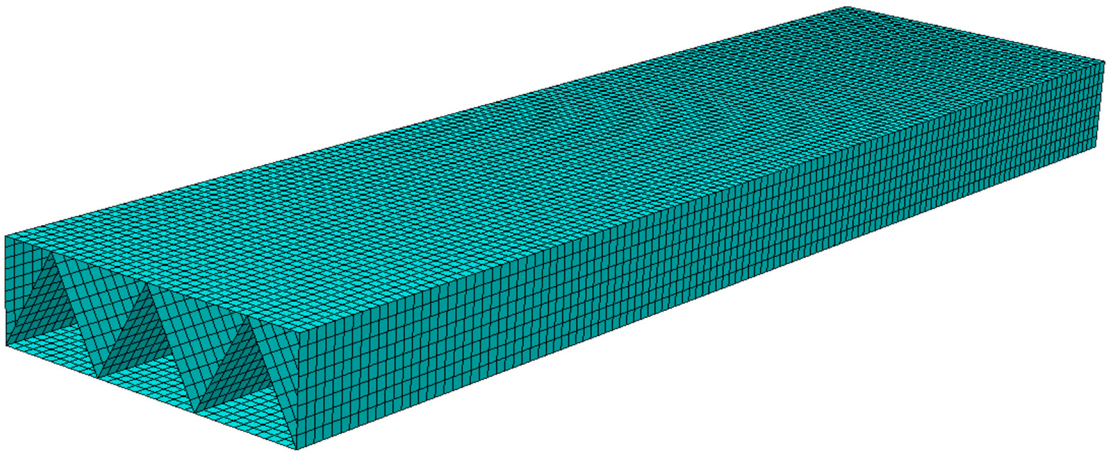

Figure 8.2: Typical FE mesh for modular aluminum bridge deck extrusion

## 8.2 Results

The contact surface between two of the connecting extrusions was subdivided into twenty-two smaller surfaces as shown in Figure 8.3. The central surfaces measured 127 mm in width to match the dimensions of the experimental test specimens, and the end surfaces measured 28.5 mm in width. A python script was used to compute the net forces that were transferred between each pair of contact surfaces based on the normal and shear stress distributions predicted by the model. The resulting net forces are shown in Figures 8.4 through 8.6. It was found that approximately 30% of the total wheel load was transferred to each of the two exterior extrusions, while the remaining 40% was carried by the middle extrusion. The majority of the vertical force was transferred across the bottom portion of the contact surface, as demonstrated in Figure 8.4, and the greatest vertical shear force occurred at midspan. The total vertical shear force transferred between two of the connecting extrusions was about 27 kN, which is far less than all of the slip loads observed for the ridged static test specimens. This suggests that a single bolted connection may be sufficient to fasten the studied extrusions together for a deck span of 1.2 m. Illustrations of how such a connection might be implemented are shown in Figure 8.7. Additional bolts may be required, however, to better distribute the clamping force across the connections. Experimental testing and further computer modelling would be necessary to confirm the required number of bolts for the connections. The bolted connections would also need to transfer tensile forces between the extrusions, as demonstrated by Figure 8.5 where tension can be seen along the bottom portion of

the contact surface. The greatest tensile force occurred at midspan, and the total tensile force transferred between two of the connecting extrusions was about 59 kN. The horizontal shear forces transferred between the extrusions were found to be quite small, as demonstrated by Figure 8.7, and it is believed that the friction between the faying surfaces would be sufficient to carry these forces.

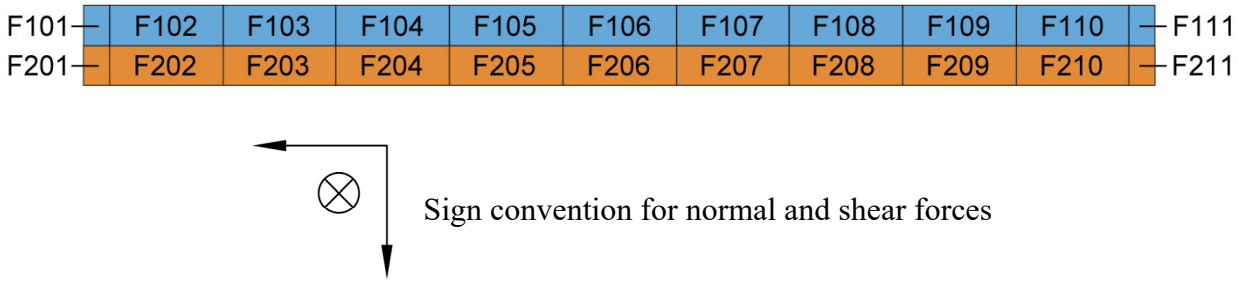


Figure 8.3: Subdivision of contact surface between adjacent deck extrusions

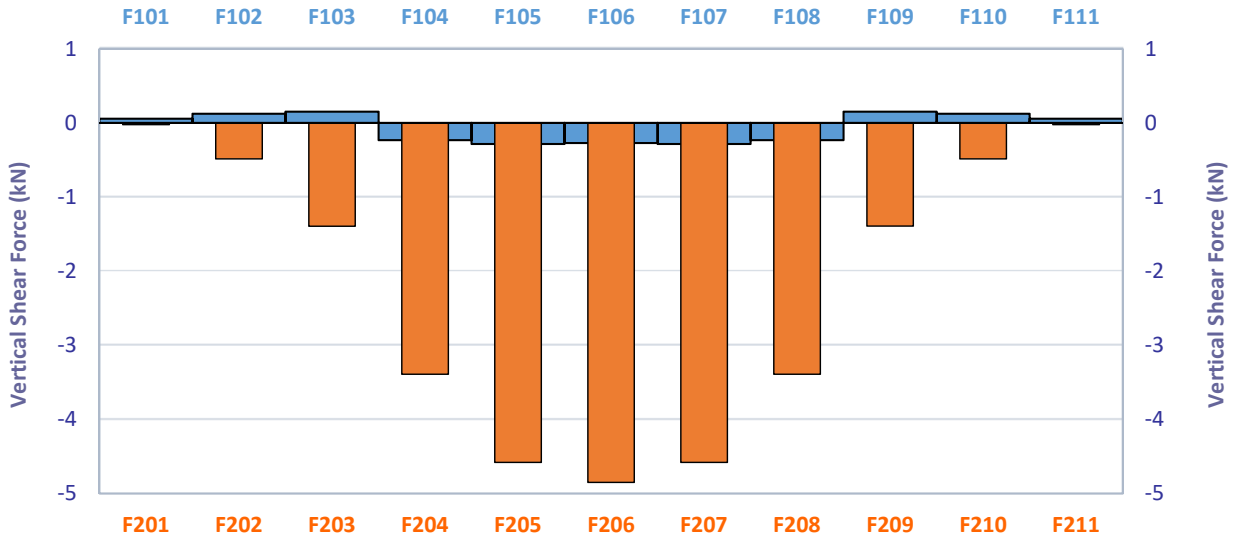


Figure 8.4: Vertical shear forces transferred between modelled deck extrusions

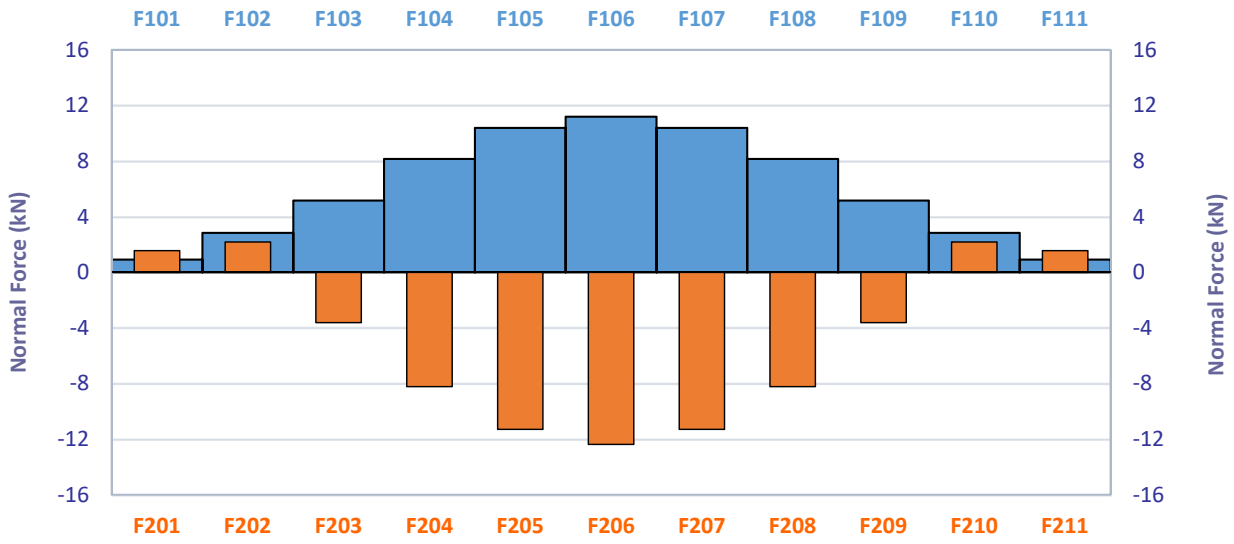


Figure 8.5: Normal forces transferred between modelled deck extrusions

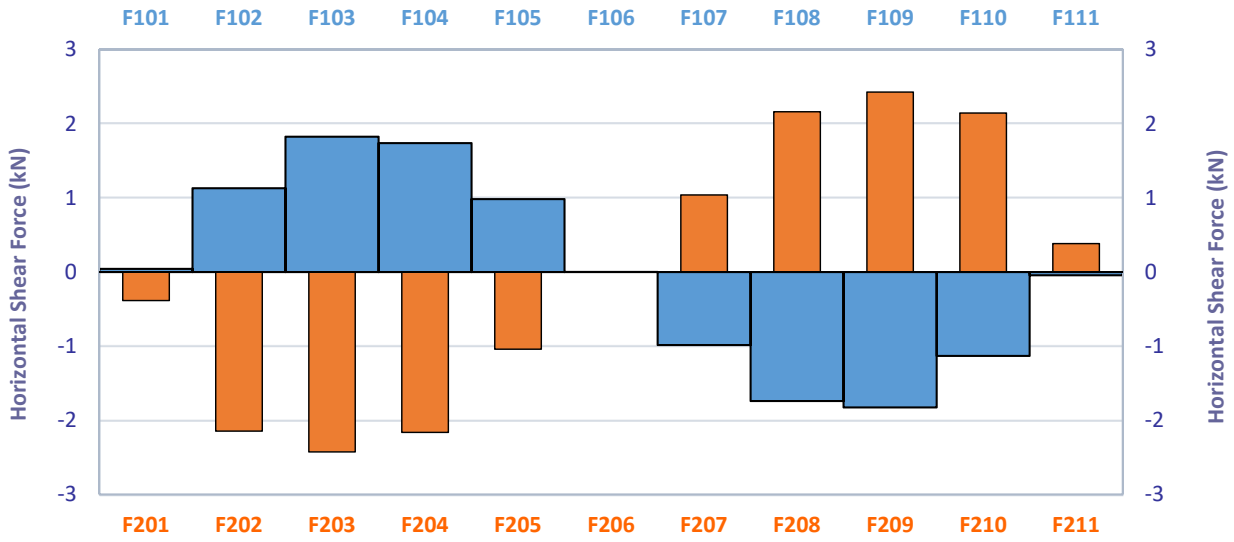


Figure 8.6: Horizontal shear forces transferred between modelled deck extrusions

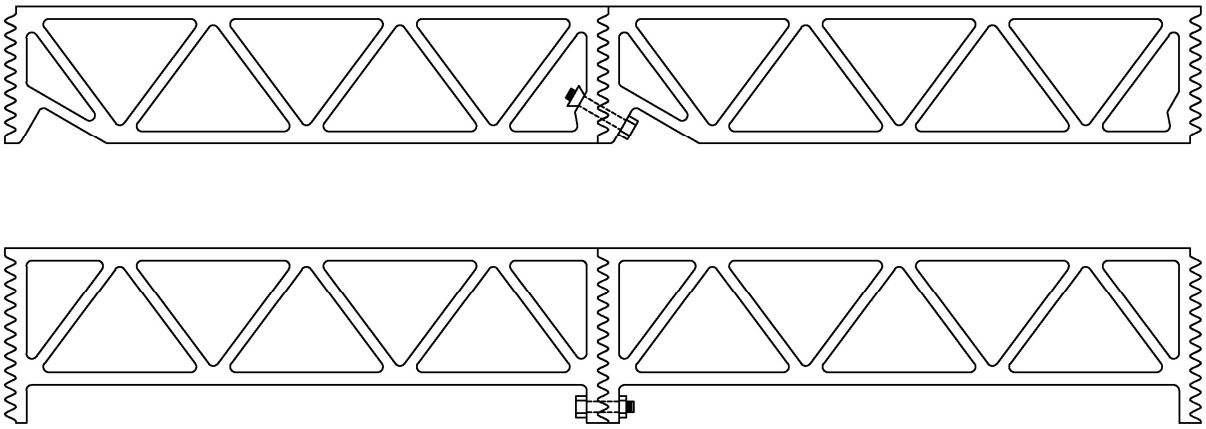

Figure 8.7: Preliminary connection concepts for modular aluminum bridge deck extrusions

# 9 Conclusions and Recommendations

This chapter presents the conclusions that have been drawn from the findings of the research presented within this thesis. Recommendation for further research are then discussed.

## 9.1 Conclusions

The conclusions presented in this chapter have been divided into two major areas of study. First, the conclusions pertaining to the experimental results are presented, followed by the conclusions pertaining to the mechanistic and numerical analyses.

### 9.1.1 Experimental Testing

The following conclusions have been drawn from the experimental testing of aluminum ridged slip-resistant connections:

- The ridged slip-resistant connections were found to provide improved slip-resistance, strength and ductility in comparison to non-ridged slip-resistant connections. The average increases were found to be approximately 230%, 51%, and 29%, respectively.

- The greatest improvement in slip-resistance and strength was observed for the ridged connections with sand-blasted faying surfaces. However, improvement was still present without sand-blasted faying surfaces. The average increases in slip-resistance and strength for the ridged connections with sand-blasted faying surfaces were found to be approximately 452% and 135%, respectively, in comparison to the non-ridged connections. In contrast, the average increases in slip-resistance and strength for the ridged connections with non-sand-blasted faying surfaces were found to be approximately 156% and 22%, respectively, in comparison to the non-ridged connections.

- The ridged connections with A325 carbon steel bolts offered greater strength than those with F593 stainless steel bolts. However, the stainless steel bolts provided greater ductility.

- The ridged connections with stainless steel bolts out-performed the non-ridged connections with carbon steel bolts in terms of slip-resistance, strength, and ductility, regardless of whether the ridged connections had sand-blasted faying surfaces.

- The ridged connections with single ¾" bolts exhibited more ductility than those with two ½" bolts. However, it was found that two A325 carbon steel bolts provided greater strength than a single A325 carbon steel bolt despite a decreased total cross-sectional area. The opposite trend was observed for stainless steel bolts where a single bolt provided greater strength.

- ONESIDE$^{TM}$ blind bolts by Ajax Fasteners were shown to be a useful alternative to standard A325 bolts, offering far greater ductility when used in eccentrically-loaded lap-splice connections.

- An aluminum ridged slip-resistant connection with a single ¾" stainless steel bolt was able to withstand 3.4 million cycles under constant amplitude loading with a peak load equal to approximately 21% of the static capacity of the connection.

### 9.1.2 Mechanistic and Numerical Analyses

The following conclusions have been drawn from the mechanistic and numerical analyses of aluminum ridged slip-resistant connections:

- A simple mechanistic model was created to predict the slip loads of ridged slip-resistant connections, and the results were found to align well with the experimental observations. When calibrated input parameters were used, the average percent difference between the mechanistic model predictions and the experimental results was found to be approximately 12%, with percent difference values ranging from 0% to 56%. When nominal input parameters were used, the average percent difference between the mechanistic model predictions and the experimental results was found to be approximately 20%, with percent difference values ranging from 0% to 67%.

- Finite element modelling was carried out to predict the behaviour of the experimental test specimens, and the results were found to align well with both the experimental observations and the mechanistic model. When calibrated input parameters were used, the average percent difference between the slip loads predicted by the finite element models and those observed during experimental testing was found to be approximately 15%, with percent difference values ranging from 0% to 53%. When nominal input parameters were used, the average percent difference between the slip loads predicted by the finite element models and those observed during experimental testing was found to be approximately 16%, with percent difference values ranging from 1% to 56%.

- The mechanistic model typically provided slip load predictions that were more accurate than the finite element model predictions when calibrated input parameters were used. However, the finite element model predictions were found to be more accurate than the mechanistic model predictions when nominal input parameters were used. In general, the mechanistic model provided slip load predictions that were more conservative than those provided by the finite element models.

- The mechanistic model was combined with the existing design equation for aluminum slip-critical connections presented in CSA S6 Canadian Highway Bridge Design Code (CSA Group, 2014) to produce a new design equation for computing the slip-resistance of aluminum ridged slip-resistant connections at the service limit state.

- The Smith-Watson-Topper (SWT) strain-life criterion has demonstrated good potential for predicting the fatigue lives of aluminum ridged slip-resistance connections in the high cycle range when used in combination with Neuber's Rule (NR) or the equivalent strain energy density (ESED) method.

- Preliminary finite element modelling was carried out to analyze the forces that are transferred between modular aluminum bridge deck extrusions, and the results demonstrated that ridged slip-resistant connections are a feasible option for the connections between adjacent extrusions.

## 9.2 Recommendations for Future Work

The following recommendations for further research pertaining to aluminum ridged slip-resistant connections have been proposed:

- The experimental testing carried out in the current research focused on a single ridge profile, which was fabricated using a CNC machine and included jagged edges. Further experimental testing is therefore recommended to study a range of smooth ridge profiles, preferably ones that are fabricated using an aluminum extrusion process. Such testing is necessary to provide further validation of the mechanistic model presented in the current research, and to generate accurate S-N curves for connection details with smooth interlocking ridges.

- The experimental testing carried out for the current study was also limited to the testing of eccentrically-loaded lap-splice specimens. Further experimental testing is therefore recommended to study aluminum ridged slip-resistant connections in a larger variety of configurations.

- The structural behaviour of modular aluminum bridge deck systems was not studied in detail in the current research. Further computer modelling of these systems is therefore recommended so that a modular aluminum bridge deck product that employs the ridged slip-resistant connection concept can be designed.

- Once a modular aluminum bridge product is designed, it is recommended that sample specimens be fabricated and tested in a variety of configurations under both static and cyclic loading conditions. Such testing is necessary to demonstrate whether the product is adequate for implementation on Canadian highway bridges.

## References


Ajax Fasteners. (2017). *Ajax ONESIDE Brochure V4.* Retrieved from http://www.ajaxfast.com.au

Annan, C.-D., & Chiza, A. (2013). Characterization of slip resistance of high strength bolted connections with zinc-based metallized faying surfaces. *Engineering Structures 56*, 2187–2196.

Annan, C.-D., & Chiza, A. (2014). Slip resistance of metalized–galvanized faying surfaces in steel bridge construction. *Journal of Constructional Steel Research 95*, 211-219.

Arrayago, I., Real, E., & Gardner, L. (2015). Description of stress–strain curves for stainless steel alloys. *Materials and Design 87*, 540-552.

Arrien, P., Bastien, J., & Beaulieu, D. (2001). Rehabilitation of bridges using aluminum decks. *Canadian Journal of Civil Engineering*, 992-1002.

ASTM International. (2010). *ASTM B308/B308M-10: Standard Specification for Aluminum-Alloy 6061-T6 Standard Structural Profiles.* West Conshohocken, PA 19428-2959: ASTM International.

ASTM International. (2015). *ASTM F3125/F3125M-5a: Standard Specification for High Strength Structural Bolts, Steel and Alloy Steel, Heat Treated, 120 ksi (830 MPa) and 150 ksi (1040 MPa) Minimum Tensile Strength, Inch and Metric Dimensions.* West Conshohocken, PA 19428-2959: ASTM International.

ASTM International. (2017). *ASTM F593-17: Standard Specification for Stainless Steel Bolts, Hex Cap Screws, and Studs.* West Conshohocken, PA 19428-2959: ASTM International.

Bouchaïr, A., Averseng, J., & Abidelah, A. (2008). Analysis of the behaviour of stainless steel bolted connections. *Journal of Constructional Steel Research 64*, 1264–1274.

CSA Group. (2005). *CAN/CSA-S157-05: Strength Design in Aluminum.* Mississauga, ON: CSA Group.

CSA Group. (2014). *CAN/CSA-S6-14: Canadian Highway Bridge Design Code.* Mississauga, ON: CSA Group.

Das, S. K., & Kaufman, J. G. (2007). Aluminum Alloys for Bridges and Bridge Decks. *The Minerals, Metals & Materials Society*, 61-72.

Dassault Systèmes. (2013). *ABAQUS 6.13 Documentation Collection.* Dassault Systèmes.

Dobmeier, J. M., Barton, F. W., Gomez, J. P., Massarelli, P. J., & McKeel Jr., W. T. (2001). Failure Study of an Aluminum Bridge Deck Panel. *Journal of Performance of Constructed Facilities 15(2)*, 68-75.

European Committee for Standardization. (2005). *Eurocode 3 - Design of steel structures.* Brussels: CEN.

European Committee for Standardization. (2007). *Eurocode 9 - Design of Aluminum Structures.* Brussels: CEN.

Fadden, M., Hayatdavoudi, A., & Seibi, A. (2015). High Performance Surface Coatings for Bolted Slip-Critical Connections. *Structures Congress 2015* (pp. 2101-2111). Portland: ASCE.

Gardner, L. (2005). The use of stainless steel in structures. *Progress in Structural Engineering and Materials 7*, 45–55.

Growdon, J., Riegel, R., & Tremplin, R. (1934). Heavy bridge floor replaced with aluminum. *Civil Engineering, ASCE, Vol. 4, No. 3*, 113-117.

Ju, S., Fan, C., & Wu, G. (2004). Three-dimensional finite elements of steel bolted connections. *Engineering Structures 26*, 403–413.

Kulak, G. (2005). *High Strength Bolting for Canadian Engineers.* Willowdale, ON: Canadian Institute of Steel Construction.

Kulak, G., Fisher, J., & Struik, J. (2001). *Guide to Design Criteria for Bolted and Riveted Joints: Second Edition.* Chicago, IL: American Institute of Steel Construction.

Lee, J., Goldsworthy, H., & Gad, E. (2010). Blind bolted T-stub connections to unfilled hollow section columns in low rise structures. *Journal of Constructional Steel Research 66*, 981-992.

Lee, J., Goldsworthy, H., & Gad, E. (2011). Blind bolted moment connection to sides of hollow section columns. *Journal of Constructional Steel Research 67*, 1900–1911.

Mirza, F., Liu, K., & Chen, X. (2017). Cyclic Stress-Strain Behavior and Low Cycle Fatigue Life of AA6061 Aluminum Alloy. *Light Metals 2017* (pp. 447-452). The Minerals, Metals & Materials Society.

Roberge, P. R. (2008). *Corrosion Engineering Principles and Practice.* New York: McGraw-Hill.

Saleem, M. A., Mirmiran, A., Xia, J., & Mackie, K. (2012). Experimental Evaluation of Aluminum Bridge Deck System. *Journal of Bridge Engineering 17(1)*, 97-106.

Shin, C., Man, K., & Wang, C. (1994). A practical method to estimate the stress concentration of notches. *International Journal of Fatigue 16(4)*, 242-256.

Siwowski, T. (2006). Aluminium Bridges – Past, Present and Future. *Structural Engineering International*, 286-293.

Siwowski, T. (2009a). FEM modelling and analysis of a certain aluminium bridge deck panel. *Archives of Civil Engineering, LV, 3*, 347-365.

Siwowski, T. (2009b). Structural behaviour of aluminium bridge deck panels. *Engineering Structures 31*, 1349-1353.

Svensson, L., & Pettersson, L. (1990). Aluminium Extrusion Bridge Rehabilitation System. *International Conference on Bridge Management* (pp. 777-783). London: Springer.

Varedian, M. (2016). *A New Improved Type of Friction Connection - An Experimental Study (Master's Thesis).* Luleå University of Technology, Sweden.

Walbridge, S., & de la Chevrotiere, A. (2012). Opportunities for the use of aluminum in vehicular bridge construction. *Aluminum Association of Canada Report*.

# Appendix

Experimental and Analytical Results for Static Test Specimens

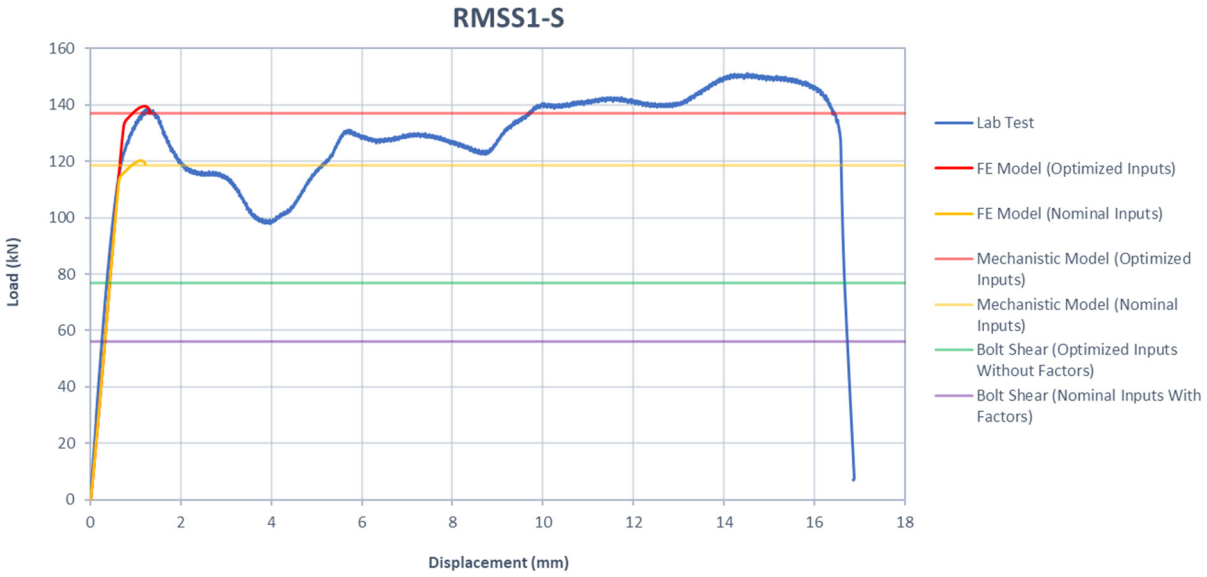


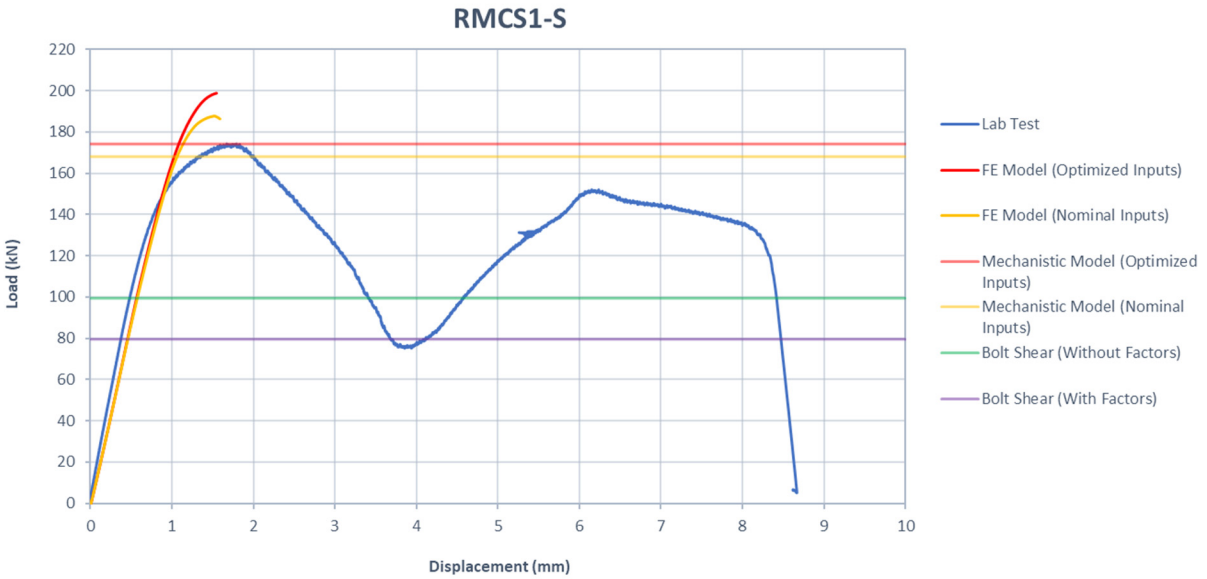


RMBB1
Load (kN)
Displacement (mm)
0
20
40
60
80
100
120
140
160
180
200
0
5
10
15
20
25
Lab Test
FE Model (Optimized Inputs)
FE Model (Nominal Inputs)
Mechanistic Model (Optimized Inputs)
Mechanistic Model (Nominal Inputs)
Bolt Shear (Without Factors)
Bolt Shear (With Factors)

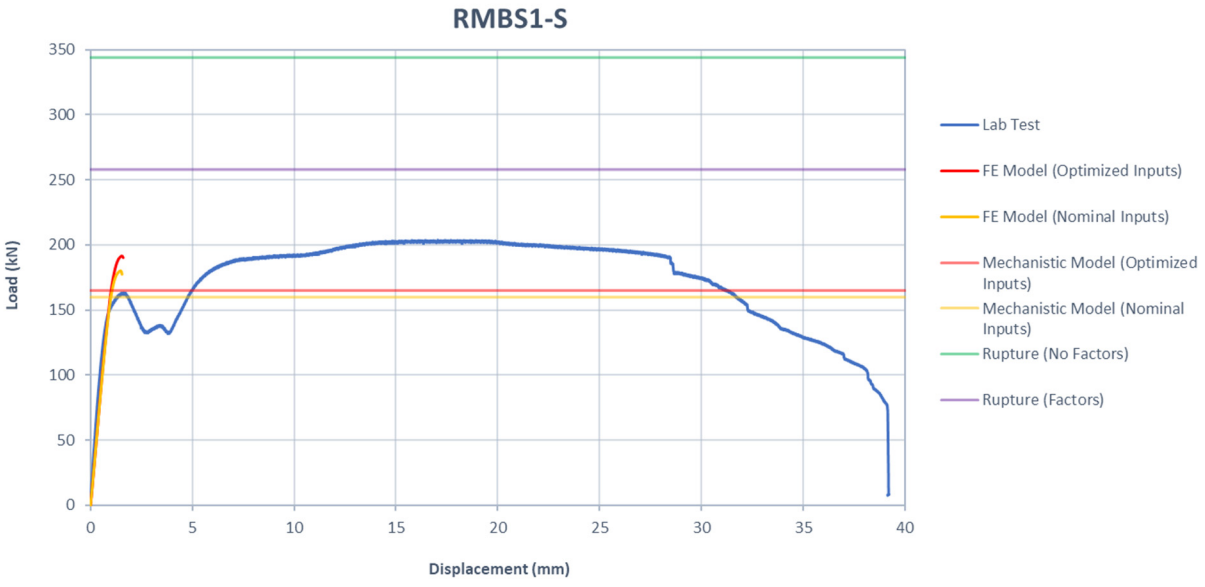
RMBS1-S
Load (kN)
Displacement (mm)
0
50
100
150
200
250
300
350
0
5
10
15
20
25
30
35
40
Lab Test
FE Model (Optimized Inputs)
FE Model (Nominal Inputs)
Mechanistic Model (Optimized Inputs)
Mechanistic Model (Nominal Inputs)
Rupture (No Factors)
Rupture (Factors)

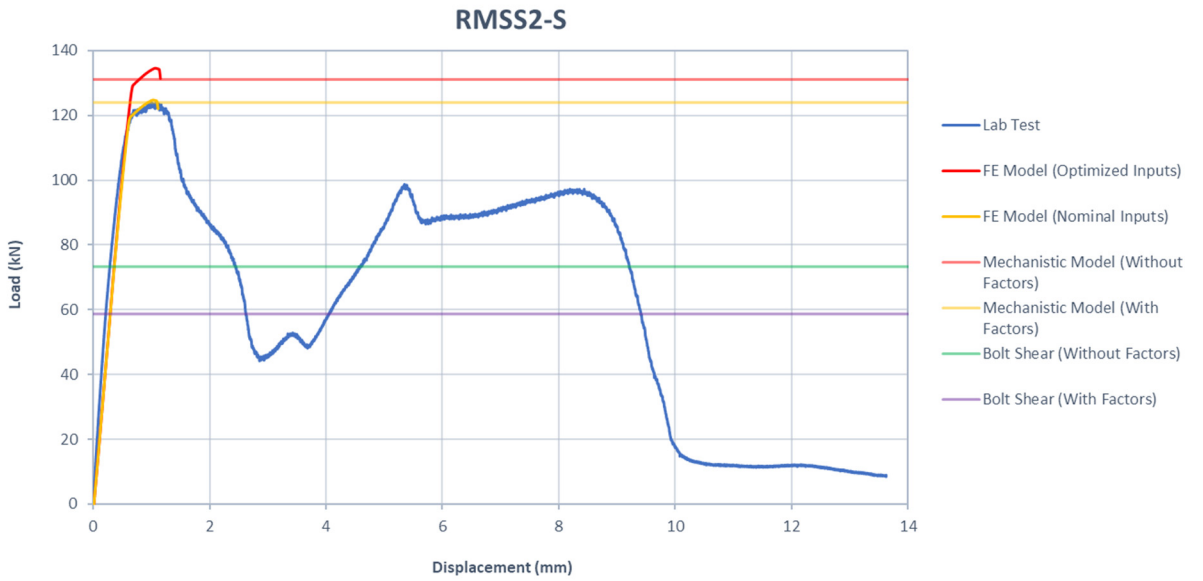
RMSS2-S
Load (kN)
Displacement (mm)
0
20
40
60
80
100
120
140
0
2
4
6
8
10
12
14
Lab Test
FE Model (Optimized Inputs)
FE Model (Nominal Inputs)
Mechanistic Model (Without Factors)
Mechanistic Model (With Factors)
Bolt Shear (Without Factors)
Bolt Shear (With Factors)

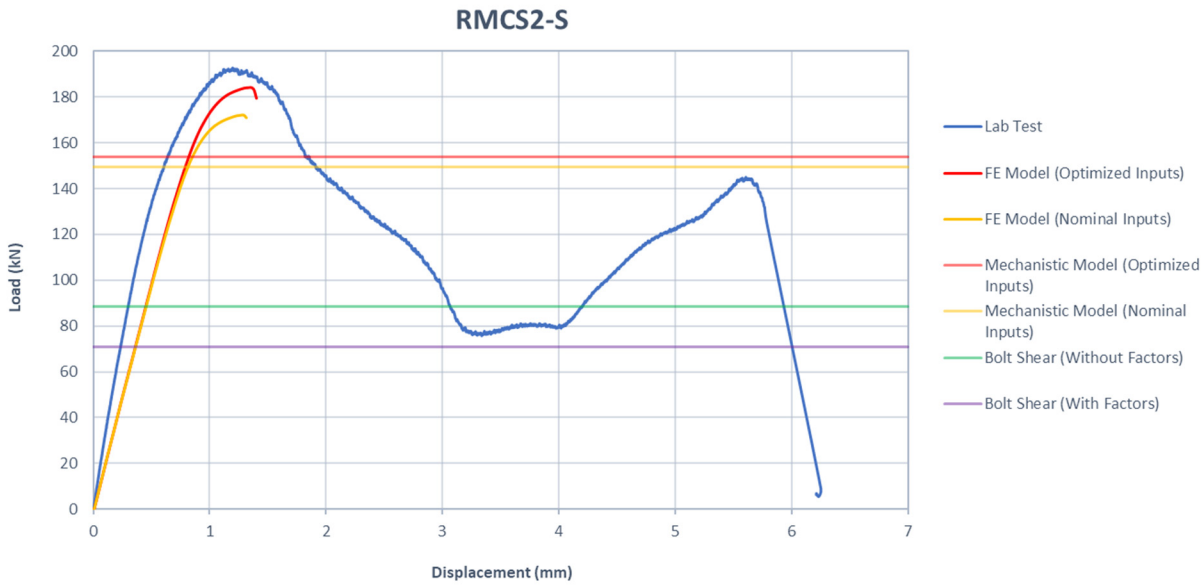
RMCS2-S
Load (kN)
Displacement (mm)
0
20
40
60
80
100
120
140
160
180
200
0
1
2
3
4
5
6
7
Lab Test
FE Model (Optimized Inputs)
FE Model (Nominal Inputs)
Mechanistic Model (Optimized Inputs)
Mechanistic Model (Nominal Inputs)
Bolt Shear (Without Factors)
Bolt Shear (With Factors)

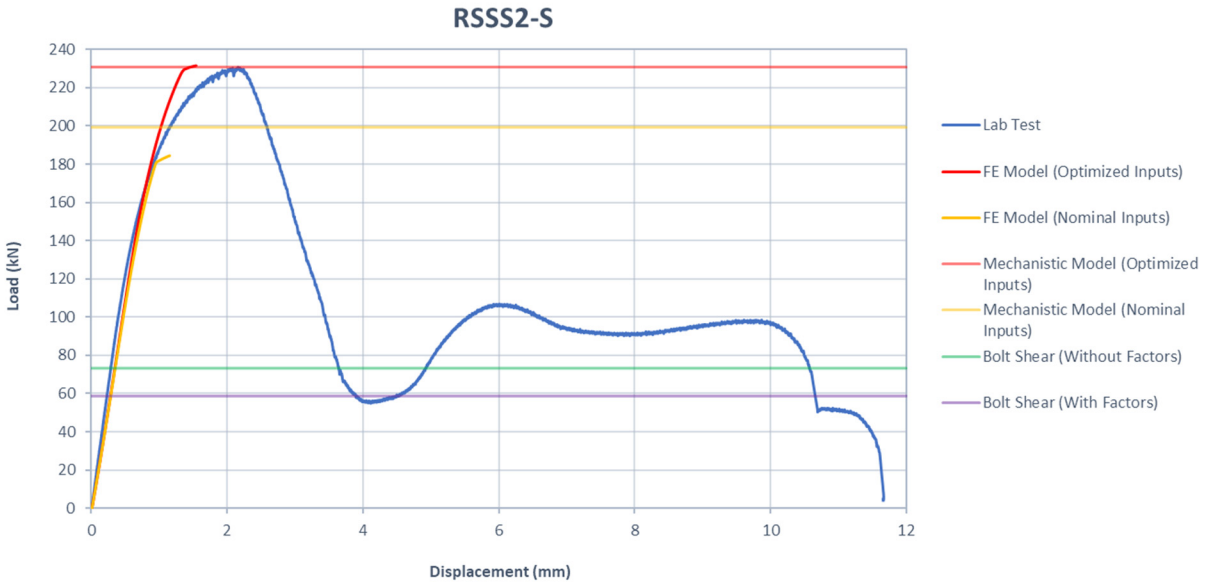
RSSS2-S
Load (kN)
Displacement (mm)
Lab Test
FE Model (Optimized Inputs)
FE Model (Nominal Inputs)
Mechanistic Model (Optimized Inputs)
Mechanistic Model (Nominal Inputs)
Bolt Shear (Without Factors)
Bolt Shear (With Factors)

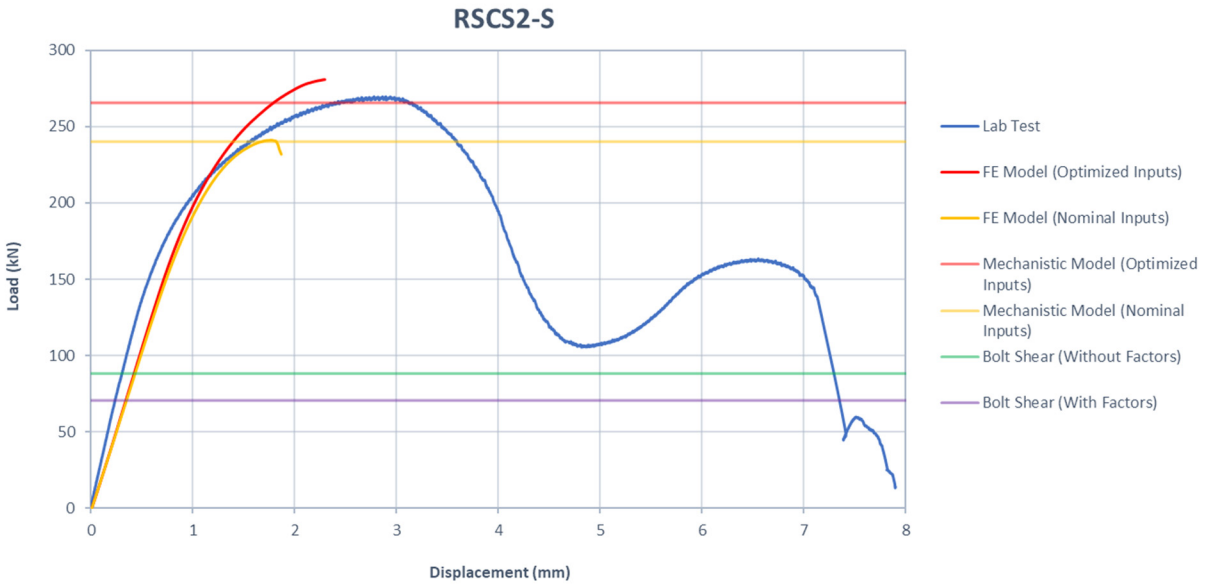
RSCS2-S
Load (kN)
Displacement (mm)
Lab Test
FE Model (Optimized Inputs)
FE Model (Nominal Inputs)
Mechanistic Model (Optimized Inputs)
Mechanistic Model (Nominal Inputs)
Bolt Shear (Without Factors)
Bolt Shear (With Factors)

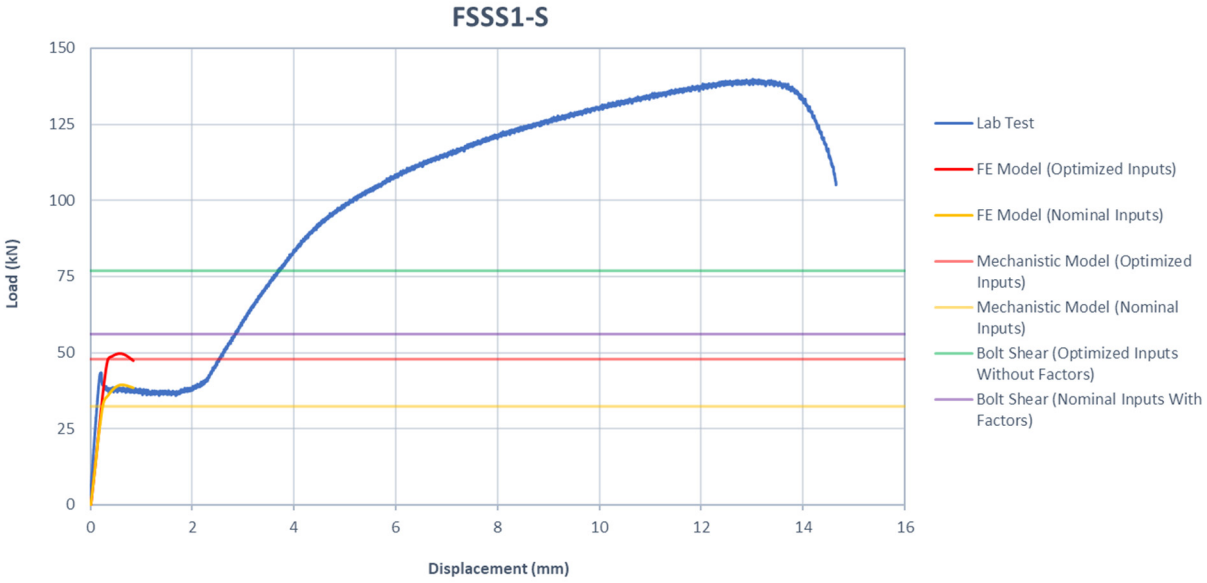
FSSS1-S
Load (kN)
Displacement (mm)
Lab Test
FE Model (Optimized Inputs)
FE Model (Nominal Inputs)
Mechanistic Model (Optimized Inputs)
Mechanistic Model (Nominal Inputs)
Bolt Shear (Optimized Inputs Without Factors)
Bolt Shear (Nominal Inputs With Factors)

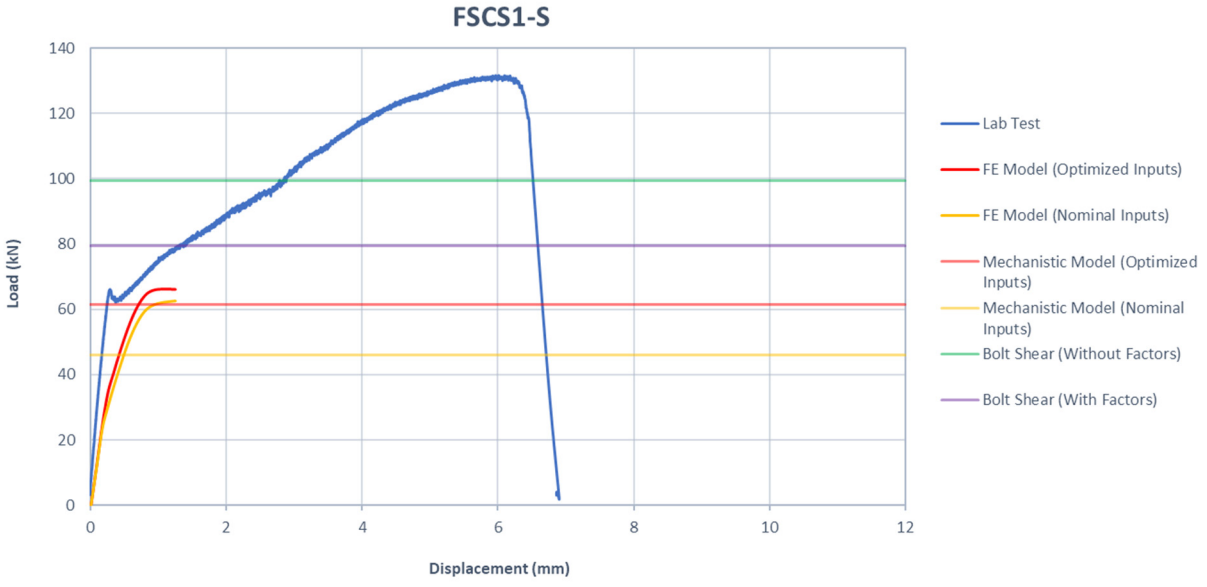
FSCS1-S
Load (kN)
Displacement (mm)
Lab Test
FE Model (Optimized Inputs)
FE Model (Nominal Inputs)
Mechanistic Model (Optimized Inputs)
Mechanistic Model (Nominal Inputs)
Bolt Shear (Without Factors)
Bolt Shear (With Factors)

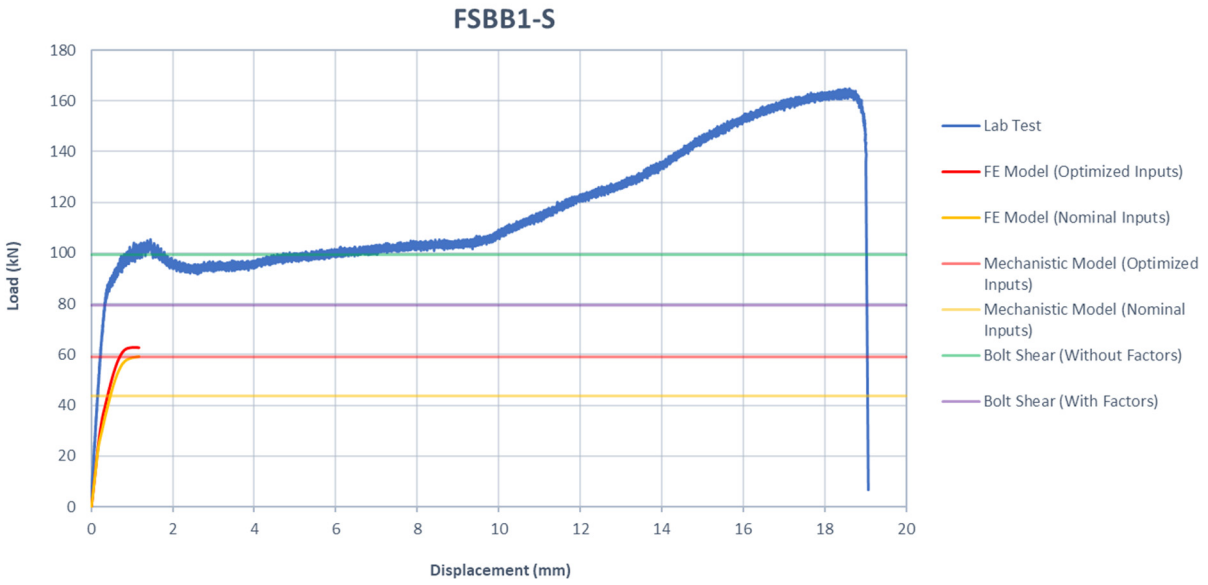
FSBB1-S
Load (kN)
Displacement (mm)
Lab Test
FE Model (Optimized Inputs)
FE Model (Nominal Inputs)
Mechanistic Model (Optimized Inputs)
Mechanistic Model (Nominal Inputs)
Bolt Shear (Without Factors)
Bolt Shear (With Factors)

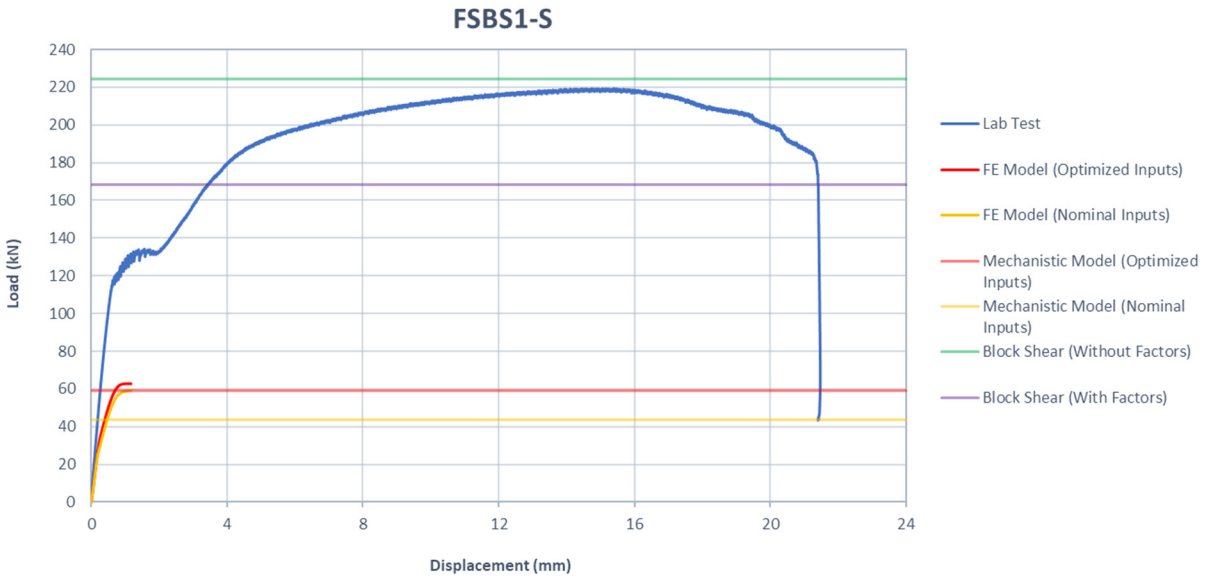
FSBS1-S
Load (kN)
Displacement (mm)
Lab Test
FE Model (Optimized Inputs)
FE Model (Nominal Inputs)
Mechanistic Model (Optimized Inputs)
Mechanistic Model (Nominal Inputs)
Block Shear (Without Factors)
Block Shear (With Factors)

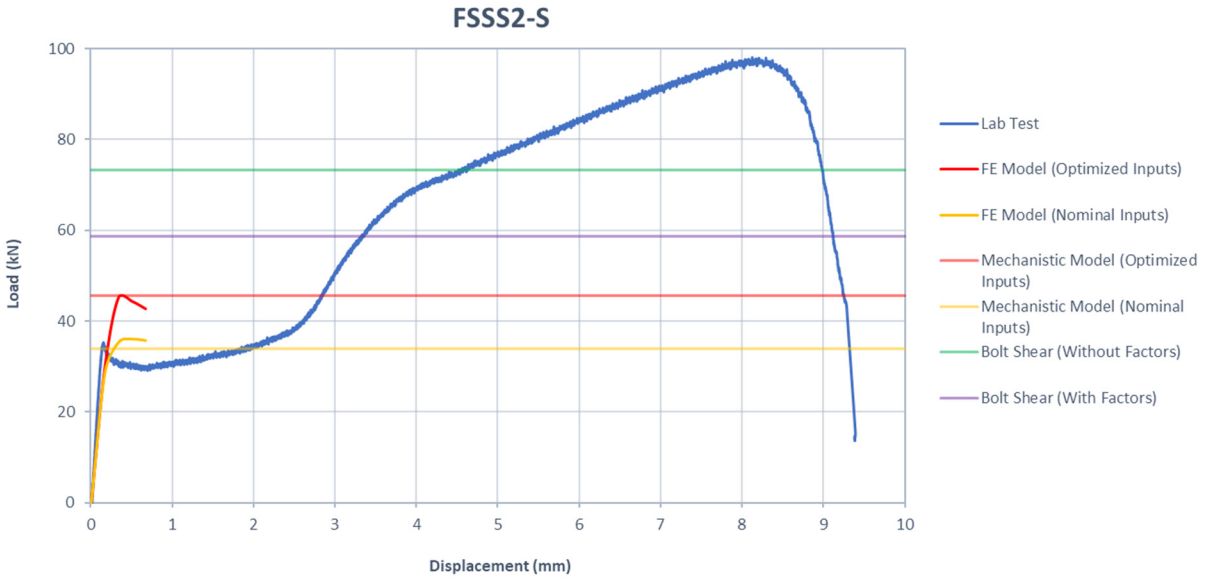
FSSS2-S
Load (kN)
Displacement (mm)
Lab Test
FE Model (Optimized Inputs)
FE Model (Nominal Inputs)
Mechanistic Model (Optimized Inputs)
Mechanistic Model (Nominal Inputs)
Bolt Shear (Without Factors)
Bolt Shear (With Factors)

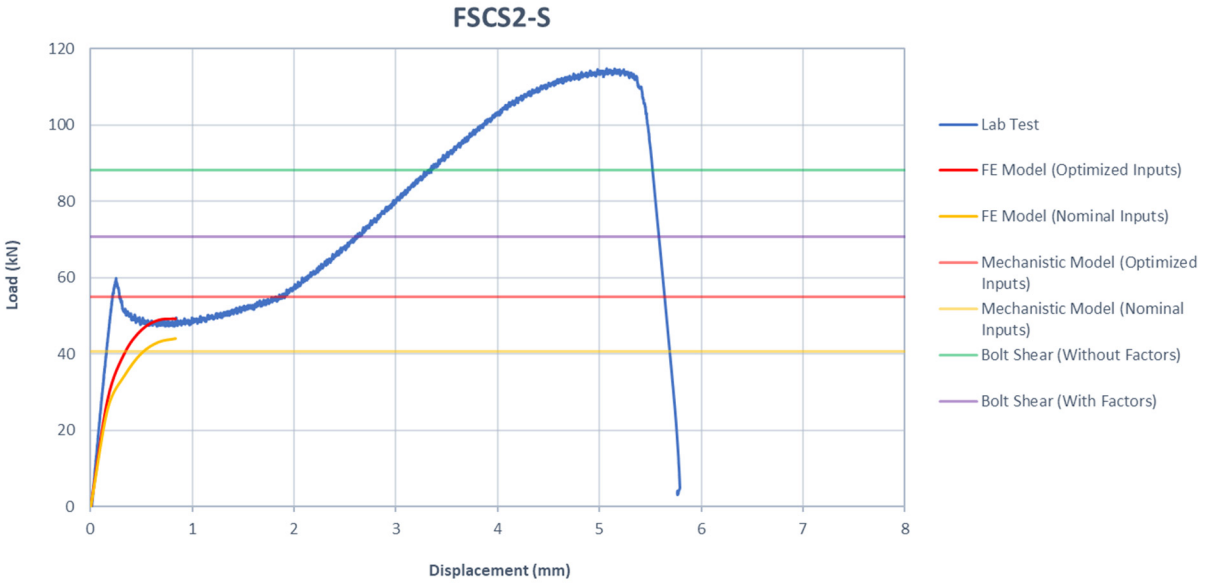
FSCS2-S
Load (kN)
Displacement (mm)
Lab Test
FE Model (Optimized Inputs)
FE Model (Nominal Inputs)
Mechanistic Model (Optimized Inputs)
Mechanistic Model (Nominal Inputs)
Bolt Shear (Without Factors)
Bolt Shear (With Factors)